Università degli Studi di Trento
Dottorato di Richerca in Matematica
XVII ciclo

VLADIMIR A. TITAREV

Derivative Riemann problem and ADER schemes

Ph.D. thesis

SUPERVISOR: PROFESSOR E.F. TORO OBE

TRENTO, ITALIA – 2005

Acknowledgments

I would like to thank the Department of Mathematics, University of Trento, Italy, for giving me a possibility to study and do research as well as travel to numerous conferences. Many thanks are to my supervisor, Professor E.F. Toro OBE, for his guidance, support and encouragement during the course of this research.

Finally, I thank my parents for their continuous support during this exceedingly long project.

Contents

Introduction

Hyperbolic conservation laws arise in areas as diverse as shallow water flows, compressible gasdynamics, turbulence modelling, turbomachinery, plasma modelling, rarefied gas dynamics and many others. Analytical solutions are available only in very few special cases and numerical methods must be used in practical applications. The present thesis is devoted to the construction of numerical schemes of very high-order of accuracy for solving nonlinear hyperbolic conservation law. In designing such schemes one faces at least three major difficulties. One of them concerns the preservation of high accuracy in both space and time for multidimensional problems containing source terms. Another one concerns conservation; this is mandatory in the presence of shock waves. The other very important issue relates to the generation of spurious oscillations in the vicinity of strong gradients; according to Godunov's theorem [18] these are unavoidable by linear schemes of accuracy greater than one. These oscillations pollute the numerical solution and are thus highly undesirable. To avoid generating spurious oscillations, non-linear solution-adaptive schemes must be constructed.

Each one of these difficulties is in itself not easy to resolve; the simultaneous resolution of all three difficulties above represents a formidable task in the numerical analysis of hyperbolic conservation laws.

At present, there are various approaches for constructing numerical schemes that attempt to overcome the above difficulties. The class of Godunov-type methods for solving numerically hyperbolic conservation laws is often regarded as one of the most successful. The original first-order scheme of Godunov [18] uses the self-similar solution of the local Riemann problem with piece-wise constant initial data to compute the upwind numerical flux. The extension to second order of accuracy in time and space can be carried out, amongst other ways, by using a non-oscillatory piece-wise linear reconstruction of data from cell averages. It appears as if it was Kolgan [25] who first proposed to suppress spurious oscillations by applying the so-called principle of minimal values of derivatives, producing in this manner a non-oscillatory (TVD) Godunov-type scheme of second order spatial accuracy. Further, more well-known, developments are due to van Leer [82]. In multiple space dimensions unsplit second-order non-oscillatory methods were constructed by Kolgan [27, 26], Tiliaeva [48], Colella [12] and many others.

TVD methods avoid oscillations by locally reverting to first order of accuracy near discontinuities and extrema. They are therefore unsuitable for applications

involving long time evolution of complex structures, e.g. in acoustic and compressible turbulence. In these applications extrema are clipped as time evolves and numerical diffusion may become dominant. Uniformly very high order methods, both in time and space, are needed for such applications.

Essentially non-oscillatory schemes [19] can be regarded as uniformly high order extensions of Kolgan- van Leer approach in which the data in each cell is represented by polynomials of arbitrary order rather than linear ones. The numerical solutions obtained by these methods are, *at least to the eye*, free from spurious oscillations. The key idea in the r^{th} - order ENO reconstruction procedure used in [19, 43, 7] is to consider r possible stencils covering the given cell (in one space dimension) and to select only one, the smoothest, stencil. The reconstruction polynomial is then built using this selected stencil. The WENO reconstruction [30, 22] takes a convex combination of all r stencils with non-linear solution-adaptive weights. The design of the weights involves local estimates of the smoothness of the solution in each possible stencil so that the reconstruction achieves $(2r-1)^{\text{th}}$ - order of spatial accuracy in smooth regions and emulates the r^{th} - order ENO reconstruction near discontinuities. A more refined version of the one-dimensional WENO reconstruction is the so-called monotonicity-preserving WENO (MPWENO) [3] which is a combination of increasingly high order (e.g. 9^{th} order) WENO and a monotonicity preserving (MP) constraint [46].

Essentially non-oscillatory schemes can be divided into finite-difference schemes and finite-volume schemes. Finite-difference schemes, pioneered in [43] and further developed in [22, 3] seem to be more popular for academic applications due to their simplicity and low cost, e.g. [44], but are restricted to smooth structured meshes. Finite-volume schemes are more expensive and complicated, but can be used on arbitrary non-smooth or/and non-structured meshes and are therefore of more interest to us. In multiple space dimensions these schemes have been developed in [7, 1, 33, 21, 41, 52]. A comparison of finite-difference and finite-volume ENO schemes can be found in [8].

Another very interesting class of very-high order methods for hyperbolic systems is the class of Discontinuous Galerkin (RKDG) Finite Element Methods, which consists of Runge-Kutta DG methods [9, 2, 10, 11] and Space-Time DG methods [79, 80, 81]. These schemes combine the finite-element idea of representing the data locally inside each cells by means of spatial polynomials and using the Riemann problem solution in the computation of the intercell flux. In fact, the first-order DG scheme boils down to the original Godunov method [18]. The key advantage of DG methods over finite-volume schemes lies in their locality: since the data

representation in each cell is stored and evolved by the method no reconstruction procedure is required. This is especially important when using unstructured meshes, e.g. triangles in two space dimensions. Locality of the method also greatly helps in implementing h-refinement algorithms. However, a pending problem in the RKDG methods is the construction of some sort of the limiting procedure to suppress the spurious oscillations. The present approaches, such as the TVD limiter or the use of Hermite WENO schemes [36, 35], do not seem to completely resolve the issue.

We should also mention the class of Compact Difference Methods of Tolstykh and co-workers [55, 56, 57, 59, 60, 58]. These schemes achieve arbitrary order of spatial accuracy, e.g. in last two references up to 57^{th} order is reported. However, the compact approximations are, in general, not monotone and some sort of a limiter must be used to avoid spurious oscillations. The application of the limiter is helped by the fact, that the oscillations are typically contained in 2-3 cells around the discontinuity only.

All the schemes discussed above meet the requirement of very high-order spatial accuracy. Matching time accuracy to space accuracy, however, remains an issue in all of the above approaches due to the use Runge-Kutta methods for time evolution. To avoid spurious oscillations these Runge-Kutta methods must be TVD [42]. This leads to accuracy barriers: the accuracy of such methods cannot be higher than fifth [42]. Moreover, fourth and fifth order methods are quite complicated and have reduced stability range. In most practical implementations reported, when the solution is not smooth, a third order TVD Runge-Kutta method has been used, e.g. [3].

Although increased order of spatial discretisation improves accuracy for some problems such schemes converge with third order only when the mesh is refined and thus should be regarded as third order schemes. For some applications, such as numerical simulation of compressible turbulence and wave propagation problems involving long-time evolution it may be beneficial to use schemes which converge with higher order both in time and space.

A recent approach for constructing schemes of very high order of accuracy is the ADER (Advection-Diffusion-Reaction) approach [71, 72], which stems from the modified Generalised Riemann Problem (MGRP) scheme [64], which in turn is a simplification of the GRP-type schemes [4, 31]. ADER allows the construction of *arbitrarily* high-order accurate schemes, both in time and space. The original ADER idea was applicable to linear advection with constant coefficients only. In [71, 72] formulations were given for one, two and three-dimensional *linear* schemes on regular meshes and implementation of *linear* schemes of up to 10^{th} order in space

and time for both the one-dimensional and the two-dimensional case were reported. In [40, 39, 17] linear schemes for linear systems with constant coefficients of up to 6^{th} order in space and time were constructed. These were then applied to acoustic problems and detailed comparison with other schemes was carried out.

The extension of the ADER approach to non-linear problems relies on the solution of the Derivative Riemann problem. The solution procedure for the DRP reported in [74] provides an approximation to the state variable along the t-axis in the form of a Taylor time expansion and relies, among other things, on the availability of an approximate-state Riemann solver for the non-linear *conventional* (piece-wise constant initial data) Riemann problem system. Construction of ADER schemes for the one-dimensional Euler equations using this Riemann problem solution has been reported in [49]. For the construction of schemes as applied to non-linear scalar equations in one space dimension see also [47]. Extension of ADER to scalar advection-diffusion-reaction equations in one space dimension is reported in [50], where explicit non-linear schemes of up to 6^{th} order are presented.

This thesis is devoted to the further construction and generalization of the ADER advection schemes to the case of non-linear multi-dimensional conservation laws with reactive-like source terms. The main objective is three-fold. Firstly, we would like to extend the schemes to systems for which the solution of the conventional Riemann problem is not available or exceedingly complicated. To achieve this, we need to modify the Derivative Riemann problem solver. Secondly, we would like to extend the schemes to multidimensional *non-linear* hyperbolic systems with reactive-like source terms. Finally, we carry out truncation error and stability analysis of the schemes for the model linear advection equation with constant coefficients in one, two and three space dimensions.

The rest of the thesis is organized as follows.

In Chapter 1 we present the approximate solution of the Derivative Riemann problem. Conventionally, the Riemann problem for a system of conservation laws is defined as the Cauchy problem with initial conditions consisting of two constant states separated by a discontinuity at the origin [18]. A generalization of this is the so-called Generalized Riemann problem [4, 32], whereby a *piece-wise linear data* Riemann problem is posed and solved. A further generalization is to consider the Riemann problem for a system of equations with source terms and *arbitrary piece-wise smooth* initial data [29, 6, 74]. In particular, the initial conditions may consist of polynomials of arbitrary degree. Here we call such Riemann problem, the *Derivative Riemann Problem*, or DRP for short. The approximate solver described here provides an approximation to the state variable along the t-axis in the form

of a Taylor time expansion. To build up this expansion, the original DRP is reduced to a sequence of *conventional* Riemann problems for *homogeneous* advection equations. The leading term of the expansion is computed as the Godunov state of the conventional nonlinear Riemann problem, whereas the evaluation of higher-order terms involves the solution of linearized Riemann problems for spatial derivatives. Therefore, availability of an approximate-state Riemann solver for the non-linear conventional Riemann problem system is crucial for building up the approximate solution to the DRP.

Although exact or approximate-state Riemann solvers are available for a large variety of hyperbolic systems of conservation laws [65, 28], for complex nonlinear systems they may become very complicated or simply unavailable. It is therefore desirable to have a simple procedure for calculating the leading term of the state expansion which would not necessarily require a detailed knowledge of the Riemann problem solution. We develop a new modification of the DRP solver which differs from the original one in the way how the leading term of the Taylor time expansion is computed. That is, the new procedure does not require a Riemann solver for the nonlinear system to be solved. This method proceeds first to a non-linear evolution of the initial condition of a conventional Riemann problem, followed by a simple linearization of the Riemann problem, which leads to closed-form solutions. We illustrate the method by solving the DRP for the inviscid Burgers' equation with a source term. The presented results demonstrate that both the original and modified solvers can maintain a really arbitrary order of accuracy even when the solution to the problem contains a shock wave.

In Chapter 2 we present the general construction of the ADER schemes as applied to the non-homogeneous conservation laws in multiple space dimensions on Cartesian meshes. The ADER schemes have a standard one-step finite-volume form with intercell numerical fluxes obtained by performing time-space integration of the physical fluxes over cell faces. The computation of the ADER intercell flux essentially consists of three major steps. Firstly, since the scheme advances cell averages of the solution but the flux need point-wise values, a high-order polynomial reconstruction is carried out for each cell. In order to circumvent Godunov's theorem [18] and avoid spurious oscillations the weighted essentially non-oscillatory procedure is used. We discuss the finite-volume WENO reconstruction in multiple space dimensions and present extensions of [7, 22, 41] to higher orders and three spatial dimension [52]. Next, at each cell interface (or spatial quadrature point for spatial integration over the side/face in multiple space dimensions) we have the Derivative Riemann problem with the initial data in the form of reconstruction polynomials.

Using the DRP solver described in Chapter 1 we build up an approximate state and use it to obtain the numerical flux. The computation of the numerical source terms is then performed in a rather direct manner and involves application of the multidimensional quadrature.

The chapter is composed as follows: firstly, we describe the reconstruction procedure. Next, the scheme in one spatial dimension is presented. A special version, called ADER-TVD, is developed by replacing the first-order Godunov flux by the second-order TVD flux for each term of the ADER flux expansion leading to a much more accurate scheme. Finally, extension to the multiple space dimensions is carried out, which includes a special adaptation of the DRP solver from Chapter 1.

In Chapter 3 we carry out the stability and truncation error analysis of the schemes as applied to the model linear advection equation with constant coefficients in one, two and three space dimensions. We consider the schemes of different order of accuracy as well as different reconstruction stencils, e.g. upwind or downwind biased. The results of the analysis demonstrate analytically that the schemes do maintain the desired order of accuracy both in time and space and are stable under the normal Courant number. The stability region of the scheme is the same as that of the unsplit first-order Godunov method and the state-of-the-art ENO/WENO schemes.

Numerical results are presented in Chapter 4 and are divided in three groups: scalar equations, nonlinear compressible Euler equations and nonlinear shallow water equations with source terms. In most of the cases we compare our schemes with the state-of-the art finite-volume WENO schemes [41] The convergence studies for a number of well-established test problems demonstrate the schemes compare well with the other modern methods, can maintain the desired very high order of accuracy in both time and space for nonlinear systems, and at the same time can be used for computing solutions with strong moving and possibly colliding discontinuities.

Our presentation is concentrated on the development of main ideas of the ADER flux and source term computation and is thus restricted to Cartesian meshes only. Recently, the approach has been extended to unstructured triangular meshes [23, 24]. All the basic technologies for the computation of the ADER flux, e.g. the solution of the Derivative Riemann Problem, remain the same except the reconstruction, which is now carried out on triangles. In [24] non-oscillatory schemes of up to fourth order of temporal accuracy have been reported and applied to a number of test problems.

Another very recent and promising direction of research on advection schemes are the so-called ADER-DG methods [14, 16, 15]. The basic idea of these methods

is to replace the Runge-Kutta time marching in the DG methods by the ADER-type temporal discretization. The resulting ADER-DG methods are one-step and of really arbitrary order of accuracy. The numerical results of the schemes of up to 6^{th} order as applied to two-dimensional non-linear systems have been reported.

The main results of the present thesis have been published in the following papers:

1. V.A. Titarev and E.F. Toro. Finite-volume WENO schemes for three-dimensional conservation laws. *J. Comput. Phys.*, 201(1):238–260, 2004.

2. E.F. Toro and V.A. Titarev. ADER schemes for scalar non-linear hyperbolic conservation laws with source terms in three-space dimensions. *J. Comput. Phys.*, 202(1):196–215, 2005.

3. V.A. Titarev and E.F. Toro. ADER schemes for three-dimensional nonlinear hyperbolic systems. *J. Comput. Phys.*, 204(2):715–736, 2005.

4. V.A. Titarev and E.F. Toro. MUSTA schemes for multi-dimensional hyperbolic systems: analysis and improvements. *International Journal for Numerical Methods in Fluids*, 49(2):117–147, 2005.

5. E.F Toro and V.A. Titarev. TVD fluxes for the high-order ADER schemes. *J. Sci. Comput.*, 24(3):285-309. 2005.

6. E.F. Toro and V.A. Titarev. Derivative Riemann solvers for systems of conservation laws and ADER methods. *J. Comput. Phys.*, 212(1):150-165. 2006.

and in [51]. One more paper is to appear in J. Comput. Phys.:

E.F. Toro and V.A. Titarev. MUSTA schemes for systems of conservation laws.

Main results have also been presented at a number of international conferences, including the 6th International Conference on Spectral and High-Order Methods, June 21-25, 2004, Brown University, RI, USA and The Tenth International Conference "Hyperbolic Problems: Theory, Numerics and Applications", September 13-17, 2004, Osaka, Japan.

1. *Derivative Riemann Solvers*

Introduction

Conventionally, the Riemann problem for a system of conservation laws is defined as the Cauchy problem with initial conditions consisting of two constant states separated by a discontinuity at the origin. A generalization of the conventional Riemann problem in which the piece-wise linear polynomials are used as the initial data has become to be known as the Generalized Riemann problem [4, 29, 6, 31, 32]. A further generalization is to consider the Riemann problem for a system of equations with source terms and *arbitrary piece-wise smooth* initial data [29, 6, 74]. In particular, the initial conditions may consist of polynomials of arbitrary degree. Here we call such Riemann problem, the *Derivative Riemann Problem*, or DRP for short.

This chapter is devoted to the construction of the approximate solution for the Derivative Riemann problem [74, 78]. Later we intend to use this solution in the design of the numerical schemes. We note that for the Godunov-type methods one does need the Riemann problem solution in the whole $t - x$ space, but rather only along the t axis. Moreover, the complete solution is most probably impossible to construct for a sufficiently complex system. For example, a second-order accurate solution to the GRP problem for a rather simple system of the one-dimensional compressible Euler equations is already quite complicated [32] and probably is not practical.

The solution procedure reported here provides an approximation to the state variable along the t-axis in the form of a Taylor time expansion. To build up this expansion, the original DRP is reduced to a sequence of *conventional* Riemann problems for *homogeneous* advection equations. The leading term of the expansion is computed as the Godunov state of the conventional nonlinear Riemann problem, whereas the evaluation of higher-order terms involves the solution of linearized Riemann problems for spatial derivatives. Therefore, availability of an approximate-state Riemann solver for the non-linear conventional Riemann problem system is crucial for building up the approximate solution to the DRP.

Although approximate-state Riemann solvers exist now for a large variety of hyperbolic systems of conservation laws [65, 28], for complex nonlinear systems they may become very complicated or simply unavailable. It is therefore desirable to have a simple procedure for calculating the leading term of the state expansion

which would not necessarily require a detailed knowledge of the Riemann problem solution. Here we employ a recent EVILIN solver [69] to circumvent the problem of computing the leading term. The method proceeds first to a non-linear evolution of the initial condition of a conventional Riemann problem, followed by a simple linearization of the Riemann problem, which leads to closed-form solutions.

Finally, we illustrate the performance of the DRP solver with both methods for computing the leading term by solving the DRP for the inviscid Burgers' equation with a source term. We first obtain an accurate numerical solution of the problem. Next, we use this solution to verify the accuracy and convergence rate of the approximate DRP solver, developed in this chapter.

1.1. Derivative Riemann problem and solution methodology

The Derivative Riemann Problem or DRP for a hyperbolic system is the initial-value problem

$$\left.\begin{array}{l} \partial_t \mathbf{Q} + \partial_x \mathbf{F}(\mathbf{Q}) = \mathbf{S}(x,t,\mathbf{Q}) \ , \\ \mathbf{Q}(x,0) = \left\{ \begin{array}{ll} \mathbf{Q}_L(x) & \text{if} \quad x < 0 \ , \\ \mathbf{Q}_R(x) & \text{if} \quad x > 0 \ . \end{array} \right. \end{array}\right\} \tag{1.1}$$

where the initial states $\mathbf{Q}_L(x)$, $\mathbf{Q}_R(x)$ are two vectors, the components of which are smooth functions of distance x. We introduce the notation DRP_K to mean the Derivative Riemann Problem in which K represents the number of non-trivial spatial derivatives of the initial condition, $K = \max\{K_L, K_R\}$, where K_L and K_R are such that

$$\partial_x^{(k)} \mathbf{Q}_L(x) \equiv 0 \ \ \forall k > K_L \ , \ \forall x < 0 \ \text{and} \ \partial_x^{(k)} \mathbf{Q}_R(x) \equiv 0 \ \ \forall k > K_R \ , \ \forall x > 0 \ .$$

$\mathbf{DRP}_0$ means that all first ($k = 1$) and higher-order spatial derivatives of the initial condition for the DRP away from the origin vanish identically; this case corresponds to the conventional piece-wise constant data Riemann problem.

The two initial states $\mathbf{Q}_L(x)$ and $\mathbf{Q}_R(x)$ are assumed to be smooth functions, for example $K-$th order polynomials, defined respectively for $x < 0$ and for $x > 0$, with a discontinuity at $x = 0$. Away from $x = 0$ we could use the Cauchy-Kowalewski method to construct a solution $\mathbf{Q}(x,t)$ to (1.1), provided that all the smoothness assumptions of the Cauchy-Kowalewski theorem were met. Here we are interested in the solution of DRP_K, right at $x = 0$, where in fact the initial data may be discontinuous.

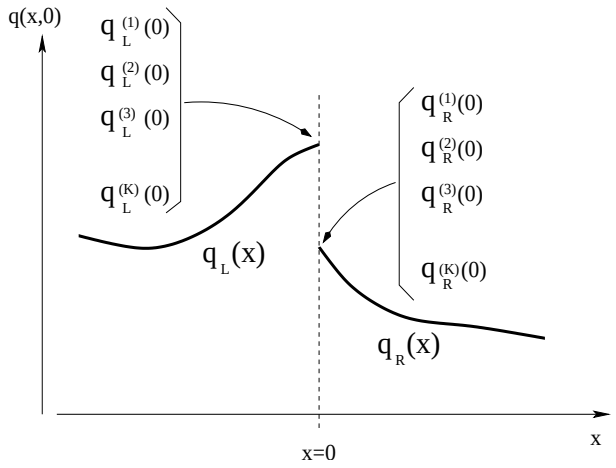

Figure 1.1. Information available in the $\mathbf{DRP}_K$ for a scalar problem.

Figure 1.1 illustrates the initial conditions of the DRP_K and the information available at $t = 0$ at the origin $x = 0$. The initial data is, in general, discontinuous at $x = 0$. Away from $x = 0$ the initial data is smooth, with all spatial derivatives well defined and readily computed. At $x = 0$ we can define one-sided spatial derivatives, so that at the interface $x = 0$ we have jumps in spatial derivatives. These jumps will form the initial data for new (conventional) Riemann problems, as we shall explain below.

We seek a power series solution at $x = 0$ as a function $\mathbf{Q}_{LR}(t)$ of time t only. Formally, we write the sought solution as

$$\mathbf{Q}_{LR}(\tau) = \mathbf{Q}(0, 0_+) + \sum_{k=1}^{K} \left[\partial_t^{(k)} \mathbf{Q}(0, 0_+)\right] \frac{\tau^k}{k!} , \tag{1.2}$$

where $0_+ \equiv \lim_{t \to 0_+} t$. The solution contains a leading term $\mathbf{Q}(0, 0_+)$ and higher-order terms with coefficients determined by $\partial_t^{(k)} \mathbf{Q}(0, 0_+)$. In what follows we describe a method to compute each of the terms of the series expansion.

1.2. The leading term

The leading term $\mathbf{Q}(0, 0_+)$ in the expansion accounts for the *first-instant* interaction of the initial data via the governing PDEs, which is realized solely by the boundary extrapolated values $\mathbf{Q}_L(0)$ and $\mathbf{Q}_R(0)$ in (1.1). Therefore, the leading term $\mathbf{Q}(0, 0_+)$

is found from the *similarity solution* of the following $\mathbf{DRP}_0$

$$\left.\begin{array}{l} \partial_t \mathbf{Q} + \partial_x \mathbf{F}(\mathbf{Q}) = \mathbf{0} \ , \\ \mathbf{Q}(x,0) = \left\{ \begin{array}{lll} \mathbf{Q}_L(0) \equiv \lim_{x\rightarrow 0_-} \mathbf{Q}_L(x) & \text{if} & x<0 \ , \\ \mathbf{Q}_R(0) \equiv \lim_{x\rightarrow 0_+} \mathbf{Q}_R(x) & \text{if} & x>0 \ . \end{array} \right. \end{array} \right\} \tag{1.3}$$

Here, the influence of the source term can be neglected. Denoting the similarity solution by $\mathbf{D}^{(0)}(x/t)$, the sought leading term is given by evaluating this solution along the t-axis, that is along $x/t = 0$, namely

$$\mathbf{Q}(0,0_+) = \mathbf{D}^{(0)}(0) \ . \tag{1.4}$$

The value $\mathbf{D}^{(0)}(0)$ is commonly known as the *Godunov state*, as it corresponds to the numerical flux associated with the first-order upwind scheme of Godunov [18]. In what follows we shall extend the use of this terminology to mean the solution of conventional Riemann problems for spatial derivatives evaluated at $x/t = 0$. In practice, a conventional *Riemann solver*, possibly approximate, is needed here to determine the leading term.

1.3. Higher-order terms

To compute the higher-order terms in (1.2) we need to compute the coefficients, that is the partial derivatives $\partial_t^{(k)}\mathbf{Q}(x,t)$ at $x = 0$, $t = 0_+$. If these were available on both sides of the initial discontinuity at $x = 0$, then one could implement a fairly direct approach to the evaluation of the higher order terms. The method presented below relies on the availability of all spatial derivatives rather than temporal derivatives away from the interface, see Fig. 1.1.

In order to express all *time* derivatives as *functions of space derivatives* we apply the Cauchy-Kowalewski method and use the fact that both the physical flux and source term are the functions of the vector of conservative variables. This yields the following expressions for time derivatives:

$$\partial_t^{(k)}\mathbf{Q}(x,t) = \mathbf{P}^{(k)}(\partial_x^{(0)}\mathbf{Q}, \partial_x^{(1)}\mathbf{Q}, \ldots, \partial_x^{(k)}\mathbf{Q}) \ . \tag{1.5}$$

These time-partial derivatives at $x = 0$ for $t > 0$ have a meaning if the spatial derivatives $\partial_x^{(0)}\mathbf{Q}, \partial_x^{(1)}\mathbf{Q}, \ldots, \partial_x^{(k)}\mathbf{Q}$ can be given a meaning at $x = 0$ for $t > 0$. For $x < 0$ and for $x > 0$ all spatial derivatives

$$\partial_x^{(k)}\mathbf{Q}_L(x) \ , \ \ \partial_x^{(k)}\mathbf{Q}_R(x) \ , \ \ k = 1, 2, \ldots, K$$

are defined and readily computed. At $x = 0$, however, we have the *one-sided* derivatives

$$\left.\begin{array}{l} \partial_x^{(k)}\mathbf{Q}_L(0) = \lim_{x\to 0_-} \partial_x^{(k)}\mathbf{Q}_L(x) \\ \\ \partial_x^{(k)}\mathbf{Q}_R(0) = \lim_{x\to 0_+} \partial_x^{(k)}\mathbf{Q}_R(x) \end{array}\right\} \quad k = 1, 2, \ldots, K \ .$$

We thus have a set of K pairs $(\partial_x^{(k)}\mathbf{Q}_L(0), \partial_x^{(k)}\mathbf{Q}_R(0))$ of constant vectors that could be used as the initial condition for K conventional Riemann problems, if in addition we had a set of corresponding evolution equations for the quantities $\partial_x^{(k)}\mathbf{Q}(x,t)$. The sought evolution equations can be easily constructed. It can be verified that the quantity $\partial_x^{(k)}\mathbf{Q}(x,t)$ obeys the following system of non-linear inhomogeneous evolution equations

$$\partial_t(\partial_x^{(k)}\mathbf{Q}(x,t)) + \mathbf{A}(\mathbf{Q})\partial_x(\partial_x^{(k)}\mathbf{Q}(x,t)) = \mathbf{H}^k \ . \tag{1.6}$$

where the coefficient matrix $\mathbf{A}(\mathbf{Q})$ is precisely the Jacobian matrix of system (1.1). Equations (1.6) are obtained by manipulating derivatives of (1.1). The source term $\mathbf{H}^k$ on the right hand side of (1.6)

$$\mathbf{H}^k = \mathbf{H}^k(\partial_x^{(0)}\mathbf{Q}(x,t), \partial_x^{(1)}\mathbf{Q}(x,t), \ldots, \partial_x^{(k)}\mathbf{Q}(x,t))$$

is a function of the spatial derivatives $\partial_x^{(k)}\mathbf{Q}(x,t)$, for $k = 0, 1, \ldots, k$, and vanishes when the Jacobian matrix $\mathbf{A}$ is constant and $\mathbf{S} \equiv 0$, that is, when the original system in (1.1) is linear and homogeneous with constant coefficients. In order to easily solve these evolution equations we perform two simplifications, namely, we first neglect the source terms $\mathbf{H}^k$ and then we linearize the resulting homogeneous equations.

Neglecting the effect of the source terms $\mathbf{H}^k$ is justified, as we only need $\partial_x^{(k)}\mathbf{Q}(x,t)$ at the *first-instant* interaction of left and right states. We thus have homogeneous non-linear systems for spatial derivatives. Then we perform a linearization of the homogeneous systems about the leading term of the power series expansion (1.2), that is the coefficient matrix is taken as the constant matrix

$$\mathbf{A}_{LR}^{(0)} = \mathbf{A}(\mathbf{Q}(0, 0_+)) \ .$$

Thus, in order to find the spatial derivatives at $x = 0$, $t = 0_+$ we solve the following *homogeneous, linearized* conventional Riemann problems

$$\left.\begin{array}{l} \partial_t(\partial_x^{(k)}\mathbf{Q}(x,t)) + \mathbf{A}_{LR}^{(0)}\partial_x(\partial_x^{(k)}\mathbf{Q}(x,t)) = \mathbf{0} \ , \\ \\ \partial_x^{(k)}\mathbf{Q}(x,0) = \left\{\begin{array}{ll} \partial_x^{(k)}\mathbf{Q}_L(0) \ , & x < 0 \ , \\ \partial_x^{(k)}\mathbf{Q}_R(0) \ , & x > 0 \ . \end{array}\right. \end{array}\right\} \tag{1.7}$$

Note that the (constant) Jacobian matrix $\mathbf{A}_{LR}^{(0)}$ is the same coefficient matrix for all $\partial_x^{(k)}\mathbf{Q}(x,t))$ and is evaluated only once, using the leading term of the expansion.

We denote the similarity solution of (1.7) by $\mathbf{D}^{(k)}(x/t)$. In the computation of all higher order terms, the solutions of the associated Riemann problems are analytic and the question of choosing a *Riemann solver* does not arise. The relevant value at the interface is obtained by evaluating this vector at $x/t = 0$, namely

$$\partial_x^{(k)}\mathbf{Q}(0,0_+)) = \mathbf{D}^{(k)}(0) \ .$$

We call this value the *Godunov state*, in analogy to the interface state (1.4) associated with the leading term.

Having evolved all space derivatives at the interface $x = 0$ we form the time derivatives and finally define the solution of the $\mathbf{DRP}_K$ as the power series expansion

$$\mathbf{Q}_{LR}(\tau) = \mathbf{C_0} + \mathbf{C_1}\tau + \mathbf{C_2}\tau^2 + \ldots + \mathbf{C_K}\tau^K \ . \tag{1.8}$$

where the coefficients are given by

$$\mathbf{C}_k = \frac{\partial_t^{(k)}\mathbf{Q}(0,0_+))}{k!} \ . \tag{1.9}$$

1.4. Riemann solvers for the leading term of DRP

Recall that the leading term of the Taylor series expansion (1.2), the Godunov state, will be the solution of a non-linear problem, found by a non-linear Riemann solver, exact or approximate. As has already been mentioned, for complex nonlinear systems such solvers are very complicated or simply unavailable. It is therefore desirable from the practical point of view to have a simple procedure for calculating the leading term of the state expansion which would not require a detailed knowledge of the Riemann problem solution.

Here, we suggest that the recently-proposed EVILIN Riemann solver [69] be used to obtain the Godunov state of the nonlinear Riemann problem (1.2). The computation of the Godunov state by the EVILIN Riemann solver consists of two main steps. The first step is to open the Riemann fan by using the generalized **M**ulti-**S**tage (GMUSTA) Riemann solver [76] which is an improvement of the MUSTA solver originally proposed in [67]. See also [54]. The GMUSTA Riemann solver solves the local Riemann problem (1.3) numerically rather than analytically by means of a simple first-order scheme applying transmissive boundary conditions at each local time step. This is equivalent to evolving in time the initial data $\mathbf{Q}_L(0)$, $\mathbf{Q}_R(0)$

via the governing equations. In the second step one applies a linearized Riemann solver on the *evolved* initial data obtained from the GMUSTA procedure giving a close-form expression for the Godunov state.

Below we briefly outline the GMUSTA and EVILIN Riemann solvers. Assume that at initial time $t = 0$ we know the left and right initial data values $\mathbf{Q}_L(0)$, $\mathbf{Q}_R(0)$ of the Riemann problem (1.3). We introduce a local spatial domain and the corresponding mesh with $2M$ cells: $-M + 1 \leq m \leq M$ and the local cell size Δx_{loc}. The boundary between cells $m = 0$ and $m = 1$ corresponds to the interface position $x = 0$ in (1.3). Transmissive boundary conditions are applied at numerical boundaries $x_{\pm M+1/2}$ on the grounds that the Riemann - like data extends to $\pm\infty$. We now want to solve this Riemann problem numerically on a given local mesh and construct a sequence of *evolved* data states $\mathbf{Q}_m^{(l)}$, $0 \leq l \leq k$ in such a way, that the final values adjacent to the origin $\mathbf{Q}_0^{(k)}$, $\mathbf{Q}_1^{(k)}$ are close to the sought Godunov state. Here k is the total number of stages (time steps) of the algorithm.

In short, the GMUSTA local time marching for $m = -M+1, \dots M$ is organized as follows:

$$\mathbf{Q}_m^{(l+1)} = \mathbf{Q}_m^{(l)} - \frac{\Delta t_{loc}}{\Delta x_{loc}} \left(\mathbf{F}^{(l)}_{m+1/2} - \mathbf{F}^{(l)}_{m-1/2} \right), \quad \mathbf{F}^{(l)}_{m+1/2} = \mathbf{F}^{GF}(\mathbf{Q}_m^{(l)}, \mathbf{Q}_{m+1}^{(l)}). \quad (1.10)$$

Here $\mathbf{F}^{GF}$ is the monotone first order GFORCE numerical flux [76] which is the upwind generalization of the centred FORCE flux [65] and is given by:

$$\mathbf{F}^{GF} = \Omega_{loc}\mathbf{F}^{LW} + (1 - \Omega_{loc})\mathbf{F}^{LF}, \quad \Omega_{loc} = \frac{1}{1 + C_{loc}}, \quad (1.11)$$

where $\mathbf{F}^{LW}$ and $\mathbf{F}^{LF}$ are the centred Lax-Wendroff and Lax-Friedrichs fluxes, respectively. The local Courant number coefficient $0 < C_{loc} < 1$ is prescribed by the user; we typically take $C_{loc} = 0.9$. The local time step Δt_{loc} is computed according to the conventional formula

$$\Delta t_{loc} = C_{loc}\Delta x_{loc}/S_{max},$$

and then is used in the time update and for evaluation $\mathbf{F}^{LW}$ and $\mathbf{F}^{LF}$. Here S_{max} is the speed of the fastest way in the local solution. The local cell size Δx_{loc} can be chosen arbitrary due to the self-similar structure of the solution of the conventional Riemann problem. For example, one could take $\Delta x_{loc} \equiv 1$ or $\Delta x_{loc} \equiv \Delta x$.

We remark that although expression (1.11) involves centred fluxes, the resulting GFORCE flux is upwind due to the fact that the nonlinear weight Ω_{loc} in (1.11) depends on the local wave speed. We remark that in the special case of the linear constant coefficient equation the GFORCE flux is identical to the Godunov upwind flux.

The time marching procedure is stopped when the desired number of stages k is reached. At the final stage we have a pair of values adjacent to the interface position. For the construction of Godunov-type advection schemes one needs a numerical flux at the origin, which for the outlined procedure is given by

$$\mathbf{F}^{GM}_{i+1/2} = \mathbf{F}^{(k)}_{m+1/2} = \mathbf{F}^{GF}(\mathbf{Q}^{(k)}_{m}, \mathbf{Q}^{(k)}_{m+1}). \tag{1.12}$$

For the purpose of solving the derivative Riemann problem, however, we need the Godunov state as well. In general, the states adjacent to the origin, namely $\mathbf{Q}^{(k)}_0$,$\mathbf{Q}^{(k)}_1$ are different. We now use a linearized Riemann solver to resolve the discontinuity in $\mathbf{Q}$ at the origin resulting in the EVILIN Riemann solver [69]. To this end we solve exactly the following linearized Riemann problem:

$$\begin{aligned} &\partial_t \mathbf{Q} + \mathbf{A}_{1/2}\partial_x \mathbf{Q} = \mathbf{0}, \quad \mathbf{A}_{1/2} = \mathbf{A}(\tfrac{1}{2}(\mathbf{Q}^{(k)}_0 + \mathbf{Q}^{(k)}_1)) \\ &\mathbf{Q}(x,0) = \begin{cases} \mathbf{Q}^{(k))}_0 & \text{if} \quad x < 0\ , \\ \mathbf{Q}^{(k))}_1 & \text{if} \quad x > 0\ . \end{cases} \end{aligned} \tag{1.13}$$

We remark that conventional linearized Riemann solvers have two major deficiencies. Firstly, when a transonic rarefaction is present and the flow thus contains a sonic point they give a large unphysical jump in all flow variables near this sonic point, a *rarefaction shock*, unless explicit *entropy fixes* are enforced. This is due to the fact that linearized Riemann solvers do not open the Riemann fan when the solution contains a sonic point and produce instead a rarefaction shock. Secondly, the linearized Riemann solvers cannot handle the situation when the Riemann problem solution contains very strong rarefaction waves. These problems do not occur for the EVILIN Riemann solver, which is essentially due to the fact that we apply the linearized Riemann solver to *evolved* values rather than to the initial data. See [69] for more details and numerical examples.

It can be shown numerically [76] that when the number of cells $2M$ and number of stages k are large, the GMUSTA flux converges to the Godunov flux with the exact Riemann solver. Correspondingly, the approximate Godunov state produced by the EVILIN solver (1.13) converges to the exact Godunov state, even for nonlinear systems with a complex wave pattern. For the linear constant coefficient equations this property is exact, whereas for nonlinear systems it can be verified by numerical experiments.

We note that since the solution of the piece-wise constant Riemann problem (1.3) is self-similar, the value of the cell size Δx used in the local time marching does not influence the resulting GMUSTA and EVILIN solutions. For a given CFL number C_{loc} these solutions depend only on the number of stages k and domain size $2M$. Moreover, when $M > k$ the transmissive boundary conditions do not affect the numerical solution of (1.3) which in this case depends only on k and C_{loc}.

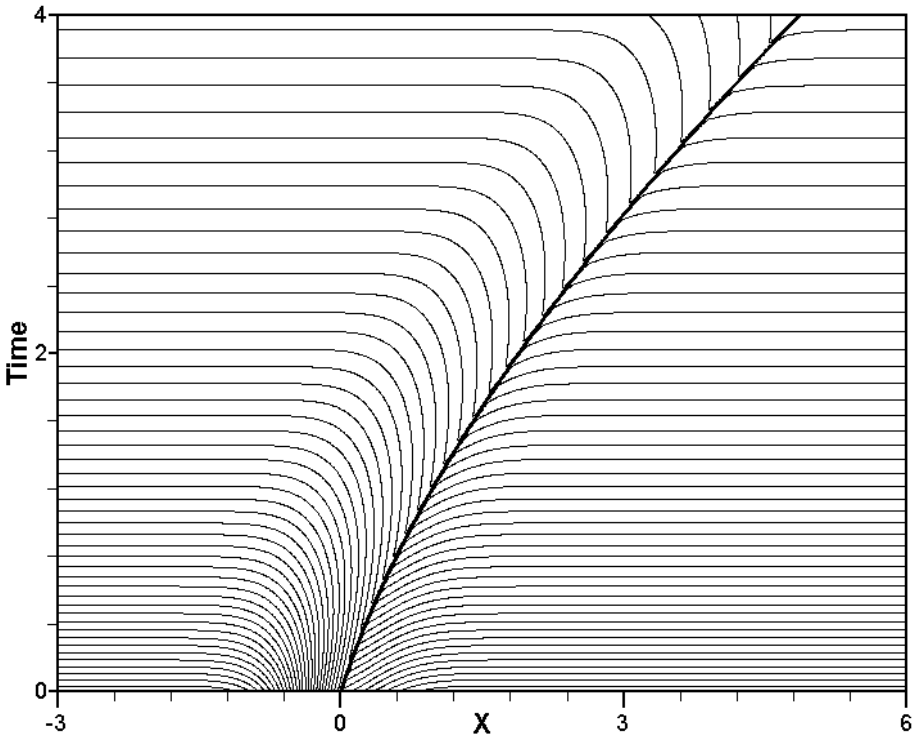

Figure 1.2. Numerical solution of DRP problem (1.14)

1.5. Numerical example

As an example here we solve the following derivative Riemann problem for the inviscid inhomogeneous Burgers' equation:

$$\left.\begin{aligned} &\partial_t q + \partial_x(\tfrac{1}{2}q^2) = e^{-q} \\ &q(x,0) = \begin{cases} q_L(x) = e^{-2(x-\frac{1}{5})^2} & \text{if} \quad x < 0 \\ q_R(x) = \frac{1}{4}e^{-2(x+\frac{1}{5})^2} & \text{if} \quad x > 0 \end{cases} \end{aligned}\right\} \tag{1.14}$$

Fig. 1.2 shows the *global* solution of (1.14) in the $x-t$ plane. This solution was obtained numerically using a high-order non-oscillatory numerical method on a very fine mesh. The dominant feature of the solution is an accelerating shock wave that emerges from the initial discontinuity in the initial condition at $x = 0$. We regard this as the exact solution and define an error by taking the difference between the accurate numerical solution and our semi-analytical DRP solution (1.2).

Table 1 shows the variation of the error as function of the order of accuracy of the Taylor time expansion for different times τ using the exact Riemann solver for the

Table 1 . Convergence study for the Derivative Riemann problem (1.14) for different output times τ and different orders of accuracy. The exact Riemann solver is used.

Order	$t = 0.01$	$t = 0.05$	$t = 0.1$	$t = 0.2$
1	0.2918×10^{-2}	0.1573×10^{-1}	0.3300×10^{-1}	0.6580×10^{-1}
2	0.7381×10^{-4}	0.1513×10^{-2}	0.4560×10^{-2}	0.8916×10^{-2}
3	0.3479×10^{-5}	0.4197×10^{-3}	0.3168×10^{-2}	0.2200×10^{-1}
4	0.2452×10^{-7}	0.1830×10^{-4}	0.3356×10^{-3}	0.6032×10^{-2}
5	0.1389×10^{-8}	0.3843×10^{-5}	0.1042×10^{-3}	0.2331×10^{-2}
6	0.3771×10^{-10}	0.6143×10^{-6}	0.3840×10^{-4}	0.2234×10^{-2}

Table 2 . Convergence study for the Derivative Riemann problem (1.14) for different output times τ and different orders of accuracy. The EVILIN Riemann solver with $M = 1$ and $k = 2$ is used for the leading term.

Order	$t = 0.01$	$t = 0.05$	$t = 0.1$	$t = 0.2$
1	0.3097×10^{-2}	0.9719×10^{-2}	0.2699×10^{-1}	0.5979×10^{-1}
2	0.5873×10^{-2}	0.4161×10^{-2}	0.7710×10^{-3}	0.4269×10^{-2}
3	0.5949×10^{-2}	0.6063×10^{-2}	0.8381×10^{-2}	0.2617×10^{-1}
4	0.5946×10^{-2}	0.5633×10^{-2}	0.4936×10^{-2}	0.1385×10^{-2}
5	0.5947×10^{-2}	0.5647×10^{-2}	0.5165×10^{-2}	0.2269×10^{-2}
6	0.5946×10^{-2}	0.5651×10^{-2}	0.5303×10^{-2}	0.6708×10^{-2}

leading term of the time expansion. As expected, for sufficiently small output times the error rapidly decreases when the number of terms in the expansion increases. For the last output time $\tau = 0.2$ the solution appears to be too far away from the initial time and therefore the Taylor time expansion (1.2) is not accurate anymore.

Tables 2–4 show the convergence study for the case when the EVILIN Riemann solver is used for the leading term of the time expansion. These tables illustrate the influence of the number of cells $2M$ and stages k in the local time marching (1.10) on the accuracy of the resulting Taylor time expansion (1.2). As expected, the size of the error is defined by the accuracy of the leading term. That is the error committed in computing the leading term of the state expansion (1.2) by using the EVILIN approximation (1.13) cannot be recovered by high order terms. From the tables it is clear that this error crucially depends on the number of stages k and cells $2M$ in the

Table 3 . Convergence study for the Derivative Riemann problem (1.14) for different output times τ and different order of accuracy. The EVILIN Riemann solver with $M = 2$ and $k = 10$ is used for the leading term.

Order	$t = 0.01$	$t = 0.05$	$t = 0.1$	$t = 0.2$
1	0.2918×10^{-2}	0.1573×10^{-1}	0.3300×10^{-1}	0.6580×10^{-1}
2	0.7379×10^{-4}	0.1512×10^{-2}	0.4560×10^{-2}	0.8916×10^{-2}
3	0.3501×10^{-5}	0.4197×10^{-3}	0.3168×10^{-2}	0.2200×10^{-1}
4	0.2848×10^{-8}	0.1828×10^{-4}	0.3356×10^{-3}	0.6032×10^{-2}
5	0.2028×10^{-7}	0.3823×10^{-5}	0.1042×10^{-3}	0.2331×10^{-2}
6	0.2171×10^{-7}	0.6349×10^{-6}	0.3842×10^{-4}	0.2234×10^{-2}

Table 4 . Convergence study for the Derivative Riemann problem (1.14) for different output times τ and different order of accuracy. The EVILIN Riemann solver with $M = 3$ and $k = 12$ is used for the leading term.

Order	$t = 0.01$	$t = 0.05$	$t = 0.1$	$t = 0.2$
1	0.2918×10^{-2}	0.1573×10^{-1}	0.3300×10^{-1}	0.6580×10^{-1}
2	0.7381×10^{-4}	0.1512×10^{-2}	0.4560×10^{-2}	0.8916×10^{-2}
3	0.3479×10^{-5}	0.4197×10^{-3}	0.3168×10^{-2}	0.2200×10^{-1}
4	0.2452×10^{-7}	0.1830×10^{-4}	0.3356×10^{-3}	0.6032×10^{-2}
5	0.1389×10^{-8}	0.3843×10^{-5}	0.1042×10^{-3}	0.2331×10^{-2}
6	0.3783×10^{-10}	0.6143×10^{-6}	0.3840×10^{-4}	0.2234×10^{-2}

GMUSTA time marching (1.10). As M and k grow, the leading term obtained by EVILIN approximation approaches the exact one and the EVILIN solution converges to the one obtained by using the exact Riemann solver, see Table 4.

1.6. Summary of the method

The solution of the Derivative Riemann Problem has the following steps:

- **I: The leading term**

  To compute the leading term one solves exactly or approximately the conventional Riemann problem (1.3) to obtain the similarity solution $\mathbf{D}^{(0)}(x/t)$. The leading term in then given by the Godunov state $\mathbf{Q}(0, 0_+)) = \mathbf{D}^{(0)}(0)$.

- **II: Higher order terms**

  1. **Time derivatives in terms of spatial derivatives**

     Use the Cauchy-Kowalewski method to express time derivatives $\partial_t^{(k)}\mathbf{Q}(x,t)$ in terms of functions of space derivatives as in (1.5)

  2. **Evolution equations for derivatives**

     Construct evolution equations for spatial derivatives (1.6).

  3. **Riemann problems for spatial derivatives**

     Simplify (1.6) by neglecting source terms and linearizing the evolution equations. Then pose conventional, homogeneous linearized Riemann problems for spatial derivatives (1.7).

     Solve analytically these Riemann problems to obtain similarity solutions $\mathbf{D}^{(k)}(x/\tau)$ and set $\partial_x^{(k)}\mathbf{Q}(0,0_+)) = \mathbf{D}^{(k)}(0)$.

- **III:** Form the solution as the power series expansion (1.8) with the coefficients (1.9).

Conclusions

In this chapter we first presented a general method for solving the so-called Derivative Riemann problem. The solution procedure builds up an approximate expression for the state variable along the t-axis by reducing the original initial-value problem to a sequence of conventional Riemann problem for homogeneous equations. Only one of these problems is nonlinear whereas others are linearized. Next, we developed a modification of the solution procedure which does not require an approximate-state Riemann solver. The accuracy of the approximate solution has been demonstrated on a model initial value problem for the Burgers' equation. Up to sixth order of accuracy has been demonstrated.

In the next chapter we will use the developed DRP solver in the construction of very high order ADER schemes applicable hyperbolic systems of conservation laws.

2. *General framework of ADER schemes*

Introduction

In this chapter we describe the ADER schemes for multidimensional systems with reactive source terms. The schemes are based on the essentially non-oscillatory reconstruction [19, 7, 22, 41, 52] and the approximate solution of the Derivative Riemann problem, developed in the previous chapter. The chapter is structured as follows. We first present the review of the WENO reconstruction procedure. Next we outline the one-dimensional ADER scheme, which is an extension of [49] to the case of non-homogeneous systems. We also describe a new, improved version of the one-dimensional scheme, called the ADER-TVD scheme, based on the use of TVD fluxes as the building block. Finally, extension of the ADER approach to three space dimensions is given.

2.1. Reconstruction in multiple space dimensions

Here we outline the dimension-by-dimension reconstruction procedure in multiple space dimensions. For the sake of brevity, we concentrate on the three-dimensional case from the beginning. Expressions for the one- and two-dimensional procedure are part of this general case. Our presentation is based on [7, 22, 41, 52]. Note, that in the above references only expressions for the state variables are given whereas here we need the spatial derivatives as well.

2.1.1. Scalar finite-volume reconstruction

The reconstruction problem we face is the following. Given spatial averages of a scalar function $q(x, y, z)$ in a cell I_{ijk}

$$q_{ijk} = \frac{1}{\Delta x}\frac{1}{\Delta y}\frac{1}{\Delta z}\int_{x_{i-1/2}}^{x_{i+1/2}}\int_{y_{j-1/2}}^{y_{j+1/2}}\int_{z_{k-1/2}}^{z_{k+1/2}} q(x, y, z)\, dz\, dy\, dx,$$

we want to compute the point-wise value of q at Gaussian integration points

$$(x_{i+1/2}, y_\alpha, z_\beta)$$

so that the reconstruction procedure is conservative and these reconstructed values are of high-order of accuracy. There are essentially two ways of accomplishing this: genuine multidimensional reconstruction and dimension-by-dimension reconstruction.

The genuine multidimensional reconstruction [21] considers all cells in the multidimensional stencil simultaneously to build up a reconstruction polynomial, whereas dimension-by-dimension reconstruction [7, 41] consists of a number of one-dimensional reconstruction sweeps. The dimension-by-dimension reconstruction is much simpler and less computationally expensive than the genuine multidimensional one; this is especially so in three space dimensions. Therefore, in this paper we use dimension-by-dimension reconstruction throughout.

The general idea of dimension-by-dimension (dim-by-dim) reconstruction in two space dimensions is explained in [7, 41] in the context of the ENO schemes. The extension to three space dimensions is straightforward and consists of three steps. Recall that we need left $q^L_{i+1/2,\alpha\beta}$ and right $q^R_{i+1/2,\alpha\beta}$ extrapolated values. For the left values the stencil consists of cells $I_{i_x i_y i_z}$ such that

$$i - r \le i_x \le i + r, \quad j - r \le i_y \le j + r, \quad k - r \le i_z \le k + r, \tag{2.1}$$

where $r-1$ is the order of polynomials used in WENO sweeps, e.g. $r = 3$ corresponds to the weighted piece-wise parabolic (fifth order) reconstruction and so on. For the right values the stencil consists of cells for which $i + 1 - r \le i_x \le i + 1 + r$ and i_y, i_z vary according to (2.1).

In the first step of the three-dimensional reconstruction for all indexes i_y, i_z from the stencil we perform the one-dimensional WENO reconstruction in the x coordinate direction (normal to the cell face) and obtain two-dimensional averages with respect to $y - z$ coordinate directions:

$$v^L_{i_y i_z} = \frac{1}{\Delta y}\frac{1}{\Delta z}\int_{y_{i_y-1/2}}^{y_{i_y+1/2}}\int_{z_{i_z-1/2}}^{z_{i_z+1/2}} q(x_{i+1/2} - 0, y, z)\, dz\, dy,$$
$$v^R_{i_y i_z} = \frac{1}{\Delta y}\frac{1}{\Delta z}\int_{y_{i_y-1/2}}^{y_{i_y+1/2}}\int_{z_{i_z-1/2}}^{z_{i_z+1/2}} q(x_{i+1/2} + 0, y, z)\, dz\, dy.$$

In the second step we perform one-dimensional reconstruction in y coordinate direction for all values of i_z and obtain one-dimensional averages of the solution with respect to z coordinate direction

$$w^L_{i_z} = \frac{1}{\Delta z}\int_{z_{i_z-1/2}}^{z_{i_z+1/2}} q(x_{i+1/2} - 0, y_\alpha, z)\, dz,$$
$$w^R_{i_z} = \frac{1}{\Delta z}\int_{z_{i_z-1/2}}^{z_{i_z+1/2}} q(x_{i+1/2} + 0, y_\alpha, z)\, dz$$

in lines corresponding to the Gaussian integration points on the y axis ($x = x_{i+1/2}$, $y = y_\alpha$). Finally, for each line ($x = x_{i+1/2}$, $y = y_\alpha$) we obtain reconstructed pointwise values $q(x_{i+1/2}, y_\alpha, z_\beta)$ by again applying the one-dimensional reconstruction

now to $w^L_{i_z}$, $w^R_{i_z}$ in the z coordinate direction. We note that it is also possible to do the z sweep in the second step instead of y sweep.

The two-dimensional reconstruction is obtained by using only two first steps in the above algorithm.

We now proceed to define the reconstructed values for each of the one-dimensional WENO sweeps. We do so in terms of reconstructions of one-dimensional averages u_i of a function $u(\xi)$

$$u_i = \frac{1}{\Delta\xi}\int_{\xi_{i-1/2}}^{\xi_{i+1/2}} u(\xi)\, d\xi,$$

where $\Delta\xi$ is the cell size: $\Delta\xi = \xi_{i+1/2} - \xi_{i-1/2}$. Recall that in one space dimension for any order of accuracy r there are r candidate stencils for reconstruction. For each such stencil of r cells there is a corresponding $(r-1)^{th}$-order polynomial $p_l(\xi)$, $l = 0, \ldots r-1$. The WENO reconstruction procedure [30, 22] defines the reconstructed value as a convex combination of r^{th}-order accurate values of all polynomials, taken with positive non-linear weights. The weights are chosen in such a way as to achieve $(2r-1)^{th}$ order of accuracy when the solution is smooth and to mimic the ENO idea [19, 7] otherwise. For a given point $\tilde{\xi}$ the design of weights consists of three steps. First, one finds the so-called optimal weights d_l so that the combination of all polynomials with these weights produces the value of the polynomial of order $(2r-1)$ corresponding to the large stencil. Next, if optimal weights d_l are all positive one defines the non-linear weights ω_l as

$$\alpha_l = \frac{d_l}{(\epsilon+\beta_l)^2}, \quad \omega_l = \frac{\alpha_k}{\sum_{l=0}^{r-1}\alpha_l}, \quad l = 0, \ldots r-1. \tag{2.2}$$

Here β_l are the so-called smoothness indicators [22]:

$$\beta_l = \sum_{m=1}^{r-1}\int_{\xi_{i-1/2}}^{\xi_{i+1/2}} \left(\frac{d^m}{dx^m}p_l(\xi)\right)^2 \Delta\xi^{2m-1} d\xi, \quad l = 0, \ldots r-1. \tag{2.3}$$

If some of d_l are negative then a special procedure to handle such negative weights must be used, see [41] for details. The small constant ϵ is introduced to avoid division by zero when $\beta_l \equiv 0$; we usually set $\epsilon = 10^{-6}$. The final WENO reconstructed value is then given by

$$u(\tilde{\xi}) = \sum_{l=0}^{r-1} p_l(\tilde{\xi}) w_l. \tag{2.4}$$

In several space dimensions the one-dimensional WENO procedure is applied during each one-dimensional sweep. For the first sweep (normal to the cell face) the weights are designed to obtain reconstructed values at $x_{i+1/2}$; the corresponding

linear weights d_l and smoothness indicators β_l can be found in [22, 3] for up to $r = 6$. For the second and third steps the weights, which will be different from the first step, are designed to achieve $(2r-1)^{\text{th}}$ order of accuracy for Gaussian integration points (y_α, z_β). The values of the weights are tailored to a specific Gaussian integration rule used to discretize the spatial integrals over cell faces and the cell volume, see (2.47), (2.48) below. Our numerical experiments show that the best results in terms of accuracy and computational cost for $r = 3, 4$ are obtained if the following two-point (fourth order) Gaussian quadrature is used:

$$\int_{-1}^{1} \phi(\xi)\, d\xi = \phi\left(-\frac{1}{\sqrt{3}}\right) + \phi\left(+\frac{1}{\sqrt{3}}\right), \tag{2.5}$$

even though the use of (2.5) leads to formal fourth order spatial accuracy. The WENO sweep in the x coordinate direction (normal to the cell face) corresponds to the left and right reconstructed values at $\xi_{i+1/2}$ whereas the y and z sweeps need values at the Gaussian points ξ_α; for the two-point quadrature (2.5) these are $\xi_i \pm \Delta\xi/(2\sqrt{3})$.

It appears as if the weights and reconstruction formulas for the Gaussian integration points ξ_α have not been reported in the literature so far. Therefore, in order to provide the complete information about the scheme below we give all necessary information for one dimensional sweeps in the piece-wise parabolic ($r = 3$) and piece-wise cubic ($r = 4$) reconstruction.

2.1.2. Piece-wise parabolic WENO reconstruction ($r = 3$)

We consider a cell $[\xi_{i-1/2}, \xi_{i+1/2}]$ and provide expressions for $u(\xi_{i+1/2}-0)$, $u(\xi_{i-1/2}+0)$ and $u(\xi_i \pm \Delta\xi/(2\sqrt{3}))$. The three candidate stencils for reconstruction are

$$S_0 = (i, i+1, i+2), \quad S_1 = (i-1, i, i+1), \quad S_2 = (i-2, i-1, i).$$

The corresponding smoothness indicators are given by [22]

$$\begin{aligned}
\beta_0 &= \frac{13}{12}(u_i - 2u_{i+1} + u_{i+2})^2 + \frac{1}{4}(3u_i - 4u_{i+1} + u_{i+2})^2, \\
\beta_1 &= \frac{13}{12}(u_{i-1} - 2u_i + u_{i+1})^2 + \frac{1}{4}(u_{i-1} - u_{i+1})^2, \\
\beta_2 &= \frac{13}{12}(u_{i-2} - 2u_{i-1} + u_i)^2 + \frac{1}{4}(u_{i-2} - 4u_{i-1} + 3u_i)^2.
\end{aligned} \tag{2.6}$$

The optimal weights d_l and the left extrapolated value are given by [22]:

$$d_0 = \frac{3}{10}, \quad d_1 = \frac{3}{5}, \quad d_2 = \frac{1}{10} \tag{2.7}$$

$$u(\xi_{i+1/2}-0)=\frac{1}{6}\omega_0(-u_{i+2}+5u_{i+1}+2u_i)+$$
$$\frac{1}{6}\omega_1(-u_{i-1}+5u_i+2u_{i+1})+\frac{1}{6}\omega_2(2u_{i-2}-7u_{i-1}+11u_i). \tag{2.8}$$

For derivatives we have

$$\Delta x\frac{d}{dx}u(\xi_{i+1/2}-0)=\omega_0(u_{i+1}-u_i)+$$
$$\omega_1(u_{i+1}-u_i)+\omega_2(u_{i-2}-3u_{i-1}+2u_i).$$
$$\Delta x^2\frac{d^2}{dx^2}u(\xi_{i+1/2}-0)=\omega_0(u_{i+2}-2u_{i+1}+u_i)+$$
$$\omega_1(u_{i+1}-2u_i+u_{i-1})+\omega_2(u_i-2u_{i-1}+u_{i-2}).$$

The optimal weights and extrapolated values for the right boundary are obtained by symmetry and are thus omitted.

For the first Gaussian integration point $\xi=\xi_i-\Delta\xi/(2\sqrt{3})$ the optimal weights are as follows [52]:

$$d_0=\frac{210-\sqrt{3}}{1080},\quad d_1=\frac{11}{18},\quad d_2=\frac{210+\sqrt{3}}{1080} \tag{2.9}$$

and the reconstructed values are given by

$$u\left(\xi_i-\frac{\Delta\xi}{2\sqrt{3}}\right)=\omega_0\left[u_i+(3u_i-4u_{i+1}+u_{i+2})\frac{\sqrt{3}}{12}\right]+$$
$$\omega_1\left[u_i-(-u_{i-1}+u_{i+1})\frac{\sqrt{3}}{12}\right]+\omega_2\left[u_i-(3u_i-4u_{i-1}+u_{i-2})\frac{\sqrt{3}}{12}\right]. \tag{2.10}$$

$$\Delta x\frac{d}{dx}u\left(\xi_i-\frac{\Delta\xi}{2\sqrt{3}}\right)=\frac{1}{6}\omega_0\left[-9u_i+12u_{i+1}-3u_{i+2}-\sqrt{3}u_i+2\sqrt{3}u_{i+1}-\sqrt{3}u_{i+2}\right]+$$
$$\frac{1}{6}\omega_1\left[-3u_{i-1}+3u_{i+1}+2\sqrt{3}u_i-\sqrt{3}u_{i-1}-\sqrt{3}u_{i+1}\right]+$$
$$\frac{1}{6}\omega_2\left[9u_i-12u_{i-1}+3u_{i-2}-\sqrt{3}u_i+2\sqrt{3}u_{i-1}-\sqrt{3}u_{i-2}\right]. \tag{2.11}$$

$$\Delta x^2\frac{d^2}{dx^2}u\left(\xi_i-\frac{\Delta\xi}{2\sqrt{3}}\right)=\omega_0\left[u_i-2u_{i+1}+u_{i+2}\right]+$$
$$\omega_1\left[-2u_i+u_{i+1}+u_{i-1}\right]+\omega_2\left[u_i-2u_{i-1}+u_{i-2}\right]. \tag{2.12}$$

For the second Gaussian integration point $\xi = \xi_i + \Delta\xi/(2\sqrt{3})$ the optimal weights and the extrapolated values are obtained from symmetry

We note that the nonlinear weights ω_l must be computed according to (2.2) *separately* for each of the points $\xi_i \pm \Delta\xi/(2\sqrt{3})$.

2.1.3. Piece-wise cubic WENO reconstruction ($r = 4$)

The four candidate stencils are

$$\begin{aligned} S_0 &= (i, i+1, i+2, i+3), \quad S_1 = (i-1, i, i+1, i+2), \\ S_2 &= (i-2, i-1, i, i+1), \quad S_3 = (i-3, i-2, i-1, i). \end{aligned} \tag{2.13}$$

The corresponding smoothness indicators as well as expressions for $u^L_{i+1/2}$ and $u^R_{i-1/2}$ are rather cumbersome and can be found in [3]. We omit them to save space and describe the weights and reconstructed values only for the Gaussian integration points. The reconstructed values for derivatives are omitted as well.

For the first Gaussian integration point $\xi = \xi_i - \Delta\xi/(2\sqrt{3})$ the optimal weights are as follows [52][1]:

$$\begin{aligned} d_0 &= \frac{-50 + 3717\sqrt{3}}{166320}\sqrt{3}, & d_1 &= \frac{72\sqrt{3}}{7}\left(\frac{889\sqrt{3}}{63360} - \frac{587}{1995840}\right), \\ d_2 &= \frac{72\sqrt{3}}{7}\left(\frac{889\sqrt{3}}{63360} + \frac{587}{1995840}\right), & d_3 &= \frac{50 + 3717\sqrt{3}}{166320}\sqrt{3} \end{aligned}$$

and the reconstructed value is given by

$$\begin{aligned} & u\left(\xi_i - \frac{\Delta\xi}{2\sqrt{3}}\right) = \\ & \omega_0\left[u_i - (-43u_i + 69u_{i+1} - 33u_{i+2} + 7u_{i+3})\frac{\sqrt{3}}{144} - (-u_i + 3u_{i+1} - 3u_{i+2} + u_{i+3})\frac{\sqrt{3}}{432}\right] + \\ & \omega_1\left[u_i - (-15u_i + 27u_{i+1} - 7u_{i-1} - 5u_{i+2})\frac{\sqrt{3}}{144} + (-3u_i + 3u_{i+1} + u_{i-1} - u_{i+2})\frac{\sqrt{3}}{432}\right] + \\ & \omega_2\left[u_i - (15u_i + 7u_{i+1} - 27u_{i-1} + 5u_{i-2})\frac{\sqrt{3}}{144} + (3u_i - u_{i+1} - 3u_{i-1} + u_{i-2})\frac{\sqrt{3}}{432}\right] \\ & \omega_3\left[u_i - (43u_i - 69u_{i-1} + 33u_{i-2} - 7u_{i-3})\frac{\sqrt{3}}{144} - (u_i - 3u_{i-1} + 3u_{i-2} - u_{i-3})\frac{\sqrt{3}}{432}\right]. \end{aligned} \tag{2.14}$$

For the second Gaussian integration point optimal weights and reconstructed values are obtained from symmetry.

[1]Note that in note, that there is a misprint in the paper [52]

2.1.4. Reconstruction for systems

The reconstruction for systems can be carried out either in conservative variables or in local characteristic variables, see e.g. [19]. For the first option the above expressions (2.7) – (2.14) are used for each component of the vector of conservative variables $\mathbf{Q}$. For the characteristic reconstruction one first transforms to characteristic variables and then applies (2.7) – (2.14) to each component of these variables. The final values are obtained by transforming back to conservative variables.

Although the use of characteristic decomposition in reconstruction increases the computational cost of the scheme, our experiments show that in some cases it is necessary in order to avoid spurious oscillations. Therefore, in this paper we always carry out reconstruction in local characteristic variables.

A note needs to be added on the use of the ENO and WENO reconstructions for nonlinear systems. In general, ENO reconstruction avoids generating large $O(1)$ oscillations near discontinuities by selecting a smooth stencil of $r-1$ cells out of r possible stencils covering the given cell. WENO reconstruction mimics the behavior of the ENO reconstruction near discontinuities by assigning nearly zero weights to stencils which cross a discontinuity. However, if the solution contains two discontinuities which are too close to each other the reconstruction procedure will not be able to find a smooth stencil and spurious oscillations will appear. As a result, the scheme may crash.

To avoid the above problem we adopt (with appropriate modifications for the present study) a method proposed in [19]. Consider computation of the left boundary extrapolated values for the cell I_{ijk} used in the evaluation of the numerical flux $\mathbf{F}_{i+1/2,jk}$. For each Gaussian integration point $(x_{i+1/2}-0, y_\alpha, z_\beta)$ we check the following conditions:

$$|\rho(x_{i+1/2}-0, y_\alpha, z_\beta)-\rho_{ijk}| \le 0.9\,\rho_{ijk}, \quad |p(x_{i+1/2}-0, y_\alpha, z_\beta)-p_{ijk}| \le 0.9\,p_{ijk} \quad (2.15)$$

If conditions (2.15) are not satisfied we decrease the order of reconstruction r in each of the one-dimensional WENO sweeps and repeat the reconstruction step for the left boundary extrapolated values. If conditions (2.15) are not satisfied even for the weighted piece-wise linear ($r=2$) reconstruction we switch to a MUSCL-type reconstruction in each of the one dimensional sweeps:

$$u^L_{i+1/2} = u_i + \frac{\Delta\xi}{2}S, \quad u^R_{i-1/2} = u_i - \frac{\Delta\xi}{2}S, \quad u\left(\xi_i \pm \frac{\Delta\xi}{2\sqrt{3}}\right) = u_i \pm \frac{\Delta\xi}{2\sqrt{3}}S,$$

where S is the limited slope. We use minmod-type limiter [25]:

$$S = \frac{1}{2}(\mathrm{sign}(\Delta_-)+\mathrm{sign}(\Delta_+))\min(|\Delta_-|,|\Delta_+|), \quad \Delta_- = \frac{u_i-u_{i-1}}{\Delta\xi}, \quad \Delta_+ = \frac{u_{i+1}-u_i}{\Delta\xi}.$$

The right boundary extrapolated values are treated in an entirely analogous manner.

Our numerical experiments show that the use of a less diffusive slope limiter in the above framework does not improve the accuracy and may sacrifice the robustness of the scheme.

We remark that the use of the above procedure does not in any way degrade the high order of accuracy of the schemes for smooth solutions; see [19] for details.

2.2. ADER schemes in one space dimension

Consider a hyperbolic system in conservation form given by

$$\partial_t \mathbf{Q} + \partial_x \mathbf{F}(\mathbf{Q}) = \mathbf{S}(x, t, \mathbf{Q}) \tag{2.16}$$

along with initial and boundary conditions. Here $\mathbf{Q}$ is the vector of unknown conservative variables, $\mathbf{F}(\mathbf{Q})$ is the physical flux vector and $\mathbf{S}(x, t, \mathbf{Q})$ is a source term. Integrating (2.16) over a space-time control volume in $x-t$ space $[x_{i-1/2}, x_{i+1/2}] \times [t^n, t^{n+1}]$ of dimensions $\Delta x = x_{i+1/2} - x_{i-1/2}$, $\Delta t = t^{n+1} - t^n$, we obtain the following one-step relations:

$$\mathbf{Q}_i^{n+1} = \mathbf{Q}_i^n + \frac{\Delta t}{\Delta x} \left(\mathbf{F}_{i-1/2} - \mathbf{F}_{i+1/2} \right) + \Delta t \, \mathbf{S}_i. \tag{2.17}$$

Here $\mathbf{Q}_i^n$ is the cell average of the solution at time level t^n, $\mathbf{F}_{i+1/2}$ is the time average of the physical flux at cell interface $x_{i+1/2}$ and $\mathbf{S}_i$ is the time-space average of the source term over the control volume:

$$\begin{gathered} \mathbf{Q}_i^n = \frac{1}{\Delta x} \int_{x_{i-1/2}}^{x_{i+1/2}} \mathbf{Q}(x, t^n) \, dx, \quad \mathbf{F}_{i+1/2} = \int_{t^n}^{t^{n+1}} \mathbf{F}(\mathbf{Q}(x_{i+1/2}, t) \, dt, \\ \mathbf{S}_i = \frac{1}{\Delta t} \frac{1}{\Delta x} \int_{t^n}^{t^{n+1}} \int_{x_{i-1/2}}^{x_{i+1/2}} \mathbf{S}(x, \tau, \mathbf{Q}(x, \tau)) \, dx \, d\tau. \end{gathered} \tag{2.18}$$

Equation (2.17) involving the integral averages (2.18) is up to this point an exact relation, but can be used to construct numerical methods to compute approximate solutions to (2.16). This is done by subdividing the domain of interest into many disjoint control volumes and by defining approximations to the flux integrals, called numerical fluxes, and to the source integral, called numerical source. Let us denote the approximations to these integrals by the same symbols $\mathbf{F}_{i+\frac{1}{2}}$ and $\mathbf{S}_i$ in (2.18). Then the formula (2.17) is a conservative one-step scheme to solve (2.16).

The ADER approach defines numerical fluxes and numerical sources in such a way that the explicit conservative one-step formula (2.17) computes numerical solutions to (2.16) to arbitrarily high order of accuracy in both space and time. The approach consists of three steps: (i) reconstruction of point wise values from cell averages, (ii) solution of a Derivative Riemann problem at the cell interface and evaluation of the intercell flux $\mathbf{F}_{i+1/2}$, (iii) evaluation of the numerical source term $\mathbf{S}_i$ by integrating a time-space Taylor expansion of the solution inside the cell.

The point-wise values of the solution at $t = t^n$ are reconstructed from cell averages by means of essentially non-oscillatory (ENO) [19] or weighted essentially non-oscillatory (WENO) [30, 22] techniques. We remark that for the r^{th} order accurate scheme (in time and space) the reconstruction polynomials must be of $(r-1)^{\text{th}}$ order, e.g. for third order schemes we use piece-wise parabolic reconstruction and so on. After the reconstruction step the conservative variables in each cell are represented by vectors $\mathbf{p}_i(x)$ of polynomials. Then at each cell interface we can pose the following Derivative Riemann problem:

$$\begin{aligned} \text{PDE:} \quad & \partial_t \mathbf{Q} + \partial_x \mathbf{F}(\mathbf{Q}) = \mathbf{S}(x,t,\mathbf{Q}), \\ \text{IC:} \quad & \mathbf{Q}(x,0) = \begin{cases} \mathbf{Q}_L(x) = \mathbf{p}_i(x), & x < x_{i+1/2}, \\ \mathbf{Q}_R(x) = \mathbf{p}_{i+1}(x), & x > x_{i+1/2}. \end{cases} \end{aligned} \tag{2.19}$$

Obviously, the initial-boundary problem (2.19) is exactly the DRP (1.1). Therefore, in order to obtain an approximate solution for the interface state $\mathbf{Q}(x_{i+1/2},\tau)$, where τ is local time $\tau = t - t^n$, we apply the solution procedure outlined in the previous chapter and obtain the approximate state $\mathbf{Q}(x_{i+1/2},\tau))$ in the form of the temporal polynomial (1.2).

Two options now exist to evaluate the numerical flux depending on the way we evaluate the Godunov state of (1.3). If a conventional approximate-state Riemann solver for the Riemann problem (1.3) is available we use the *state-expansion* version of the method. We insert the approximate state $\mathbf{Q}(x_{i+1/2},\tau))$ into the definition of the numerical flux (2.18) and then use an appropriate r^{th}-order accurate quadrature for time integration:

$$\mathbf{F}_{i+1/2} = \sum_{l=0}^{K_l} \mathbf{F}(\mathbf{Q}(x_{i+1/2}, \alpha_l \Delta t))\omega_l. \tag{2.20}$$

Here α_l and ω_l are properly scaled nodes and weights of the rule and K_l is the number of nodes.

When a conventional approximate-state Riemann solver is not available, we use the EVILIN Riemann solver to obtain the leading term of the state expansion (1.2).

Numerical experiments show that in this case the best results are obtained when the so-called *flux-expansion* ADER [53] is used. The main difference from the state-expansion ADER is that we now seek a truncated Taylor time expansion of the physical flux at $x_{i+1/2}$:

$$\mathbf{F}(x_{i+1/2},\tau) = \mathbf{F}(x_{i+1/2},0+) + \sum_{k=1}^{r-1} \left[\frac{\partial^k}{\partial t^k} \mathbf{F}(x_{i+1/2},0+) \right] \frac{\tau^k}{k!}. \tag{2.21}$$

From (2.18) and (2.21) the numerical flux is now given by

$$\mathbf{F}_{i+1/2} = \mathbf{F}(x_{i+1/2},0+) + \sum_{k=1}^{r-1} \left[\frac{\partial^k}{\partial t^k} \mathbf{F}(x_{i+1/2},0+) \right] \frac{\Delta t^k}{(k+1)!} \, . \tag{2.22}$$

The leading term $\mathbf{F}(x_{i+1/2},0+)$ accounts for the first interaction of left and right boundary extrapolated values and is the GMUSTA flux (1.12). Other options include the use of conventional upwind fluxes, see [53] for details. The remaining higher order time derivatives of the flux in (2.22) are expressed via time derivatives of the intercell state $\mathbf{Q}(x_{i+1/2},0+)$, which are known from (1.1). The leading term $\mathbf{Q}(0+,0)$ is now given by the EVILIN Riemann solver (1.13). No numerical quadrature is then required to compute the numerical flux.

An important issue is the choice of parameters M and k in the local GMUSTA time marching (1.10). In general, we observe that convergence of the EVILIN state to the exact Godunov state is obtained only when $M, k \to \infty$. However, practical experience suggest that for designing *numerical methods* in most of the cases the choice $M = 1$ and $k = 1$ in the GMUSTA time marching (1.10) gives numerical results that are comparable with those from the most accurate of fluxes, namely, the first-order Godunov upwind flux used in conjunction with the exact Riemann solver[2]. See [76] for a more detailed discussion of the choice of M and k. Therefore, for the rest of the paper we use these values in ADER schemes.

Now we deal with the treatment of the source term. The first step in the evaluation of the numerical source term $\mathbf{S}_i^n$ in (2.18) is to discretize the space integral by means of a N-point Gaussian rule:

$$\mathbf{S}_i = \sum_{\alpha=1}^{N} \left(\frac{1}{\Delta t} \int_{t^n}^{t^{n+1}} \mathbf{S}(x_\alpha, \tau, \mathbf{Q}(x_\alpha,\tau)) d\tau \right) K_\alpha, \tag{2.23}$$

where K_α are the scaled weights of the rule, x_α are the Gaussian integration points and N is the total number of points in the rule.

[2]Note that in [78] the value of k is incorrectly given as 2.

Next for each Gaussian point x_α (which are different from $x_{i\pm1/2}$) we reconstruct values of $\mathbf{Q}$ and its spatial derivatives by means of the WENO reconstruction, write the Taylor time expansion and perform the Cauchy-Kowalewski procedure to replace all time derivatives by spatial derivatives. As a result we obtain high-order approximations to $\mathbf{Q}(x_\alpha, \tau)$, $\alpha = 1, \ldots, N$ in the form of temporal polynomials. Finally, the time integration in (2.18) is carried out by means of a Gaussian quadrature:

$$\mathbf{S}_i = \sum_{\alpha=1}^{N} \left(\sum_{l=1}^{N} \mathbf{S}(x_\alpha, \tau_l, \mathbf{Q}(x_\alpha, \tau_l)) K_l \right) K_\alpha. \tag{2.24}$$

The solution is advanced in time by updating the cell averages according to the one-step formula (2.17).

2.3. ADER-TVD schemes

We recall that in the solution of the DRP we have made use of the so-called *Godunov state* in the solution of each of the conventional Riemann problems to evaluate each term of the expansion. It is known that the use of the Godunov state is associated with the flux of a first-order monotone scheme, namely the Godunov first-order upwind method [18]. In this section we propose to use a second-order TVD flux (or state) instead of the first-order Godunov flux or state, to evaluate each term of the expansion. We present the main ideas in terms of the model hyperbolic equation. Our description follows that of [75, 77].

2.3.1. The scheme for the linear advection equation

Consider

$$\partial_t q + \partial_x f(q) = 0 \,, \quad f(q) = \lambda q \,, \quad \lambda : \text{constant} \,. \tag{2.25}$$

The corresponding finite volume scheme reads

$$q_i^{n+1} = q_i^n - \frac{\Delta t}{\Delta x} \left(f_{i+1/2} - f_{i-1/2} \right) \,. \tag{2.26}$$

We use the *state-expansion* version of ADER, whose numerical flux in (2.26) is computed by first solving the appropriate DRP, the solution of which is

$$q(x_{i+1/2}, \tau) = q(x_{i+1/2}, 0+) + \sum_{k=1}^{r-1} \left[\partial_t^{(k)} q(x_{i+1/2}, 0+) \right] \frac{\tau^k}{k!} \,. \tag{2.27}$$

We now need to determine the coefficients $\partial_t^{(k)} q(x_{i+1/2}, 0+)$. The Cauchy-Kowalewski method allows us to write

$$\partial_t^{(k)} q(x,t) = (-\lambda)^k \partial_x^{(k)} q(x,t) \ , \tag{2.28}$$

so now the problem is reduced to that of computing space derivatives at $x = x_{i+\frac{1}{2}}$, $\tau = 0+$. To do this we first note that $q^{(k)} \equiv \partial_x^{(k)} q$ obeys the evolution equation in (2.25) and the associated conventional Riemann problem DRP_0 is:

$$\left.\begin{array}{ll} \text{PDE:} & \partial_t q^{(k)} + \lambda \partial_x q^{(k)} = 0 \ , \\ \text{IC:} & q^{(k)}(x,0) = \left\{ \begin{array}{lll} q_L^{(k)} \equiv \partial_x^{(k)} q_L(x_{i+1/2}) & \text{if} & x < x_{i+1/2} \ , \\ q_R^{(k)} \equiv \partial_x^{(k)} q_R(x_{i+1/2}) & \text{if} & x > x_{i+1/2} \ , \end{array} \right. \end{array}\right\} \tag{2.29}$$

whose similarity solution is denoted by $q^{(k)}(x,\tau)$. The sought particular value of this solution is

$$q^{(k)}(x_{i+\frac{1}{2}}, 0+) \ : \ \text{The Godunov state} \ . \tag{2.30}$$

Then, from (2.28) we may write

$$\partial_t^{(k)} q(x_{i+\frac{1}{2}}, 0+) = (-\lambda)^k q^{(k)}(x_{i+\frac{1}{2}}, 0+) \tag{2.31}$$

and thus the expansion (2.27) becomes completely determined, namely

$$q(x_{i+1/2}, \tau) = q(x_{i+1/2}, 0+) + \sum_{k=1}^{r-1} \left[(-\lambda)^k q^{(k)}(x_{i+\frac{1}{2}}, 0+) \right] \frac{\tau^k}{k!} \ . \tag{2.32}$$

Then the flux is computed from (2.21) and (2.22) as

$$f_{i+1/2} = \lambda \left[q(x_{i+1/2}, 0+) + \sum_{k=1}^{r-1} \left[(-\lambda)^k q^{(k)}(x_{i+\frac{1}{2}}, 0+) \right] \frac{\Delta t^k}{(k+1)!} \right] \tag{2.33}$$

and substitution into (2.26) gives the updated solution at the time level $n+1$.

It is informative to fully expand the algebraic expression of the updated solution at the new time level. We obtain

$$\left.\begin{array}{rcl} q_i^{n+1} = q_i^n & - & \dfrac{(\Delta t)_0}{\Delta x} \left(\lambda p_{i+1/2}^{(0)} - \lambda p_{i-1/2}^{(0)} \right) \\ & - & \dfrac{(\Delta t)_1}{\Delta x} \left(\lambda p_{i+1/2}^{(1)} - \lambda p_{i-1/2}^{(1)} \right) \\ & & \cdots \\ & - & \dfrac{(\Delta t)_k}{\Delta x} \left(\lambda p_{i+1/2}^{(k)} - \lambda p_{i-1/2}^{(k)} \right) \\ & & \cdots \\ & - & \dfrac{(\Delta t)_{r-1}}{\Delta x} \left(\lambda p_{i+1/2}^{(r-1)} - \lambda p_{i-1/2}^{(r-1)} \right) \end{array}\right\} \tag{2.34}$$

with

$$p_{i+1/2}^{(k)} = (-\lambda)^k q_{i+1/2}^{(k)}\,, \quad (\Delta t)_k = \frac{(\Delta t)^{k+1}}{(k+1)!}\,. \tag{2.35}$$

First we see that in the case of piece-wise constant representation of the data (no reconstruction) the first line of (2.34) is the Godunov first-order upwind method applied to the state variable $q = \partial_x^{(0)} q$. An immediate thought that comes to mind is to replace the Godunov flux by some more accurate flux, provided it gives a non-oscillatory scheme, such as a TVD flux. We also note that the second line could be interpreted as solving an equation for the evolution of gradients $q^{(1)} = \partial_x^{(1)} q$, also using the Godunov first-order upwind method, and in which the initial condition is given by the two terms on the right-hand side of the first line. Again one could argue that it is obviously better to use a second order TVD flux for this part instead of the first-order Godunov flux. Similar observations apply to the remaining lines of (2.34), leading to the obvious conclusion that for each one of them one should utilize a TVD flux, instead of the first-order Godunov flux.

In other words, in each term of the expansion in the solution of the Derivative Riemann problem DRP_{r-1} we replace the Godunov state (2.30), or its corresponding flux (2.33), by a state or corresponding flux associated with a second-order TVD scheme.

2.3.2. The ADER-WAF scheme for systems

There are several TVD fluxes in the literature, see for example [65]. However, it seems as if not all TVD fluxes would be suitable to our purpose. A key requirement for simplicity is that second-order of accuracy be achieved *without data reconstruction*. To our knowledge the only (upwind) second order TVD flux that satisfies this requirement is the WAF flux, which does not impose any constraints on the boundary extrapolated values $\mathbf{Q}_L^{(k)}(x_{i+1/2})$ and $\mathbf{Q}_R^{(k)}(x_{i+1/2})$ $(k = 0, 1, \ldots, m-1)$. The Weighted Average Flux (WAF) method [61, 63, 62, 65, 5] is a one-step Godunov-type method. Here we describe the WAF flux for an $N \times N$ one-dimensional hyperbolic system. It is defined as

$$\mathbf{F}_{i+1/2}^{WAF} = \frac{1}{\Delta x} \int_{-\Delta x/2}^{\Delta x/2} \mathbf{F}(\mathbf{Q}(x, t^n + \Delta t/2))\, dx\,. \tag{2.36}$$

Assuming the integrand $\mathbf{F}$ to be the solution of the conventional piece-wise constant Riemann problem with $\mathbf{Q}_L \equiv \mathbf{Q}_i^n$, $\mathbf{Q}_R \equiv \mathbf{Q}_{i+1}^n$, we may write

$$\mathbf{F}_{i+1/2}^{WAF} = \frac{1}{2}(\mathbf{F}_i^n + \mathbf{F}_{i+1}^n) - \frac{1}{2}\sum_{k=1}^{N} c_k \Delta \mathbf{F}_{i+1/2}^{(k)}\,, \tag{2.37}$$

where $c_k = \frac{S_k \Delta t}{\Delta x}$ is the Courant number associated with wave k of speed S_k in the solution of the Riemann problem DRP_0 and $\Delta \mathbf{F}^{(k)}_{i+1/2}$ is the jump in $\mathbf{F}$ across wave k.

The TVD (non-oscillatory) version of the WAF flux is given by

$$\mathbf{F}^{WAF}_{i+1/2} = \frac{1}{2}(\mathbf{F}^n_i + \mathbf{F}^n_{i+1}) - \frac{1}{2}\sum_{k=1}^{N} \mathrm{sign}(c_k) A^{(k)}_{i+1/2} \Delta \mathbf{F}^{(k)}_{i+1/2} \, . \tag{2.38}$$

The WAF flux limiter $A^{(k)}_{i+1/2} = A^{(k)}_{i+1/2}(r^{(k)}_{i+1/2})$ depends on the parameter $r^{(k)}_{i+1/2}$, which refers to wave k in the solution of the Riemann problem and is the following ratio

$$r^{(k)}_{i+1/2} = \begin{cases} \Delta q^{(k)}_{i-1/2} / \Delta q^{(k)}_{i+1/2} \, , & \text{if} \quad c_k > 0 \, , \\ \\ \Delta q^{(k)}_{i+3/2} / \Delta q^{(k)}_{i+1/2} \, , & \text{if} \quad c_k < 0 \, . \end{cases} \tag{2.39}$$

Here q is a suitable variable which changes across each wave family in the solution of the Riemann problem; $\Delta q^{(k)}_{l+1/2}$ denotes the jump in the variable q across wave k in the self-similar solution $\mathbf{Q}_{l+1/2}(\xi, \tau)$ in the Riemann problem with data $(\mathbf{Q}^n_l, \mathbf{Q}^n_{l+1})$.

Another possible version of WAF is obtained by first defining an weighted average state

$$\mathbf{Q}_{i+1/2} = \frac{1}{2}(\mathbf{Q}^n_i + \mathbf{Q}^n_{i+1}) - \frac{1}{2}\sum_{k=1}^{N} \mathrm{sign}(c_k) A^{(k)}_{i+1/2} \Delta \mathbf{Q}^{(k)}_{i+1/2} \tag{2.40}$$

and then obtaining an associated flux as $\mathbf{F}_{i+1/2} = \mathbf{F}(\mathbf{Q}_{i+1/2})$. Further details are found in [65].

For a non-linear system the proposed ADER-WAF scheme utilizes a WAF flux (2.38) or state (2.40), instead of the Godunov flux or state, in every term of the solution (1.2) of the DRP (1.1). It is immediately obvious that in the limiting case of no reconstruction (piece-wise constant data), our schemes reduce to a second-order TVD scheme, whereas the conventional schemes reduce to a first-order monotone scheme, the underlying scheme used as the building block.

2.3.3. Some implementation issues

A couple of remarks on implementation issues are in order. These are particularly relevant for long time evolution problems. The first remark concerns the nonlinear WENO weights used in the solution reconstruction. The design of these weights involves a small parameter ϵ used to avoid division by zero [22]. Usually one takes $\epsilon = 10^{-6}$. We find, however, that for the ADER and ADER-WAF methods, especially for the third order versions, it is preferable to use a smaller value. We normally take $\epsilon = 10^{-24}$ for these schemes.

The second remark concerns the computation of the ratio $r = N/D$ in (2.39), where N is the numerator and D is the denominator. This requires special attention when the denominator D is small, $|D| \leq \delta$, say, where δ is a small positive number. For TVD methods, experience shows that the robustness of the methods does not depend too crucially on the way this step is handled, while accuracy does. The following two procedures are usually applied:

$$r = \frac{N}{D + \delta} \,, \tag{2.41}$$

$$r = \frac{\hat{N}}{\hat{D}} \,, \quad \hat{X} = \begin{cases} \delta \, \mathrm{sign}(1, X) \,, & if \quad |X| \leq \delta \,, \\ X \,, & \text{otherwise} \,, \end{cases} \tag{2.42}$$

where $X = N, D$. Procedure (2.42) leads to more accurate results and it can be easily seen that for nearly uniform flow $r \approx 1$, leading to second order accuracy, the correct behaviour of a TVD scheme. This is not the case with procedure (2.41), which results in larger artificial diffusion. There is a third procedure given by

$$r = \begin{cases} \dfrac{N}{D} \,, & if \quad |D| \geq \delta \,, \\ 0 \,, & \text{otherwise} \,. \end{cases} \tag{2.43}$$

For the computations reported in this thesis, procedure (2.42) was used successfully, except for a particular case, namely the linear advection equation for the fourth order ADER-WAF scheme for a long time evolution as applied to the linear advection equation. For such case procedure (2.43) was applied with satisfactory results. It seems to us as if the implementation of TVD criteria in the construction of very high-order methods may require some further investigations.

2.4. ADER schemes in three space dimensions

Consider the following three-dimensional nonlinear system of conservation laws:

$$\partial_t \mathbf{Q} + \partial_x \mathbf{F}(\mathbf{Q}) + \partial_y \mathbf{G}(\mathbf{Q}) + \partial_z \mathbf{H}(\mathbf{Q}) = \mathbf{S}(x, y, z, t, \mathbf{Q}). \tag{2.44}$$

Integration of (2.44) over a space-time control volume of dimensions $\Delta x = x_{i+1/2} - x_{i-1/2}$, $\Delta y = y_{j+1/2} - y_{j-1/2}$, $\Delta z = z_{k+1/2} - z_{k-1/2}$, $\Delta t = t^{n+1} - t^n$ produces the following one-step finite-volume scheme:

$$\begin{aligned} \mathbf{Q}_{ijk}^{n+1} = \mathbf{Q}_{ijk}^{n} \quad & + \frac{\Delta t}{\Delta x} \left(\mathbf{F}_{i-1/2,jk} - \mathbf{F}_{i+1/2,jk} \right) + \frac{\Delta t}{\Delta y} \left(\mathbf{G}_{i,j-1/2,k} - \mathbf{G}_{i,j+1/2,k} \right) \\ & + \frac{\Delta t}{\Delta z} \left(\mathbf{H}_{ij,k-1/2} - \mathbf{H}_{ij,k+1/2} \right) + \Delta t \mathbf{S}_{ijk}, \end{aligned} \tag{2.45}$$

where $\mathbf{Q}_{ijk}^n$ is the cell average of the solution at time level t^n:

$$\mathbf{Q}_{ijk}^n = \frac{1}{\Delta x}\frac{1}{\Delta y}\frac{1}{\Delta z}\int_{x_{i-1/2}}^{x_{i+1/2}}\int_{y_{j-1/2}}^{y_{j+1/2}}\int_{z_{k-1/2}}^{z_{k+1/2}}\mathbf{Q}(x,y,z,t^n)\,dz\,dy\,dx, \tag{2.46}$$

$\mathbf{F}_{i+1/2,jk}$, $\mathbf{G}_{i,j+1/2,k}$ and $\mathbf{H}_{ij,k+1/2}$ are the space-time averages of the physical fluxes at the cell interfaces:

$$\begin{aligned}
\mathbf{F}_{i+1/2,jk} &= \frac{1}{\Delta t}\frac{1}{\Delta y}\frac{1}{\Delta z}\int_{y_{j-1/2}}^{y_{j+1/2}}\int_{z_{k-1/2}}^{z_{k+1/2}}\int_{t^n}^{t^{n+1}}\mathbf{F}(\mathbf{Q}(x_{i+1/2},y,z,\tau))\,d\tau\,dz\,dy,\\
\mathbf{G}_{i,j+1/2,k} &= \frac{1}{\Delta t}\frac{1}{\Delta x}\frac{1}{\Delta z}\int_{x_{i-1/2}}^{x_{i+1/2}}\int_{z_{k-1/2}}^{z_{k+1/2}}\int_{t^n}^{t^{n+1}}\mathbf{G}(\mathbf{Q}(x,y_{i+1/2},z,\tau))\,d\tau\,dz\,dx,\\
\mathbf{H}_{ij,k+1/2} &= \frac{1}{\Delta t}\frac{1}{\Delta x}\frac{1}{\Delta y}\int_{x_{i-1/2}}^{x_{i+1/2}}\int_{y_{j-1/2}}^{y_{j+1/2}}\int_{t^n}^{t^{n+1}}\mathbf{H}(\mathbf{Q}(x,y,z_{i+1/2},\tau))\,d\tau\,dy\,dx.
\end{aligned} \tag{2.47}$$

and $\mathbf{S}_{ijk}$ is space-time average of the source term:

$$\mathbf{S}_{ijk} = \frac{1}{\Delta t}\frac{1}{\Delta x}\frac{1}{\Delta y}\frac{1}{\Delta z}\int_{t^n}^{t^{n+1}}\int_{x_{i-1/2}}^{x_{i+1/2}}\int_{y_{j-1/2}}^{y_{j+1/2}}\int_{z_{k-1/2}}^{z_{k+1/2}}\mathbf{S}(x,y,z,t,\mathbf{Q})\,dz\,dy\,dx\,dt. \tag{2.48}$$

Here $\tau = t - t^n$ is local time.

While describing the procedure to evaluate the numerical flux in three space dimensions we concentrate on $\mathbf{F}_{i+1/2,jk}$; the expressions for $\mathbf{G}_{i,j+1/2,k}$ and $\mathbf{H}_{ij,k+1/2}$ are obtained in an entirely analogous manner.

The evaluation of the ADER numerical flux $\mathbf{F}_{i+1/2,jk}$ consists of the following steps. First we discretize the spatial integrals over the cell faces in (2.47) using a tensor product of a suitable Gaussian numerical quadrature. The expression for the numerical flux in the x coordinate direction then reads

$$\mathbf{F}_{i+1/2,jk} = \sum_{\alpha=1}^{N}\sum_{\beta=1}^{N}\left(\frac{1}{\Delta t}\int_{t^n}^{t^{n+1}}\mathbf{F}(\mathbf{Q}(x_{i+1/2},y_\alpha,z_\beta,\tau))d\tau\right)K_\beta\,K_\alpha, \tag{2.49}$$

where y_α, z_β are the integration points over the cell face $[y_{j-1/2},y_{j+1/2}]\times[z_{k-1/2},z_{k+1/2}]$ and K_α, K_β are the weights. Normally, we use the two-point Gaussian quadrature for third and fourth order schemes and a higher-order Gaussian quadrature for fifth and higher order schemes.

Next we reconstruct the point-wise values of the solution and all derivatives up to order $r-1$ from cell averages at the Gaussian integration points $(x_{i+1/2},y_\alpha,z_\beta)$ by means of the dimension-by-dimension WENO reconstruction. For general information

on reconstruction in the context of the two-dimensional ENO and WENO schemes see [7, 21]. Extension to three space dimensions in the context of ADER schemes can be found in [68]. See Section 2.1 for more details.

After the reconstruction is carried out for each Gaussian integration point (y_α, z_β) at the cell face we pose the Derivative Riemann problem (1.1) in the x-coordinate direction (normal to the cell boundary) and obtain a high order approximation to $\mathbf{Q}(x_{i+1/2}, y_\alpha, z_\beta, \tau)$. All steps of the solution procedure remain *essentially* as in the one-dimensional case. We write Taylor series expansion in time

$$\mathbf{Q}(x_{i+1/2}, y_\alpha, z_\beta, \tau) = \mathbf{Q}(x_{i+1/2}, y_\alpha, z_\beta, 0+) + \sum_{k=1}^{r-1} \left[\frac{\partial^k}{\partial t^k} \mathbf{Q}(x_{i+1/2}, y_\alpha, z_\beta, 0+) \right] \frac{\tau^k}{k!}. \tag{2.50}$$

The leading term $\mathbf{Q}(x_{i+1/2}, y_\alpha, z_\beta, 0+)$ is the Godunov state of the conventional *augmented* Riemann problem

$$\left. \begin{array}{c} \partial_t \mathbf{Q} + \partial_x \mathbf{F}(\mathbf{Q}) = \mathbf{0}, \\ \mathbf{Q}(x,0) = \left\{ \begin{array}{lll} \mathbf{Q}_L(x_{i+1/2}, y_\alpha, z_\beta) & \text{if} & x < x_{i+1/2}, \\ \mathbf{Q}_R(x_{i+1/2}, y_\alpha, z_\beta) & \text{if} & x > x_{i+1/2}, \end{array} \right. \end{array} \right\} \tag{2.51}$$

To evaluate higher-order terms we first express all time derivatives by spatial derivatives by means of the Cauchy-Kowalewski procedure. We note that this procedure will now involve mixed x, y and z derivatives up to order $r-1$. For the system in conservation form (2.44) we have

$$\begin{aligned}
\partial_t \mathbf{Q} &= -\left(\frac{\partial \mathbf{F}}{\partial \mathbf{Q}}\right) \partial_x \mathbf{Q} - \left(\frac{\partial \mathbf{G}}{\partial \mathbf{Q}}\right) \partial_y \mathbf{Q} - \left(\frac{\partial \mathbf{H}}{\partial \mathbf{Q}}\right) \partial_z \mathbf{Q}, \\
\partial_{tx} \mathbf{Q} &= -\left(\frac{\partial^2 \mathbf{F}}{\partial \mathbf{Q^2}}\right) (\partial_x \mathbf{Q})^2 - \left(\frac{\partial \mathbf{F}}{\partial \mathbf{Q}}\right) \partial_{xx} \mathbf{Q} - \left(\frac{\partial^2 \mathbf{G}}{\partial \mathbf{Q^2}}\right) (\partial_x \mathbf{Q})(\partial_y \mathbf{Q}) - \left(\frac{\partial \mathbf{G}}{\partial \mathbf{Q}}\right) \partial_{xy} \mathbf{Q} \\
&\quad - \left(\frac{\partial^2 \mathbf{H}}{\partial \mathbf{Q^2}}\right) (\partial_x \mathbf{Q})(\partial_z \mathbf{Q}) - \left(\frac{\partial \mathbf{H}}{\partial \mathbf{Q}}\right) \partial_{xz} \mathbf{Q}, \\
\partial_{ty} \mathbf{Q} &= -\left(\frac{\partial^2 \mathbf{F}}{\partial \mathbf{Q^2}}\right) (\partial_y \mathbf{Q})(\partial_x \mathbf{Q}) - \left(\frac{\partial \mathbf{F}}{\partial \mathbf{Q}}\right) \partial_{xy} \mathbf{Q} - \left(\frac{\partial^2 \mathbf{G}}{\partial \mathbf{Q^2}}\right) (\partial_y \mathbf{Q})^2 - \left(\frac{\partial \mathbf{G}}{\partial \mathbf{Q}}\right) \partial_{yy} \mathbf{Q} \\
&\quad - \left(\frac{\partial^2 \mathbf{H}}{\partial \mathbf{Q^2}}\right) (\partial_y \mathbf{Q})(\partial_z \mathbf{Q}) - \left(\frac{\partial \mathbf{H}}{\partial \mathbf{Q}}\right) \partial_{yz} \mathbf{Q}, \\
\partial_{tz} \mathbf{Q} &= -\left(\frac{\partial^2 \mathbf{F}}{\partial \mathbf{Q^2}}\right) (\partial_z \mathbf{Q})(\partial_x \mathbf{Q}) - \left(\frac{\partial \mathbf{F}}{\partial \mathbf{Q}}\right) \partial_{xz} \mathbf{Q} - \left(\frac{\partial^2 \mathbf{G}}{\partial \mathbf{Q^2}}\right) (\partial_z \mathbf{Q})(\partial_y \mathbf{Q}) - \left(\frac{\partial \mathbf{G}}{\partial \mathbf{Q}}\right) \partial_{yz} \mathbf{Q} \\
&\quad - \left(\frac{\partial^2 \mathbf{H}}{\partial \mathbf{Q^2}}\right) (\partial_z \mathbf{Q})^2 - \left(\frac{\partial \mathbf{H}}{\partial \mathbf{Q}}\right) \partial_{zz} \mathbf{Q}, \\
\partial_{tt} \mathbf{Q} &= -\left(\frac{\partial^2 \mathbf{F}}{\partial \mathbf{Q^2}}\right) (\partial_t \mathbf{Q})(\partial_x \mathbf{Q}) - \left(\frac{\partial \mathbf{F}}{\partial \mathbf{Q}}\right) \partial_{tx} \mathbf{Q} - \left(\frac{\partial^2 \mathbf{G}}{\partial \mathbf{Q^2}}\right) (\partial_t \mathbf{Q})(\partial_y \mathbf{Q}) - \left(\frac{\partial \mathbf{G}}{\partial \mathbf{Q}}\right) \partial_{ty} \mathbf{Q} \\
&\quad - \left(\frac{\partial^2 \mathbf{H}}{\partial \mathbf{Q^2}}\right) (\partial_t \mathbf{Q})(\partial_z \mathbf{Q}) - \left(\frac{\partial \mathbf{H}}{\partial \mathbf{Q}}\right) \partial_{tz} \mathbf{Q}
\end{aligned}$$

and so on. An optimized FORTRAN or C output can be produced using algebraic manipulators and then can be directly included into the actual code.

In an entirely analogous way to the one-dimensional case, we can derive evolution equations and the initial conditions for each spatial derivative

$$\mathbf{Q}^{(m+n+l)} \equiv \frac{\partial^{m+n+l}}{\partial x^m \partial y^n \partial z^l}\mathbf{Q}, \quad 1 \leq m+n+l \leq r-1$$

by differentiating the governing equation (2.44) and the reconstruction polynomials $\mathbf{Q}_L$, $\mathbf{Q}_R$ with respect to x. The evolution equations have exactly the same form as (1.7) with a difference. The right hand side will now depend not only on lower order x derivatives but also on mixed derivatives. For the Taylor expansion (2.50) we need the values at $x = x_{i+1/2}$, $\tau = 0$. Therefore, entirely analogous to the one-dimensional case, we neglect the source term, linearize the equation around the leading term of the time expansion (2.50) and replace the piece-wise polynomial initial data by the left and right extrapolated values. The spatial derivatives at $(x - x_{i+1/2})/\tau = 0$ are then the Godunov states of the following linearised Riemann problem with piece-wise constant initial data:

$$\begin{gathered}
\partial_t \left(\mathbf{Q}^{(m+n+l)}\right) + \mathbf{A}_{i+1/2}\, \partial_x \left(\mathbf{Q}^{(m+n+l)}\right) = 0, \\
\mathbf{A}_{i+1/2} = \mathbf{A}(\mathbf{Q}(x_{i+1/2}, y_\alpha, z_\beta, 0+)), \\
\mathbf{Q}^{(m+n+l)} = \begin{cases} \dfrac{\partial^{m+n+l}}{\partial x^m \partial y^n \partial z^l}\mathbf{Q}_L(x_{i+1/2}, y_\alpha, z_\beta), & x < x_{i+1/2} \\ \dfrac{\partial^{m+n+l}}{\partial x^m \partial y^n \partial z^l}\mathbf{Q}_R(x_{i+1/2}, y_\alpha, z_\beta), & x > x_{i+1/2} \end{cases}
\end{gathered} \tag{2.52}$$

After solving (2.52) for $1 \leq m+n+l \leq r-1$ we form the Taylor expansion (2.50) for the interface state at the Gaussian integration point $(x_{i+1/2}, y_\alpha, z_\beta)$. The flux of *the state-expansion* ADER scheme is obtained by inserting the approximate state (2.50) into formula (2.49) and using an appropriate r^{th}-order accurate quadrature for time integration:

$$\mathbf{F}_{i+1/2,jk} = \sum_{\alpha=1}^{N}\sum_{\beta=1}^{N}\left(\sum_{l=1}^{N}\mathbf{F}(\mathbf{Q}(x_{i+1/2}, y_\alpha, z_\beta, \tau_l))K_l\right)K_\beta\, K_\alpha. \tag{2.53}$$

For the *flux expansion* ADER schemes we write the Taylor time expansion of the physical flux at each point $(x_{i+1/2},\, y_\alpha,\, z_\beta)$

$$\mathbf{F}(x_{i+1/2}, y_\alpha, z_\beta, \tau) = \mathbf{F}(x_{i+1/2}, y_\alpha, z_\beta, 0+) + \sum_{k=1}^{r-1}\left[\frac{\partial^k}{\partial t^k}\mathbf{F}(x_{i+1/2}, y_\alpha, z_\beta, 0+)\right]\frac{\tau^k}{k!}. \tag{2.54}$$

From (2.47) and (2.54) the numerical flux is given by

$$\begin{aligned}\mathbf{F}_{i+1/2,jk} &= \sum_{\alpha=1}^{N}\sum_{\beta=1}^{N}\mathbf{F}(x_{i+1/2},y_\alpha,z_\beta,0+)K_\alpha K_\beta \\ &\quad+\sum_{k=1}^{r-1}\left[\frac{\partial^k}{\partial t^k}\mathbf{F}(x_{i+1/2},y_\alpha,z_\beta,0+)\right]\frac{\Delta t^k}{(k+1)!}K_\alpha K_\beta\,.\end{aligned} \tag{2.55}$$

Entirely analogous to the one-dimensional case, the leading term $\mathbf{F}(x_{i+1/2},y_\alpha,z_\beta,0+)$ is computed from (2.51) using a monotone upwind flux. The remaining higher order time derivatives of the flux in (2.54) are expressed via time derivatives of the intercell state $\mathbf{Q}(x_{i+1/2},y_\alpha,z_\beta,\tau)$ which are given by the Taylor expansion (2.50).

As in the one-dimensional case, when a conventional approximate-state Riemann solver is not available, the leading term $\mathbf{Q}(0+,0)$ is now given by the EVILIN Riemann solver (1.13). The leading term of the flux expansion $\mathbf{F}(x_{i+1/2},0+)$ is given by the GMUSTA flux. Other options again include the use of conventional upwind fluxes, see [53] for details. No numerical quadrature is then required to compute the numerical flux.

The computation of the numerical source now involves four-dimensional integrals. First we use the tensor-product of the N-point Gaussian rule to discretize the three-dimensional space integral in (2.48) so that the expression for s_{ijk} reads

$$\mathbf{S}_{ijk}=\sum_{\alpha=1}^{N}\sum_{\beta=1}^{N}\sum_{\gamma=1}^{N}\left(\frac{1}{\Delta t}\int_{t^n}^{t^{n+1}}\mathbf{S}(x_\alpha,y_\beta,z_\gamma,\tau,q(x_\alpha,y_\beta,z_\gamma,\tau))d\tau\right)K_\gamma K_\beta K_\alpha. \tag{2.56}$$

Then we reconstruct values and all spatial derivatives, including mixed derivatives, of q at the Gaussian integration point in $x-y-z$ space for the time level t^n. Note that these points are different from flux integration points over cell faces. The reconstruction procedure is entirely analogous to that for the flux evaluation. Next for each Gaussian point $(x_\alpha,y_\beta,z_\gamma)$ we perform the Cauchy-Kowalewski procedure and replace time derivatives by space derivatives. As a result we have high-order approximations to $\mathbf{Q}(x_\alpha,y_\beta,z_\gamma,\tau)$. Finally, we carry out numerical integration in time using the Gaussian quadrature:

$$\mathbf{S}_{ijk}=\sum_{\alpha=1}^{N}\sum_{\beta=1}^{N}\sum_{\gamma=1}^{N}\left(\sum_{l=1}^{N}\mathbf{S}(x_\alpha,y_\beta,z_\gamma,\tau_l,\mathbf{Q}(x_\alpha,y_\beta,z_\gamma,\tau_l))K_l\right)K_\gamma K_\beta K_\alpha. \tag{2.57}$$

The solution is advanced in time by updating the cell averages according to the one-step formula (2.45).

Conclusion

In this chapter we first presented a brief description of the WENO reconstruction procedure. Expressions for higher order reconstructions as well as extension to three spatial extension were given. Next, we described the ADER approach as applied to the multidimensional nonlinear systems of conservation laws with source terms. In the one-dimensional case a special, more accurate version of the scheme, called ADER-WAF, was developed.

We remark that the ADER approach provides the upwind approximation of the source term due to the nice coupling of the flux and the source via the Taylor time expansion. A detailed study of this aspect of the schemes is subject of the ongoing research.

3. *Truncation error and stability analysis*

Introduction

Despite significant advances in the development of the ADER schemes made in recent years, little analysis of their properties has been done. So far only linear schemes with a centred stencil have been studied [17]. Here we analyze stability properties and truncation errors of the more general finite-volume ADER schemes on structured meshes as applied to the linear advection equation with constant coefficients in one, two and three spatial dimensions. The stability of linear ADER schemes is studied by means of the von Neumann method. Due to the significant complexity of the resulting expressions for the amplification factor we adopt the idea of [12, 70] to verify the stability condition numerically rather than analytically. The truncation error analysis is carried out for linear ADER schemes in one, two and three space dimensions. In one space dimension we additionally analyze the nonlinear ADER schemes as well as special ADER-WAF methods [75, 77].

The chapter is organized as follows. In In Section 3.1 we analyze one-dimensional schemes, both linear and nonlinear, including ADER-TVD scheme. In Section 3.2 we study two-dimensional schemes. Analysis of the three-dimensional case is given in Section 3.3.

We restrict ourselves to the Cauchy problem only and do not study the stability of the schemes with respect to the boundary conditions.

3.1. One-dimensional schemes

3.1.1. Framework

We now consider the model linear advection equation:

$$\frac{\partial v}{\partial t} + \frac{\partial f(v)}{\partial x} = 0, \quad f = av, \tag{3.1}$$

where $a > 0$ is the constant propagation speed. The ADER schemes are written as follows:

$$v_i^{n+1} = v_i^n - \frac{\Delta t}{\Delta x}(f_{i+1/2} - f_{i-1/2}). \tag{3.2}$$

In one spatial dimension the most general formulation is the flux-expansion ADER-WAF scheme [75, 77]. Let $P_i(x)$ and $P_{i+1}(x)$ be the left and right reconstruction

polynomials for calculating the intercell flux $f_{i+1/2}$. Then when applied to (3.1) the ADER-WAF flux reads as follows:

$$f_{i+1/2} = \frac{a}{2}\sum_{k=0}^{r-1}\frac{(-1)^k a^k \Delta t^k}{(k+1)!}\left[(1+\varphi^{(k)}_{i+1/2})\frac{d^k P_i}{dx^k}(x_{i+1/2}) + (1-\varphi^{(k)}_{i+1/2})\frac{d^k P_{i+1}}{dx^k}(x_{i+1/2})\right]. \tag{3.3}$$

Here the WAF flux limiter $\varphi^{(k)}_{i+1/2}$ is calculated separately for each spatial derivative. The ADER-WAF scheme thus may contain two nonlinearities: one is due to the TVD limiter $\varphi^{(k)}_{i+1/2}$ and another is due to the possible use of the nonlinear, solution-adaptive reconstruction. A particular choice of the flux limiter $\varphi \equiv \mathrm{sign}a$ gives the conventional upwind ADER schemes [49], both linear and nonlinear.

In general, it is very difficult, if possible, to analyze the scheme when a TVD limiter is used due to the fact that the limiter does not depend continuously on data. Therefore, we restrict our analysis to the following simplified variant of the scheme:

$$\varphi^{(k)}_{i+1/2} \equiv \varphi = \mathrm{const}.$$

The expression for the flux (3.3) takes the following form:

$$\begin{aligned} f_{i+1/2} \;=\; & \frac{a}{2}(1+\varphi)\sum_{k=0}^{r-1}\frac{(-1)^k a^k \Delta t^k}{(k+1)!}\frac{d^k}{dx^k}P_i(x_{i+1/2}) \\ & +\frac{a}{2}(1-\varphi)\sum_{k=0}^{r-1}\frac{(-1)^k a^k \Delta t^k}{(k+1)!}\frac{d^k}{dx^k}P_{i+1}(x_{i+1/2}). \end{aligned} \tag{3.4}$$

In order to avoid confusion with the complete ADER-WAF version, given by (3.3), we call the scheme with the flux (3.4) the ADER-φ scheme. The flux (3.4) differs from (3.3) in that φ depends neither on the interface position $x_{i+1/2}$ nor on the order of the spatial derivative k. However, this simplified ADER-φ scheme does include the conventional ADER $\varphi = \mathrm{sign}a$ as well as the case of the second order Lax-Wendroff flux $\varphi \equiv K_x = a\Delta t/\Delta x$ as the building block for each term in the flux expansion (3.3). Therefore, it allows us to study the effect of using higher-order building blocks in the ADER schemes. We remark that nonlinearity of the scheme may still be present due to the adaptive reconstruction procedure.

The description of ADER flux (3.4) is complete once the expressions for the reconstruction polynomials are provided. The simplest one-dimensional ADER scheme is the linear scheme with the fixed-stencil reconstruction and the first-order upwind flux as the building block ($\varphi = \mathrm{sign}a$). Recall that for the rth order scheme we need to have a reconstruction polynomial of order $r-1$. For a given cell i there are r polynomials $p_i^{(l)}$ constructed from the stencils $S_l = (i-l, \ldots, i+r-l)$. Here

$l = 0, 1, \ldots r$ is the shift of the stencil with the respect to the index i. We denote by $f^{(l)}_{i+1/2}$ the ADER flux which is obtained by setting $P_i(x) = p^{(l)}_i(x)$ and $\varphi = \mathrm{sign} a$:

$$f^{(l)}_{i+1/2} = a \sum_{k=0}^{r-1} \frac{(-1)^k a^k \Delta t^k}{(k+1)!} \frac{d^k}{dx^k} p^{(l)}_i(x_{i+1/2}), \quad a > 0. \tag{3.5}$$

ADER-φ schemes use the more accurate weighted essentially non-oscillatory (WENO) reconstruction procedure to obtain the reconstructed values of the solution at the cell interface position, see [22, 3] and references therein. The basic WENO idea is to combine all r reconstruction polynomials to build up a more accurate reconstruction polynomial:

$$P_i(x) = \sum_{l=0}^{r} d_l p^{(l)}_i(x), \tag{3.6}$$

where the so-called optimal weights d_k are taken from [22, 3]. Note, that the weights are tied up to the specific choice of the reconstruction point $x = x_{i+1/2}$ and are different for $P_i(x_{i+1/2} - 0)$ and $P_{i+1}(x_{i+1/2} + 0)$, see [22]. In the nonlinear version of the scheme the linear weights d_k are replaced by the nonlinear, solution-adaptive WENO weights ω_k given by [22]

$$\alpha_k = \frac{d_k}{(\epsilon + \beta_k)^p}, \quad \omega_k = \frac{\alpha_k}{\sum\limits_k \alpha_l}, \quad \beta_l = \sum_{k=1}^{r-1} \left(\frac{d^k p^{(l)}_i(x)}{dx^k} \right)^2 \Delta x^{2k-1}.$$

Here β_k are the so-called smoothness indicators, p is a parameter which ensures that the discontinuous stencils are assigned small weights. We use a typical value $p = 2$. We remark that the leading term of the truncation error of these schemes does not depend on the value of p. A small constant ϵ is added to avoid division by zero. For the purpose of analysis we set $\epsilon = 0$. Finally, the reconstruction polynomials obtained by replacing linear weights in (3.6) by nonlinear weights ω_k:

$$P_i(x) = \sum_{l=0}^{r} \omega_l p^{(l)}_i(x). \tag{3.7}$$

It follows from the linearity of the advection equation that for a given order of accuracy r the description of ADER-φ schemes is complete once we provide expressions for the fixed-stencil fluxes $f^{(l)}_{i+1/2}$.

Note, that the flux of the r^{th} order ADER scheme with WENO reconstruction uses for reconstruction a combination of r polynomials of order $r-1$. The stencils of these polynomials form a larger stencil of $2r-1$ cells from which one can construct

a polynomial of higher order $s = 2r - 2$ and use it for the flux evaluation. The corresponding scheme ADERr-s scheme will have the same r^{th} order of temporal accuracy but a higher order spatial discretization. It is therefore interesting to study its properties and compare it with other ADER schemes.

In the rest of the section for a given order of temporal accuracy r we analyze three families of the ADER schemes: i) fixed stencil ADERr schemes with $p_i^{(l)}(x)$ polynomials; ii) ADERr-s schemes with polynomials of order $s = 2r-2$; iii) ADER-φ schemes with linear (3.6) and nonlinear (3.7) WENO reconstructions. Depending on the choice of φ we may have conventional ADERr schemes ($\varphi = \text{sign}a$) and as well as ADER schemes with the Lax-Wendroff flux, denoted by ADERr-LW ($\varphi = K_x$)

3.1.2. Description of the schemes

Second-order schemes

Linear second-order fixed-stencil schemes use piece-wise linear reconstruction. We have two schemes, which we call centred-stencil ($l = 0$) and upwind-biased ($l = 1$). The corresponding second-order fluxes are given by

$$f_{i+1/2}^{(0)} = \frac{1}{2}\, a\,(1 + K_x)\, v_j + \frac{1}{2}\, a\,(1 - K_x)\, v_{j+1}. \tag{3.8}$$

$$f_{i+1/2}^{(1)} = \frac{1}{2}\, a\,(K_x - 1)\, v_{j-1} + \frac{1}{2}\, a\,(3 - K_x)\, v_j. \tag{3.9}$$

Here $K_x \equiv a\Delta t/\Delta x$ is the CFL number in x spatial direction. Obviously, (3.8) is the flux of the Law-Wendroff scheme whereas (3.9) is the flux of the Warming-Beam scheme.

Next, we consider the second-order ADER2-3 scheme, which has the same stencil as scheme (3.6) but uses a fixed parabolic polynomial for reconstruction. The expression for the corresponding flux takes the form

$$f_{i+1/2} = \frac{1}{6} a\left[-v_{j-1} + (5 + 3\,K_x)\, v_j + (2 - 3\,K_x)\, v_{j+1}\right]. \tag{3.10}$$

The flux of ADER2-φ scheme can be obtained from (3.4) and is omitted.

Third-order schemes

Third-order fixed-stencil schemes use parabolic reconstruction polynomials. We have three schemes, which we call downwind-biased ($l = 0$), upwind-biased ($l = 1$) and

one-sided upwind ($l = 2$). The corresponding third-order fluxes are given by

$$f^{(0)}_{i+1/2} = a\left[\left(\frac{1}{3}+\frac{1}{2}K_x+\frac{1}{6}K_x^2\right)v_i+\left(\frac{5}{6}-\frac{1}{2}K_x-\frac{1}{3}K_x^2\right)v_{i+1}+\left(-\frac{1}{6}+\frac{1}{6}K_x^2\right)v_{i+2}\right] \quad (3.11)$$

$$f^{(1)}_{i+1/2} = a\left[\left(-\frac{1}{6}+\frac{1}{6}K_x^2\right)v_{i-1}+\left(\frac{5}{6}+\frac{1}{2}K_x-\frac{1}{3}K_x^2\right)v_i+\left(\frac{1}{3}-\frac{1}{2}K_x+\frac{1}{6}K_x^2\right)v_{i+1}\right] \quad (3.12)$$

$$f^{(2)}_{i+1/2} = a\left[\left(\frac{1}{3}-\frac{1}{2}K_x+\frac{1}{6}K_x^2\right)v_{i-2}+\left(-\frac{7}{6}+\frac{3}{2}K_x-\frac{1}{3}K_x^2\right)v_{i-1}+\left(\frac{11}{6}-K_x+\frac{1}{6}K_x^2\right)v_i\right] \quad (3.13)$$

The flux of the ADER3-φ scheme with weighted piece-wise parabolic reconstruction [22] can be obtained from (3.4) and is omitted.

Finally, we consider the third-order ADER3-5 scheme, which has the same stencil as scheme (3.6) but uses a fixed fourth-order polynomial for reconstruction. The expression for the third-order ADER flux takes the form

$$\begin{aligned} f_{i+1/2} &= a\left[\left(\frac{1}{30}-\frac{1}{24}{K_x}^2\right)v_{i-2}+\left(\frac{1}{4}{K_x}^2-\frac{13}{60}-\frac{1}{24}K_x\right)v_{i-1}+\right. \\ &\left(\frac{47}{60}-\frac{1}{3}{K_x}^2+\frac{5}{8}K_x\right)v_i+\left(\frac{9}{20}+\frac{1}{12}{K_x}^2-\frac{5}{8}K_x\right)v_{i+1}+ \\ &\left.\left(\frac{1}{24}{K_x}^2-\frac{1}{20}+\frac{1}{24}K_x\right)v_{i+2}\right] \end{aligned} \quad (3.14)$$

The stencil of the ADER3-5 scheme consists of six cells and is upwind-biased.

Fourth-order schemes

Fourth-order fixed-stencil schemes use piece-wise cubic reconstruction. There are now four candidate schemes: downwind-biased ($l = 0$), symmetric or centred ($l = 1$), upwind-biased ($l = 2$) and one-sided upwind ($l = 3$). The corresponding fourth-order fluxes are given by

$$\begin{aligned} f^{(0)}_{i+1/2} &= a\left[\left(\frac{1}{24}{K_x}^3+\frac{1}{4}+\frac{1}{4}{K_x}^2+\frac{11}{24}K_x\right)v_i+\left(\frac{13}{12}-\frac{1}{8}{K_x}^3-\frac{7}{12}{K_x}^2-\frac{3}{8}K_x\right)v_{i+1}+\right. \\ &\left.\left(\frac{1}{8}{K_x}^3-\frac{5}{12}+\frac{5}{12}{K_x}^2-\frac{1}{8}K_x\right)v_{i+2}+\left(\frac{1}{24}K_x-\frac{1}{24}{K_x}^3+\frac{1}{12}-\frac{1}{12}{K_x}^2\right)v_{i+3}\right] \end{aligned} \quad (3.15)$$

$$\begin{aligned} f^{(1)}_{i+1/2} &= a\left[\left(\frac{1}{24}{K_x}^3-\frac{1}{12}+\frac{1}{12}{K_x}^2-\frac{1}{24}K_x\right)v_{i-1}+\left(\frac{7}{12}-\frac{1}{8}{K_x}^3-\frac{1}{12}{K_x}^2+\frac{5}{8}K_x\right)v_i+\right. \\ &\left.\left(\frac{7}{12}+\frac{1}{8}{K_x}^3-\frac{1}{12}{K_x}^2-\frac{5}{8}K_x\right)v_{i+1}+\left(\frac{1}{24}K_x-\frac{1}{24}{K_x}^3-\frac{1}{12}+\frac{1}{12}{K_x}^2\right)v_{i+2}\right] \end{aligned} \quad (3.16)$$

$$f^{(2)}_{i+1/2} = a\left[\left(\frac{1}{24}K_x{}^3 - \frac{1}{24}K_x + \frac{1}{12} - \frac{1}{12}K_x{}^2\right)v_{i-2} + \left(\frac{1}{8}K_x - \frac{1}{8}K_x{}^3 - \frac{5}{12} + \frac{5}{12}K_x{}^2\right)v_{i-1} + \left(\frac{1}{8}K_x{}^3 + \frac{13}{12} - \frac{7}{12}K_x{}^2 + \frac{3}{8}K_x\right)v_i + \left(\frac{1}{4} - \frac{1}{24}K_x{}^3 + \frac{1}{4}K_x{}^2 - \frac{11}{24}K_x\right)v_{i+1}\right] \tag{3.17}$$

$$f^{(3)}_{i+1/2} = a\left[\left(\frac{1}{24}K_x{}^3 + \frac{11}{24}K_x - \frac{1}{4} - \frac{1}{4}K_x{}^2\right)v_{i-3} + \left(\frac{13}{12} - \frac{1}{8}K_x{}^3 + \frac{11}{12}K_x{}^2 - \frac{15}{8}K_x\right)v_{i-2} + \left(\frac{1}{8}K_x{}^3 - \frac{23}{12} - \frac{13}{12}K^2 + \frac{23}{8}K_x\right)v_{i-1} + \left(-\frac{1}{24}K_x{}^3 + \frac{25}{12} + \frac{5}{12}K_x{}^2 - \frac{35}{24}K_x\right)v_i\right] \tag{3.18}$$

For the fourth order schemes with WENO reconstruction we limit our analysis to the linear ADER4-φ. The expressions for the corresponding flux and scheme are omitted.

Finally, we can construct the fourth-order ADER4-7 scheme, which has the same stencil as scheme (3.4) with WENO reconstruction but uses a fixed six-order polynomial for reconstruction. The expression for the flux is omitted.

3.1.3. Stability analysis

The von Neumann stability analysis of the linear versions of our schemes is performed as follows. We consider a *trial solution* $v_i^n = A^n \exp(Ii\alpha)$, where A is the amplitude, $\alpha = P\Delta x$ is the phase angle, P is the wave number (not to be confused with the reconstruction polynomial), $\lambda = 2\pi/P$ is the wave length and $I = \sqrt{-1}$ is the unit complex number. We now write down the schemes in the following concise form:

$$v_i^{n+1} = \sum_l b_l v_{i+l}^n,$$

where b_l are the coefficients of the schemes. Inserting the trial solution in the expression above we obtain the following algebraic expression for the modulus of the amplitude A:

$$|A|^2 = \left(\sum_l b_l \cos(l\alpha)\right)^2 + \left(\sum_l b_l \sin(l\alpha)\right)^2. \tag{3.19}$$

A necessary condition for stability is $|A| \leq 1$. However, the resulting algebraic expression for the modulus of the amplification factor (3.19) is rather complicated and untractable for algebraic analysis. We therefore verify the condition $|A| \leq 1$ numerically rather than analytically by evaluating $|A|$ for many values of the phase angle α. This would give us a good and reliable indication of the stability region of the scheme. See [12, 70] for more details on this procedure.

We summarize the results of the stability study in Tables 5–7. Let us first discuss the linear schemes with fixed-stencil reconstructions. We observe that the downwind-biased schemes are unconditionally unstable, which is to be expected. Other third order schemes are stable under a conventional stability condition $K_x \leq 1$. For the second and fourth order schemes the situation is more complicated. The upwind-biased second order scheme and centred stencil fourth order scheme are stable under a conventional stability condition $K_x \leq 1$. The second order scheme with the one-sided upwind stencil and fourth order scheme with the upwind-biased stencil have an enlarged stability region $K_x \leq 2$ which is twice that of the Godunov scheme. Finally, the one-sided upwind fourth-order scheme has a very unusual stability condition $1 \leq K_x \leq 3$, which renders it impractical. Therefore, the stability regions of schemes of even and odd orders of accuracy are quite different.

N	Description	Stability condition
Fixed-stencil schemes		
1.	Upwind-biased (3.8)	$K_x \leq 1$
2.	One-sided upwind (3.9)	$K_x \leq 2$
3.	ADER2-3 (3.10)	$K_x \leq 0.72$
Schemes with linear WENO reconstruction		
4.	ADER2	$K_x \leq 1.0$
5.	ADER2-LW	unstable
Schemes with nonlinear WENO reconstruction		
6.	ADER2	$K_x \leq 1$ (experiments with the scheme)
7.	ADER2-WAF	$K_x \leq 1$ (experiments with the scheme)

Table 5 . Stability conditions for one-dimensional second-order schemes

We now proceed to analyze the schemes with increased orders of spatial accuracy. We observe that compared to the fixed-stencil versions ADER2-3, ADER3-5 and ADER4-7 schemes have reduced stability regions. The loss of stability region is again expected and has been observed for other schemes in which the temporal accuracy does not match the spatial accuracy. However, given the possible increase in accuracy over fixed-stencil schemes, this reduction of the admissible CFL numbers is justified.

Next we look at the linear schemes with WENO reconstruction. We observe that the second order ADER2 scheme has a conventional stability region $K_x \leq 1$

N	Description	Stability condition
Fixed-stencil schemes		
1.	Downwind-biased	unstable for all K_x
2.	Upwind-biased (3.12)	$K_x \leq 1$
3.	One-sided upwind (3.13)	$K_x \leq 1$
4.	ADER3-5 (3.14)	$K_x \leq 0.85$
Schemes with linear WENO reconstruction		
5.	ADER3	$K_x \leq 0.4$
6.	ADER3-LW	unstable
Schemes with nonlinear WENO reconstruction		
7.	ADER3	$K_x \leq 1$ (experiments with the scheme)
8.	ADER3-WAF	$K_x \leq 1$ (experiments with the scheme)

Table 6 . Stability conditions for one-dimensional third-order schemes

whereas higher order schemes have a reduced stability region $K_x \leq 0.4$ for ADER3 and $K_x \leq 0.2$ for ADER4. Moreover, the linear ADER2-LW and ADER3-LW schemes are unstable. We remark, however, that for both schemes the maximum value of $|A|$ is only slightly larger than unity in the region $0 \leq K_x \leq 1$. The linear ADER4-LW scheme is stable with a very stringent stability condition $K_x \leq 0.08$.

Finally, we discuss the stability condition of the nonlinear ADER schemes using the nonlinear WENO reconstruction. The above spectral stability analysis is valid for linear schemes only. For nonlinear schemes we have investigated the stability for the special initial data in the form of an isolated harmonic wave and found that the nonlinear ADER schemes are stable up to $K_x = 1$. The same analysis shows that the nonlinear ADER3-LW is still unstable for small K_x, but its instability becomes less severe. Therefore, we estimate the stability condition of the nonlinear schemes ADER-WAF from numerical experiments. After exhaustive study for both smooth and discontinuous solutions we find that these schemes are stable under a conventional stability condition $K_x \leq 1$. Therefore, despite the fact that the linear schemes are unstable, the nonlinear versions are indeed stable.

We remark that it is not unusual that the nonlinear version of the scheme is stable when the linear one is not. For example, see [25] for the spatially second order Godunov schemes which nonlinear non-oscillatory versions are proven to be stable but linear ones are unconditionally unstable.

N	Description	Stability condition
1.	Downwind-biased	unstable for all K_x
2.	Centred	stable for $K_x \leq 1$
3.	Upwind-biased	stable for $K_x \leq 2$
4.	One-sided upwind	stable for $1 \leq K_x \leq 3$
5.	ADER4-7 scheme	stable for $K_x \leq 1.2$
Schemes with linear WENO reconstruction		
6.	ADER4	stable for $K_x \leq 0.2$
7.	ADER4-LW	stable for $K_x \leq 0.08$
Schemes with nonlinear WENO reconstruction		
8.	ADER4	$K_x \leq 1$ (experiments with the scheme)
9.	ADER4-WAF	$K_x \leq 1$ (experiments with the scheme)

Table 7 . Stability conditions for one-dimensional fourth-order schemes

3.1.4. Truncation error analysis

The accuracy of the schemes can be analyzed by studying the leading term $\epsilon(\Delta x, \Delta t)$ of their truncation errors, which in the one-dimensional case can be written as:

$$\epsilon(\Delta x, \Delta t) = a\,\Phi(K_x)\Delta x^r \left(\frac{\partial^{r+1}}{\partial x^{r+1}}\, v(x_i, t^n) \right). \tag{3.20}$$

Here r is the order of the scheme. The accuracy of different schemes of a given order r can be compared by studying the coefficients $\Phi(K_x)$ of the leading term.

In Tables 8–10 we list expressions for $\Phi(K_x)$ for all schemes. Additionally, we plot $\Phi(K_x)$ against the CFL number for third and fourth order schemes in Figs. 3.1, 3.2.

N	Description	$\Phi(K_x)$
1.	Upwind-biased (3.8)	$\frac{1}{6}(1 - K_x^2)$
3.	One-sided upwind (3.9)	$\frac{1}{6}(2 - 3\,K_x + K_x^2)$
4.	ADER2-3 (3.10)	$-\frac{1}{6}K_x^6$
5.	linear ADER2-φ	$\frac{1}{6}K_x\,(\varphi - K_x)$
5.	nonlinear ADER2-φ	$\frac{1}{6}\,K_x\,(\varphi - K_x)$

Table 8 . $\Phi(K_x)$ functions for one-dimensional second-order schemes

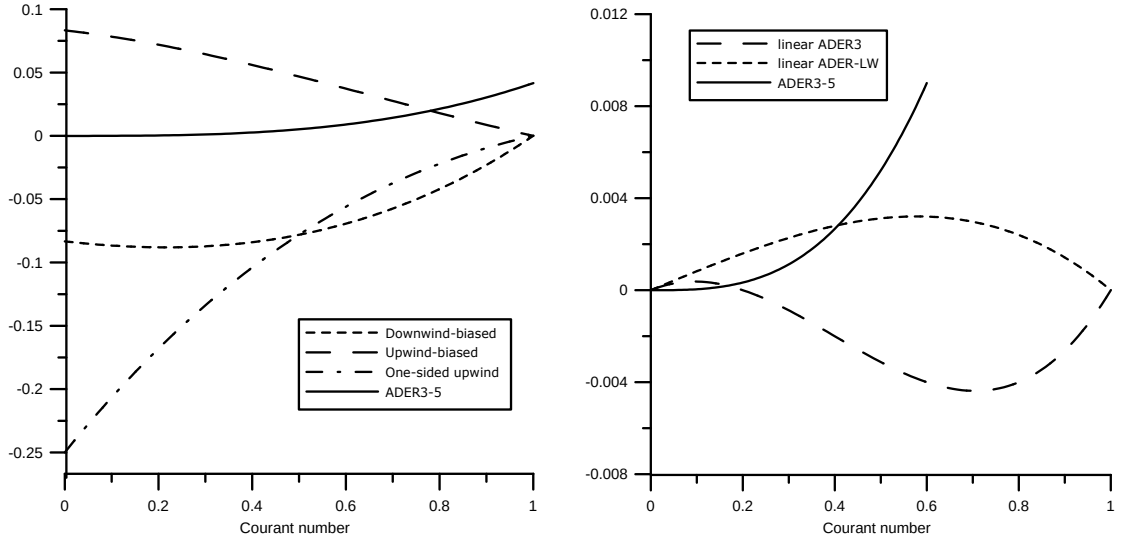

Figure 3.1. $\Phi(K_x)$ functions for ADER3 schemes with different reconstructions. Left- scheme with fixed-polynomial reconstruction, right - schemes with weighted reconstruction

Let us first discuss the results for the linear schemes with a fixed-stencil reconstruction. For a fixed order of accuracy r these schemes differ only by the shift of the stencil l with respect to the cell i. We observe that the one-sided upwind schemes have the largest error among the schemes considered, whereas the one-sided downwind scheme for $r = 3$ and the scheme with the centred stencil for $r = 4$ have the smallest error. The upwind-biased schemes have an average accuracy. For the special case $K_x = 1$ the leading term of the truncation error vanishes for all schemes. It can also be easily seen from the expressions for v_i^{n+1} that the schemes actually produce the exact solution $v_i^{n+1} \equiv v_{i-1}^n$ for this special case.

Next we look at the ADER2-3, ADER3-5 and ADER4-7 schemes which are constructed by using a higher-order polynomial while keeping the temporal accuracy r equal to that of the fixed-stencil schemes. It is obvious, that the overall formal order of accuracy is not increased by increasing the spatial accuracy. However, from Figs. 3.1, 3.2 it is clear that the actual error of these two schemes is considerably smaller than that of the fixed-stencil schemes for Courant numbers $0 \leq K_x \leq 0.7$. For larger K_x the ADER3-5 and ADER4-7 schemes become unstable. Therefore, the use of the ADER2-3, ADER3-5 and ADER4-7 schemes is recommended for moderate and small CFL numbers only.

Finally, we consider the linear and nonlinear ADER-φ schemes with WENO reconstruction. Firstly, we observe that there is no difference in the leading term of

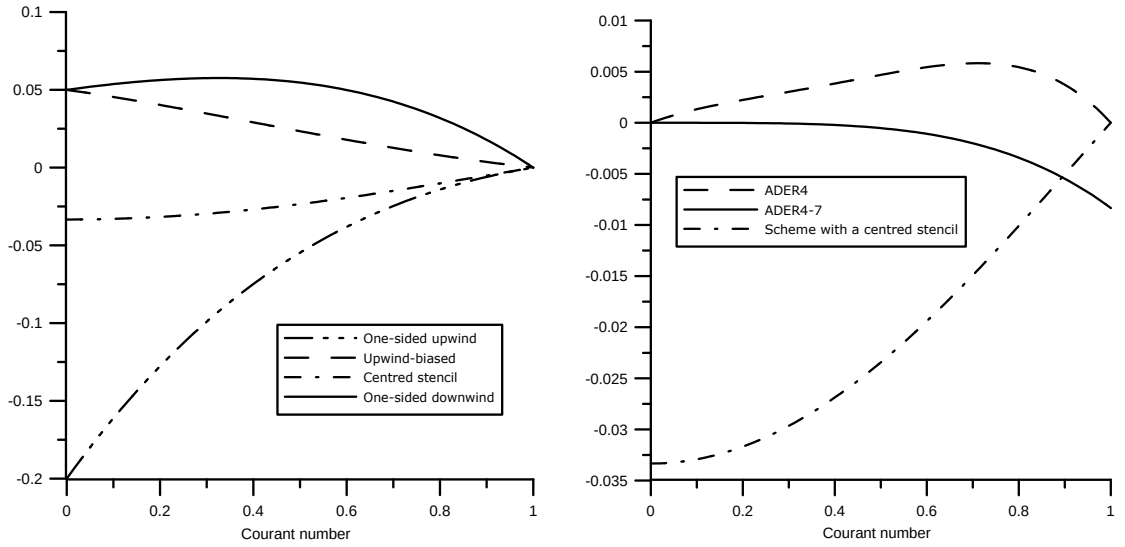

Figure 3.2. $\Phi(K_x)$ functions for ADER4 schemes with different reconstructions. Left- scheme with fixed-polynomial reconstruction, right - schemes with weighted reconstruction

the truncation error between a scheme with linear and nonlinear WENO reconstruction. The truncation error vanishes for $K_x = 1$. Secondly, we conclude that all schemes with WENO reconstruction are significantly more accurate than the corresponding schemes with fixed-stencil reconstruction. As compared to the ADERr-s schemes the use of WENO reconstruction improves the accuracy for large K_x close to unity. Finally, we see that the use of the weighted flux instead of the first-order upwind flux as the building block does not affect the accuracy of the scheme for all φ. Moreover, the second order scheme becomes third order in the case $\varphi = K_x$.

3.1.5. Other schemes

We have also studied the fifth-order scheme with an upwind-biased stencil ($l = 2$). The coefficient of the leading term of the truncation error of this fixed-stencil scheme is given by

$$\Phi(K_x) = \frac{1}{720}\left(K_x^5 - 3\,K_x^4 - 5K_x^3 + 15\,K_x^2 + 4\,K_x - 12\right)$$

For a special case $K_x = 1$ the truncation error vanishes, which can also be seen from the expression for the scheme, omitted here. The scheme is stable under a conventional condition $K_x \leq 1$.

N	Description	$\Phi(K_x)$
Fixed-stencil schemes		
1.	Downwind-biased (3.11)	$\frac{1}{24}\,(K_x^3 + 2\,K_x^2 - K_x - 2)$
2.	Upwind-biased (3.12)	$\frac{1}{24}\,(K_x^3 - 2\,K_x^2 - K_x + 2)$
3.	One-sided upwind (3.13)	$\frac{1}{24}\,(K_x^3 - 6\,K_x^2 + 11\,K_x - 6)$
4.	ADER3-5 (3.14)	$\frac{1}{24}\,K_x^3$
5.	linear ADER3-φ	$\frac{1}{120}\,K\,(5\,K_x^2 - 6\,K_x\varphi + 1)$
6.	non-linear ADER3-φ	$\frac{1}{120}\,K\,(5\,K_x^2 - 6\,K_x\varphi + 1)$

Table 9 . $\Phi(K_x)$ functions for one-dimensional third-order schemes

N	Description	$\Phi(K_x)$
1.	One-sided downwind	$-\frac{1}{120}\,(K_x^4 + 5\,K_x^3 + 5\,K_x^2 - 5\,K_x - 6)$
2.	Centred	$-\frac{1}{120}\,(K_x^4 - 5\,K_x^2 + 4)$
3.	Upwind-biased	$-\frac{1}{120}\,(K_x^4 - 5\,K_x^3 + 5\,K_x^2 + 5\,K_x - 6)$
4.	One-sided upwind	$-\frac{1}{120}\,(K_x^4 - 10\,K_x^3 + 35\,K_x^2 - 50\,K_x + 24)$
5.	ADER4-7 scheme	$-\frac{1}{120}\,K_x^4$
6.	Linear ADER4-φ	$\frac{1}{840}\,K_x\,(-7\,K_x^3 + 10\,\varphi\,K_x^2 - 5\,K_x + 2\,\varphi)$

Table 10 . $\Phi(K_x)$ functions for one-dimensional fourth-order schemes

3.2. Two-dimensional schemes

3.2.1. Framework

Consider the model two-dimensional linear advection equation

$$\frac{\partial v}{\partial t} + \frac{\partial f(v)}{\partial x} + \frac{\partial g(v)}{\partial y} = 0, \quad f = av, \quad g = bv, \tag{3.21}$$

where $a, b > 0$ are constant propagation speeds. The schemes now read:

$$v_{ij}^{n+1} = v_{ij}^n - \frac{\Delta t}{\Delta x}(f_{i+1/2,j} - f_{i-1/2,j}) - \frac{\Delta t}{\Delta y}(g_{i,j+1/2} - g_{i,j-1/2}). \tag{3.22}$$

Generally speaking, the spatial integral of the cell side in the numerical flux should be approximated numerically, using a Gaussian quadrature. However, in this section we study fixed-stencil schemes only. In this case for the linear advection

equation we can use the exact spatial integration in the expression for the numerical fluxes.

Suppose the reconstruction polynomial of order $r-1$ for the cell i,j is given by $P_{ij}(x,y)$. For the linear constant coefficient equation in the case $a>0$ the solution of the DRP problem becomes trivial. In Riemann problems (2.51), (2.52) the solution is equal to the left initial state. The final expression for the fixed-stencil flux $f_{i+1/2,j}$ of order r reads [72]:

$$f_{i+1/2,j} = \frac{a}{\Delta y} \int\limits_{y_{j-1/2}}^{y_{j+1/2}} \left(\sum_{k=0}^{r-1} \left(-a\frac{d}{dx} - b\frac{d}{dy} \right)^k \frac{\Delta t^k}{(k+1)!} P_{ij}(x_{i+1/2}, y) \right) dy. \tag{3.23}$$

It is obvious from (3.23) that the solution of the DRP problem does include all mixed spatial derivatives up to the order $r-1$.

The construction of the reconstruction polynomial of order $r-1$ for the r^{th} order scheme requires the use of the two-dimensional stencil with cells

$$(i-l_x, \ldots, i-l_x+r) \times (j-l_y, \ldots, j-l_y+r),$$

where l_x, l_y are shifts of the stencil with respect to the cell i,j in the x and y coordinate directions, respectively. Performing the exact integration over the cell side, we obtain the following expression for the two-dimensional fixed-stencil ADER flux in the x coordinate direction:

$$f_{i+1/2,j} = a \sum_{\alpha} \sum_{\beta} W_{\alpha,\beta}\, v_{i+\alpha,j+\beta}, \tag{3.24}$$

where $W_{\alpha,\beta}$ are the coefficients which depend on the CFL coefficients $K_x = a\Delta t/\Delta x$, $K_y = b\Delta t/\Delta y$.

The flux in the y direction is formulated in an entirely analogous way and can be obtained from (3.24) by interchanging x and y directions.

Substituting $f_{i+1/2,j}$ and $g_{i,j+1/2}$ into the conservative update formula (3.22), we obtain the expression for the scheme.

3.2.2. Description of the schemes

Second-order schemes

We study the second order ADER scheme with MUSCL-type piece-wise linear reconstruction [25, 27] with the reconstruction polynomial given by:

$$P_{ij}(x,y) = v_{ij} + S_x(x-x_i) + S_y(y-y_j), \tag{3.25}$$

where S_x, S_y are slopes in the x and y coordinate directions correspondingly. We choose the centred slopes:

$$S_x = \frac{v_{i+1,j} - v_{i-1,j}}{2\Delta x}, \quad S_y = \frac{v_{ij+1} - v_{ij-1}}{2\Delta y}.$$

The corresponding ADER flux is given by

$$W_{-1,0} = \frac{1}{4}\,K_x - \frac{1}{4}, \quad W_{0,-1} = \frac{1}{4}K_y, \quad W_{0,0} = 1, \quad W_{0,1} = -\frac{1}{4}K_y, \quad W_{1,0} = -\frac{1}{4}K_x + \frac{1}{4}.$$

and is in fact the flux of the unsplit MUSCL-Hancock scheme with centred slopes, see [65].

Third-order schemes

The third order upwind-biased scheme with the parabolic reconstruction polynomial corresponds to the choice $l_x = l_y = 1$. The resulting third-order upwind-biased ADER flux in the x coordinate direction is given by the following non-zero coefficients $W_{\alpha,\beta}$:

$$W_{-1,-1} = \left(-\frac{1}{36}\,{K_y}^2 - \frac{1}{24}\,K_y\right), \quad W_{-1,0} = \left(-\frac{1}{6} + \frac{1}{18}\,{K_y}^2 + \frac{1}{6}\,{K_x}^2\right),$$

$$W_{-1,1} = \left(-\frac{1}{36}\,{K_y}^2 + \frac{1}{24}\,K_y\right), \quad W_{0,-1} = \left(\frac{5}{36}\,{K_y}^2 + \frac{5}{24}\,K_y + \frac{1}{6}\,K_x\,K_y\right),$$

$$W_{0,0} = \left(-\frac{5}{18}\,{K_y}^2 + \frac{5}{6} + \frac{1}{2}\,K_x - \frac{1}{3}\,{K_x}^2\right), \quad W_{0,1} = \left(\frac{5}{36}\,{K_y}^2 - \frac{5}{24}\,K_y - \frac{1}{6}\,K_x\,K_y\right),$$

$$W_{1,-1} = \left(\frac{1}{18}\,{K_y}^2 + \frac{1}{12}\,K_y - \frac{1}{6}\,K_x\,K_y\right), \quad W_{1,0} = \left(\frac{1}{3} - \frac{1}{9}\,{K_y}^2 + \frac{1}{6}\,{K_x}^2 - \frac{1}{2}\,K_x\right),$$

$$W_{1,1} = \left(\frac{1}{18}\,{K_y}^2 - \frac{1}{12}\,K_y + \frac{1}{6}\,K_x\,K_y\right).$$

Another scheme we studied is a scheme with a higher order cubic reconstruction from the fourth order version but third-order time discretization with $l_x = l_y = 2$. The resulting scheme is denoted as the ADER3-4 scheme. The coefficients $W_{\alpha,\beta}$ are given by:

$$W_{-2,-2} = -\frac{1}{144}K_y + \frac{1}{216}K_xK_y, \quad W_{-2,-1} = \frac{1}{24}K_y - \frac{1}{36}K_xK_y + \frac{1}{72}K_y^2,$$

$$W_{-2,0} = -\frac{1}{24}K_x - \frac{1}{48}K_y + \frac{1}{72}K_xK_y - \frac{1}{36}K_y^2 - \frac{1}{12}K_x^2 + \frac{1}{12},$$

$$W_{-2,1} = \frac{1}{108}K_xK_y - \frac{1}{72}K_y + \frac{1}{72}K_y^2, \quad W_{-1,-2} = -\frac{1}{72}K_xK_y + \frac{5}{144}K_y,$$

$$W_{-1,-1} = \frac{1}{12}K_xK_y - \frac{5}{24}K_y - \frac{5}{72}K_y^2,$$

$$W_{-1,0} = -\frac{5}{12} - \frac{1}{24}K_xK_y + \frac{5}{48}K_y + \frac{5}{36}K_y^2 + \frac{5}{12}K_x^2 + \frac{1}{8}K_x,$$

$$W_{-1,1} = -\frac{1}{36}K_xK_y + \frac{5}{72}K_y - \frac{5}{72}K_y^2,$$

$$W_{0,-2} = -\frac{13}{144}K_y - \frac{1}{24}K_xK_y, \quad W_{0,-1} = \frac{1}{4}K_xK_y + \frac{13}{24}K_y + \frac{13}{72}K_y^2,$$

$$W_{0,0} = \frac{3}{8}K_x - \frac{13}{48}K_y + \frac{13}{12} - \frac{1}{8}K_xK_y - \frac{13}{36}K_y^2 - \frac{7}{12}K_x^2,$$

$$W_{0,1} = -\frac{13}{72}K_y - \frac{1}{12}K_xK_y + \frac{13}{72}K_y^2,$$

$$W_{1,-2} = -\frac{1}{48}K_y + \frac{11}{216}K_xK_y, \quad W_{1,-1} = \frac{1}{8}K_y - \frac{11}{36}K_xK_y + \frac{1}{24}K_y^2,$$

$$W_{1,0} = \frac{11}{72}K_xK_y + \frac{1}{4} - \frac{1}{12}K_y^2 - \frac{1}{16}K_y + \frac{1}{4}K_x^2 - \frac{11}{24}K_x,$$

$$W_{1,1} = \frac{11}{108}K_xK_y - \frac{1}{24}K_y + \frac{1}{24}K_y^2.$$

Fourth-order schemes

We consider two fourth order schemes with cubic reconstruction polynomials. The first scheme is upwind-biased which corresponds to the choice $l_x = l_y = 2$. The flux coefficients $W_{\alpha,\beta}$, $\alpha = -2, \ldots, 1$, $\beta = -2, \ldots, 1$, are given by

$$W_{-2,-2} = \left(\frac{1}{216}\,K_x\,K_y + \frac{1}{96}\,{K_x}^2Ky + \frac{1}{288}\,{K_y}^3 - \frac{1}{144}\,K_y\right),$$

$$W_{-2,-1} = \left(-\frac{1}{36}\,K_x\,K_y - \frac{1}{16}\,{K_x}^2K_y - \frac{1}{96}\,{K_y}^2K_x - \frac{1}{96}\,{K_y}^3 + \frac{1}{72}\,{K_y}^2 + \frac{1}{24}\,Ky\right)$$

$$\begin{aligned} W_{-2,0} \;=\; & \left(\frac{1}{12} - \frac{1}{24}\,K_x - \frac{1}{12}\,Kx^2 + \frac{1}{24}\,{K_x}^3 + \frac{1}{32}\,{K_x}^2K_y\right. \\ & \left. + \frac{1}{72}\,K_x\,K_y + \frac{1}{48}\,{K_y}^2K_x + \frac{1}{96}\,{K_y}^3 - \frac{1}{36}\,{K_y}^2 - \frac{1}{48}\,K_y\right) \end{aligned}$$

$$W_{-2,+1} = \left(\frac{1}{48}\,{K_x}^2K_y + \frac{1}{108}\,K_x\,K_y - \frac{1}{96}\,{K_y}^2K_x - \frac{1}{288}\,{K_y}^3 + \frac{1}{72}\,{K_y}^2 - \frac{1}{72}\,K_y\right)$$

$$W_{-1,-2} = \left(-\frac{5}{96}\,{K_x}^2K_y - \frac{1}{72}\,K_x\,Ky - \frac{5}{288}\,{K_y}^3 + \frac{5}{144}\,K_y\right)$$

$$W_{-1,-1} = \left(\frac{5}{16}\,{K_x}^2K_y + \frac{1}{12}\,K_x\,K_y + \frac{1}{32}\,{K_y}^2K_x - \frac{5}{24}\,K_y + \frac{5}{96}\,{K_y}^3 - \frac{5}{72}\,{K_y}^2\right)$$

$$
\begin{aligned}
W_{-1,0} &= \left(\frac{1}{8}\,K_x - \frac{5}{12} + \frac{5}{12}\,{K_x}^2 - \frac{5}{32}\,{K_x}^2 K_y - \frac{1}{24}\,K_x\,K_y \right.\\
&\quad \left. -\frac{1}{16}\,{K_y}^2 K_x - \frac{1}{8}\,{K_x}^3 - \frac{5}{96}\,{K_y}^3 + \frac{5}{36}\,{K_y}^2 + \frac{5}{48}\,K_y\right)\\
W_{-1,1} &= \left(-\frac{5}{48}\,{K_x}^2 K_y - \frac{1}{36}\,K_x\,K_y + \frac{1}{32}\,{K_y}^2 K_x + \frac{5}{288}\,{K_y}^3 - \frac{5}{72}\,{K_y}^2 + \frac{5}{72}\,K_y\right),\\
W_{0,-2} &= \left(-\frac{13}{144}\,K_y + \frac{13}{288}\,{K_y}^3 + \frac{7}{96}\,{K_x}^2 K_y - 1/24\,K_x\,K_y\right),\\
W_{0,-1} &= \left(-\frac{13}{96}\,{K_y}^3 + \frac{13}{24}\,K_y + \frac{13}{72}\,{K_y}^2 + \frac{1}{4}\,K_x\,K_y - \frac{7}{16}\,{K_x}^2 K_y + \frac{3}{32}\,{K_y}^2 K_x\right),\\
W_{0,0} &= \left(\frac{3}{8}\,K_x + \frac{13}{12} - \frac{13}{48}\,K_y + \frac{1}{8}\,{K_x}^3 + \frac{13}{96}\,{K_y}^3 - \frac{13}{36}\,{K_y}^2 - \frac{7}{12}\,{K_x}^2 \right.\\
&\quad \left. +\frac{7}{32}\,{K_x}^2 K_y - \frac{1}{8}\,K_x\,K_y - \frac{3}{16}\,{K_y}^2 K_x\right),\\
W_{0,1} &= \left(-\frac{13}{72}\,K_y + \frac{13}{72}\,{K_y}^2 - \frac{13}{288}\,{K_y}^3 + \frac{7}{48}\,{K_x}^2 K_y - \frac{1}{12}\,K_x\,K_y + \frac{3}{32}\,{K_y}^2 K_x\right),\\
W_{1,-2} &= \left(-\frac{1}{32}\,{K_x}^2 K_y + \frac{11}{216}\,K_x\,K_y + \frac{1}{96}\,{K_y}^3 - \frac{1}{48}\,K_y\right),\\
W_{1,-1} &= \left(\frac{3}{16}\,{K_x}^2 K_y - \frac{11}{36}\,K_x\,K_y - \frac{11}{96}\,{K_y}^2 K_x + \frac{1}{24}\,{K_y}^2 + \frac{1}{8}\,K_y - \frac{1}{32}\,Ky^3\right),\\
W_{1,0} &= \left(-\frac{11}{24}\,K_x + \frac{1}{4} + \frac{1}{4}\,{K_x}^2 + \frac{11}{72}\,K_x\,K_y - \frac{3}{32}\,{K_x}^2 K_y \right.\\
&\quad \left. +\frac{11}{48}\,{K_y}^2 K_x - \frac{1}{24}\,Kx^3 - \frac{1}{12}\,{K_y}^2 + \frac{1}{32}\,{K_y}^3 - \frac{1}{16}\,K_y\right),\\
W_{1,1} &= \left(-\frac{1}{16}\,{K_x}^2 K_y + \frac{11}{108}\,K_x\,K_y - \frac{11}{96}\,{K_y}^2 Kx + 1/24\,{K_y}^2 - \frac{1}{96}\,{K_y}^3 - \frac{1}{24}\,K_y\right).
\end{aligned}
$$

The second fourth order scheme we study uses the centred reconstruction in the normal direction (x direction for $f_{i+1/2,j}$), which corresponds to the choice $l_x = l$. In the y direction we still use $l_y = 1$. This scheme will be referred to as as ADER4 with the centred stencil. The coefficients $W_{\alpha,\beta}$ are given by:

$$
\begin{aligned}
W_{-1,-1} &= -\frac{1}{288}K_y^3 - \frac{1}{72}K_y - \frac{1}{7}K_y^2 - \frac{1}{96}K_y^2 K_x - \frac{1}{108}K_x K_y + \frac{1}{48}K_x^2 K_y,\\
W_{-1,0} &= \frac{1}{36}K_y^2 + \frac{1}{96}K_y^3 - \frac{1}{48}K_y - \frac{1}{24}K_x + \frac{1}{24}K_x^3 + \frac{1}{12}K_x^2\\
&\quad -\frac{1}{12} + \frac{1}{48}K_y^2 K_x + \frac{1}{32}K_x^2 K_y - \frac{1}{72}K_x K_y,\\
W_{-1,1} &= \frac{1}{24}K_y - \frac{1}{96}K_y^3 - \frac{1}{96}K_y^2 K_x - \frac{1}{16}K_x^2 K_y + \frac{1}{36}K_x K_y - \frac{1}{72}K_y^2,
\end{aligned}
$$

$$W_{-1,2} = \frac{1}{288}K_y^3 - \frac{1}{144}K_y + \frac{1}{96}K_x^2K_y - \frac{1}{216}K_xK_y,$$
$$W_{0,-1} = \frac{7}{72}K_y + \frac{7}{288}K_y^3 + \frac{7}{72}K_y^2 + \frac{5}{32}K_y^2K_x - \frac{1}{48}K_x^2K_y + \frac{5}{36}K_xK_y,$$
$$W_{0,0} = -\frac{7}{96}K_y^3 + \frac{5}{8}K_x - \frac{1}{8}K_x^3 - \frac{1}{12}K_x^2 + \frac{7}{48}K_y + \frac{7}{12}$$
$$-\frac{5}{16}K_y^2K_x - \frac{1}{32}K_x^2K_y + \frac{5}{24}K_xK_y - \frac{7}{36}K_y^2,$$
$$W_{0,1} = -\frac{7}{24}K_y + \frac{7}{96}K_y^3 + \frac{5}{32}K_y^2K_x + \frac{1}{16}K_x^2K_y - \frac{5}{12}K_xK_y + \frac{7}{72}K_y^2,$$
$$W_{0,2} = -\frac{7}{288}K_y^3 - \frac{1}{96}K_x^2K_y + \frac{5}{72}K_xK_y + \frac{7}{144}K_y,$$
$$W_{1,-1} = \frac{7}{288}K_y^3 + \frac{7}{72}K_y - \frac{5}{32}K_y^2K_x - \frac{5}{36}K_xK_y - \frac{1}{48}K_x^2K_y + \frac{7}{72}K_y^2,$$
$$W_{1,0} = -\frac{7}{36}K_y^2 + \frac{7}{48}K_y - \frac{7}{96}K_y^3 + \frac{1}{8}K_x^3 - \frac{5}{8}K_x - \frac{1}{12}K_x^2 + \frac{7}{12}$$
$$+\frac{5}{16}K_y^2K_x - \frac{1}{32}K_x^2K_y - \frac{5}{24}K_xK_y,$$
$$W_{1,1} = -\frac{7}{24}K_y + \frac{7}{96}K_y^3 + \frac{7}{72}K_y^2 - \frac{5}{32}K_y^2K_x + \frac{5}{12}K_xK_y + \frac{1}{16}K_x^2K_y,$$
$$W_{1,2} = -\frac{7}{288}K_y^3 + \frac{7}{144}K_y - \frac{1}{96}K_x^2K_y - \frac{5}{72}K_xK_y,$$
$$W_{2,-1} = -\frac{1}{72}K_y - \frac{1}{288}K_y^3 + \frac{1}{96}K_y^2K_x + \frac{1}{108}K_xK_y + \frac{1}{48}K_x^2K_y - \frac{1}{72}K_y^2,$$
$$W_{2,0} = -\frac{1}{48}K_y + \frac{1}{24}K_x - \frac{1}{24}K_x^3 + \frac{1}{12}K_x^2 + \frac{1}{96}K_y^3$$
$$-\frac{1}{48}K_y^2K_x - \frac{1}{12} + \frac{1}{32}K_x^2K_y + \frac{1}{36}K_y^2 + \frac{1}{72}K_xK_y,$$
$$W_{2,1} = \frac{1}{24}K_y - \frac{1}{96}K_y^3 - \frac{1}{72}K_y^2 + \frac{1}{96}K_y^2K_x - \frac{1}{16}K_x^2K_y - \frac{1}{36}K_xK_y,$$
$$W_{2,2} = \frac{1}{288}K_y^3 - \frac{1}{144}K_y + \frac{1}{216}K_xK_y + \frac{1}{96}K_x^2K_y.$$

3.2.3. Stability analysis

The von Neumann stability analysis of our schemes can be performed as follows. We consider a *trial solution* $v_{ij}^n = A^n \exp(I(i\alpha + j\beta)$, where A is the amplitude, α and β are phase angles in the x and y directions. We now write down the schemes in the following concise form:

$$v_{ij}^{n+1} = \sum_{lm} b_{lm} v_{i+l,j+m}^n, \quad a, b > 0, \tag{3.26}$$

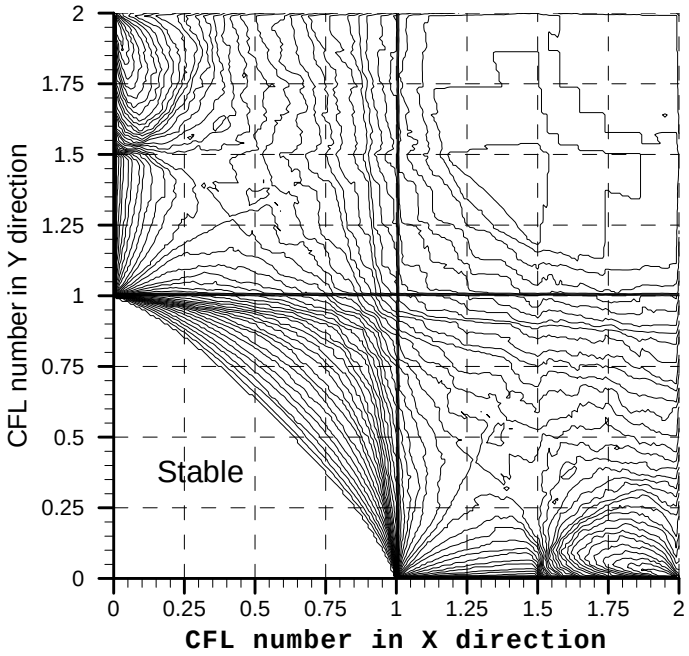

Figure 3.3. Stability plot for the two-dimensional ADER3 scheme

where b_{lm} are the coefficients of the schemes. Inserting the trial solution in the expression above we obtain the following algebraic expression for the square of the module of A:

$$|A|^2 = \left(\sum_{lm} b_{lm} \cos\left(l\alpha + m\beta\right) \right)^2 + \left(\sum_{lm} b_{lm} \sin\left(l\alpha + m\beta\right) \right)^2 . \tag{3.27}$$

A necessary condition for stability is $|A| \leq 1$. The complexity of the algebraic expression for the amplification factor in two space dimension does not allow an analytical study. Instead we again perform a numerical study to get an *indication* of the stability of the scheme.

We proceed as follows. For a given pair (K_x, K_y) we evaluate the amplification factor $A(K_x, K_y, \alpha, \beta)$ for many phase angles α, β and record the proportion $p(K_x, K_y)$ if these pair for which $|A| \leq 1$. Then a contour plot of $p(K_x, K_y)$ in $K_x - K_y$ plane will indicate the stability region of the scheme.

The analysis shows that the ADER2 scheme with the MUSCL type reconstruction (3.25) is stable with conventional stability condition

$$K_x + K_y \leq 1, \quad a, b > 0. \tag{3.28}$$

Figs. 3.3 - 3.6 show stability contour plots of $p(K_x, K_y)$ of higher-order ADER schemes. We observe that the upwind-biased ADER3 scheme has conventional

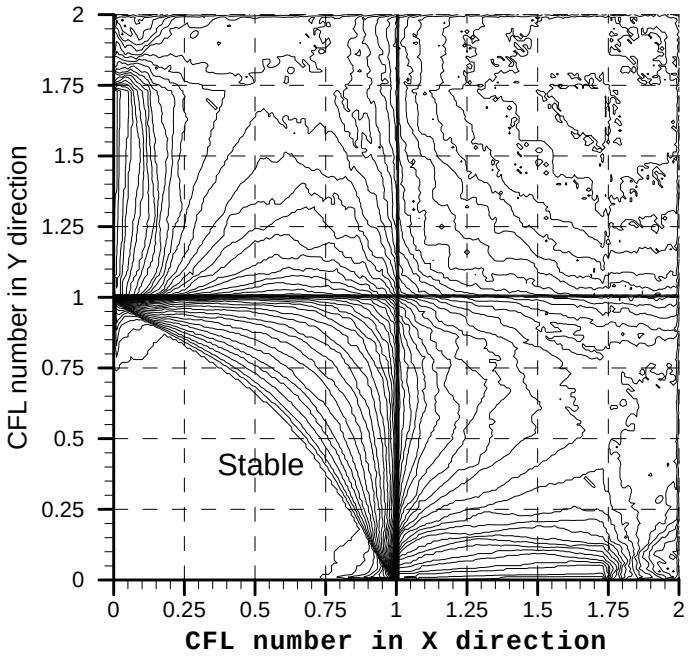

Figure 3.4. Stability plot for the two-dimensional ADER4 scheme with a centred reconstruction

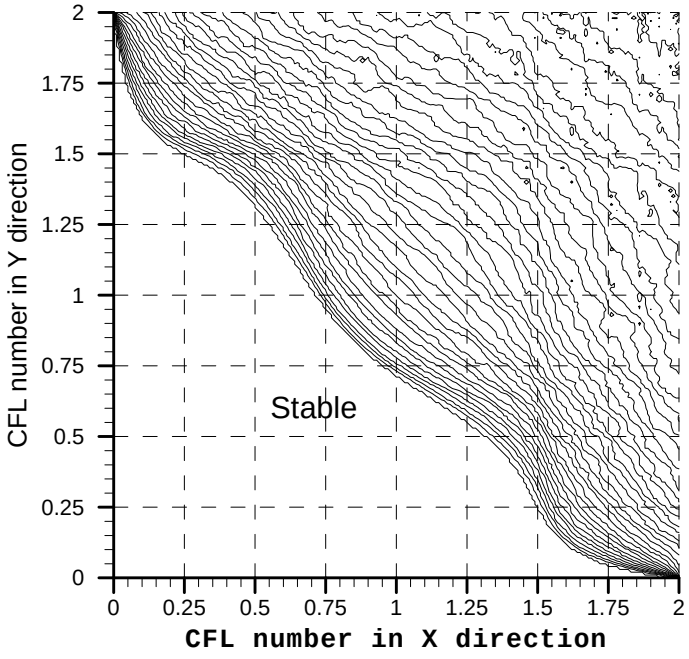

Figure 3.5. Stability plot for the two-dimensional ADER4 scheme with an upwind-biased reconstruction

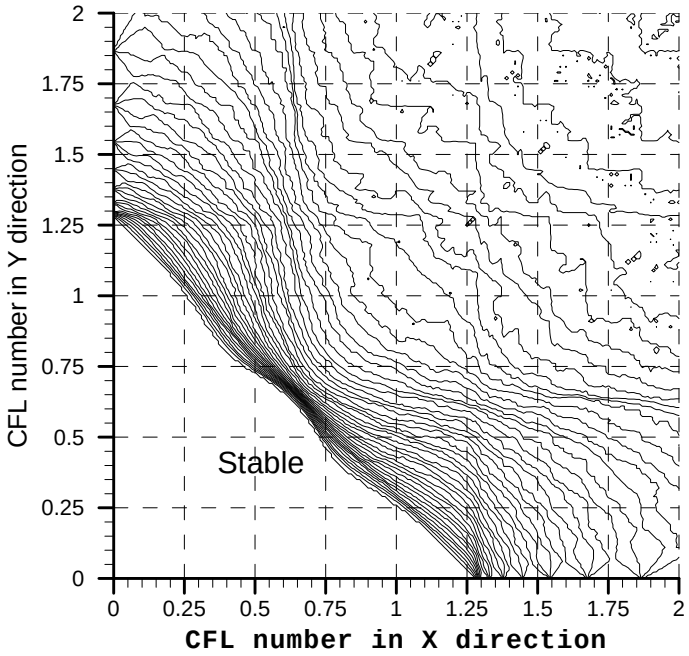

Figure 3.6. Stability plot for the two-dimensional ADER3-4 scheme with an upwind-biased reconstruction

stability condition (3.28). The stability of the fourth order scheme depends on the reconstruction used. The scheme with a centred stencil is stable under condition

$$K_x + K_y \leq 0.75, \quad a, b > 0. \tag{3.29}$$

However, the scheme with an upwind-biased stencil has a much larger stability region, approximately twice that of the ADER3 scheme. In practice, the time step for this scheme can be chosen from the approximate condition

$$K_x + K_y \leq 1.75, \quad a, b > 0. \tag{3.30}$$

The stability region of the ADER3-4 scheme with an upwind-biased stencil is an average between (3.28) and (3.30). In practice, the time step for this scheme can be chosen from the approximate condition

$$K_x + K_y \leq 1.25, \quad a, b > 0. \tag{3.31}$$

Therefore, as in the one-dimensional case, the use of a higher-order spatial reconstruction affects the stability region of the scheme.

If one of the advection coefficients of the equation is zero for all schemes we recover the one-dimensional stability region for most of the schemes except the centred ADER4.

3.2.4. Truncation error analysis

To find the truncation error of the scheme we have to insert the exact solution $v(x, y, t)$ into the difference formulation and obtain the expression for the leading term of the truncation error $\epsilon(\Delta x, \Delta y, \Delta t)$ as a function of Courant numbers K_x, K_y.

Direct evaluation of expression for the truncation error of the second-order scheme with the MUSCL reconstruction (3.25) gives the following result:

$$\begin{aligned}\epsilon &= \left(-\frac{1}{12}\,a\Delta x^2 + \frac{1}{4}a^2\Delta t\Delta x - \frac{1}{6}a^3\Delta t^2\right)\frac{\partial^3}{\partial x^3}v \\ &+ \left(\frac{1}{4}\,ab\Delta t\Delta x - \frac{1}{2}a^2b\Delta t^2\right)\frac{\partial^3}{\partial x^2\partial y}v + \left(\frac{1}{4}\,ab\Delta t\Delta y - \frac{1}{2}ab^2\Delta t^2\right)\frac{\partial^3}{\partial x\partial y^2}v \\ &+ \left(\frac{1}{4}b^2\Delta t\Delta y - \frac{1}{6}b^3\Delta t^2 - \frac{1}{12}\,b\Delta y^2\right)\frac{\partial^3}{\partial y^3}v\end{aligned}$$

Inserting expression for K_x, K_y we obtain

$$\begin{aligned}\epsilon &= a\left(-\frac{1}{12} + \frac{1}{4}K_x - \frac{1}{6}K_x^2\right)\Delta x^2\frac{\partial^3}{\partial x^3}v + b\left(\frac{1}{4}K_x - \frac{1}{2}K_x^2\right)\Delta x^2\frac{\partial^3}{\partial x^2\partial y}v \\ &+a\left(\frac{1}{4}\,aK_y - \frac{1}{2}{K_y}^2\right)\Delta y^2\frac{\partial^3}{\partial x\partial y^2}v + b\left(-\frac{1}{12} + \frac{1}{4}K_y - \frac{1}{6}b{K_y}^2\right)\Delta y^2\frac{\partial^3}{\partial y^3}v\end{aligned}$$

It is obvious that the scheme is second order accurate in space and time.

Direct evaluation of expression for the truncation error of the third order upwind-biased scheme gives the following result:

$$\begin{aligned}\epsilon &= +\left(\frac{1}{24}a^4\Delta t^3 - \frac{1}{24}a^2\Delta t\Delta x^2 + \frac{1}{12}a\Delta x^3 - \frac{1}{24}a^3\Delta t^2\Delta x\right)\frac{\partial^4}{\partial x^4}v \\ &+\left(\frac{1}{12}b\Delta y^3 - \frac{1}{24}\Delta t\Delta y^2b^2 - \frac{1}{12}b^2\Delta t^2\Delta y + \frac{1}{24}b^4\Delta t^3\right)\frac{\partial^4}{\partial y^4}v \\ &+\frac{1}{6}a^3b\Delta t^3\frac{\partial^4}{\partial x^3\partial y}v + \frac{1}{4}a^2b^2\Delta t^3\frac{\partial^4}{\partial x^2\partial y^2}v + \frac{1}{6}ab^3\Delta t^3\frac{\partial^4}{\partial x\partial y^3}v \\ &-\frac{1}{12}ab\Delta t\Delta x^2\frac{\partial^4}{\partial x^3\partial y}v - \frac{1}{12}ab\Delta t\Delta y^2\frac{\partial^4}{\partial x\partial y^3}v.\end{aligned}$$

The scheme is third order accurate in space and time. Inserting expression for K_x, K_y we obtain

$$\begin{aligned}\epsilon &= +a\left(\frac{1}{24}K_x^3 - \frac{1}{24}K_x^2 - \frac{1}{24}K_x + \frac{1}{12}\right)\Delta x^3\frac{\partial^4}{\partial x^4}v \\ &+b\left(\frac{1}{12} - \frac{1}{24}K_y - \frac{1}{12}K_y^2 + \frac{1}{24}K_y^3\right)\Delta y^3\frac{\partial^4}{\partial y^4}v \\ &+\frac{1}{6}bK_x^3\Delta x^3\frac{\partial^4}{\partial x^3\partial y}v + \frac{1}{4}bK_x^2K_y\Delta x^2\Delta y\frac{\partial^4}{\partial x^2\partial y^2}v + \frac{1}{6}aK_y^3\Delta y^3\frac{\partial^4}{\partial x\partial y^3}v \\ &-\frac{1}{12}bK_x\Delta x^3\frac{\partial^4}{\partial x^3\partial y}v - \frac{1}{12}aK_y\Delta y^3\frac{\partial^4}{\partial x\partial y^3}v.\end{aligned}$$

Note, that the presentation of ϵ as a function of K_x, K_y is not unique. In two limiting cases of one-dimensional advection the above expression coincides with the corresponding truncation error of third-order upwind-biased scheme (3.12) in purely one-dimensional case, see Table 9.

Direct evaluation of expression for the truncation error of the fourth order upwind-biased scheme gives the following result:

$$\begin{aligned}\epsilon = &+\left(\frac{1}{20}a\Delta x^4+\frac{1}{24}a^4\Delta t^3\Delta x-\frac{1}{24}a^3\Delta t^2\Delta x^2-\frac{1}{24}a^2\Delta t\Delta x^3-\frac{1}{120}a^5\Delta t^4\right)\frac{\partial^5}{\partial x^5}v\\ &+\left(\frac{1}{20}b\Delta y^4-\frac{1}{24}b^2\Delta t\Delta y^3+\frac{1}{24}b^4\Delta t^3\Delta y-\frac{1}{24}b^3\Delta t^2\Delta y^2-\frac{1}{120}b^5\Delta t^4\right)\frac{\partial^5}{\partial y^5}v\\ &-\frac{1}{12}a^2b^3\Delta t^4\frac{\partial^5}{\partial x^2\partial y^3}v-\frac{1}{24}a^4b\Delta t^4\frac{\partial^5}{\partial x^4\partial y}v-\frac{1}{12}a^3b^2\Delta t^4\frac{\partial^5}{\partial x^3\partial y^2}v\\ &-\frac{1}{24}ab^4\Delta t^4\frac{\partial^5}{\partial x\partial y^4}v+\frac{1}{48}a^3b\Delta t^3\Delta x\frac{\partial^5}{\partial x^4\partial y}v-\frac{1}{24}ab\Delta t\Delta x^3\frac{\partial^5}{\partial x^4\partial y}v+\frac{1}{48}\Delta t^3\Delta yab^3\frac{\partial^5}{\partial x\partial y^4}v\\ &+\frac{1}{72}ab^2\Delta t^2\Delta x^2\frac{\partial^5}{\partial x\partial y^4}v-\frac{1}{24}ab\Delta t\Delta y^3\frac{\partial^5}{\partial x\partial y^4}v+\frac{1}{72}a^2b\Delta t^2\Delta x^2\frac{\partial^5}{\partial x^4\partial y}v.\end{aligned}$$

The scheme is fourth order accurate in space and time. Inserting expression for K_x, K_y we obtain:

$$\begin{aligned}\epsilon = &+a\left(\frac{1}{20}+\frac{1}{24}K_x^3-\frac{1}{24}K_x^2-\frac{1}{24}K_x-\frac{1}{120}K_x^4\right)\Delta x^4\frac{\partial^5}{\partial x^5}v\\ &+b\left(\frac{1}{20}-\frac{1}{24}K_y+\frac{1}{24}K_y^3-\frac{1}{24}K_y^2-\frac{1}{120}K_y^4\right)\Delta y^4\frac{\partial^5}{\partial y^5}v\\ &-\frac{1}{12}aK_xK_y^3\Delta x\Delta y^3\frac{\partial^5}{\partial x^2\partial y^3}v-\frac{1}{24}bK_x^4\Delta x^4\frac{\partial^5}{\partial x^4\partial y}v-\frac{1}{12}bK_x^3K_y\Delta x^3\Delta y\frac{\partial^5}{\partial x^3\partial y^2}v\\ &-\frac{1}{24}aK_y^4\Delta y^4\frac{\partial^5}{\partial x\partial y^4}v+\frac{1}{48}bK_x^3\Delta x^4\frac{\partial^5}{\partial x^4\partial y}v-\frac{1}{24}bK_x\Delta x^4\frac{\partial^5}{\partial x^4\partial y}v+\frac{1}{48}aK_y^3\Delta y^4\frac{\partial^5}{\partial x\partial y^4}v\\ &+\frac{1}{72}aK_y^2\Delta x^2\Delta y^2\frac{\partial^5}{\partial x\partial y^4}v-\frac{1}{24}aK_y\Delta y^4\frac{\partial^5}{\partial x\partial y^4}v+\frac{1}{72}bK_x^2\Delta x^4\frac{\partial^5}{\partial x^4\partial y}v.\end{aligned}$$

In two limiting cases of one-dimensional advection the above expression coincides with the corresponding truncation error of fourth-order upwind-biased scheme in purely one-dimensional case, see Table 10.

3.3. Three-dimensional schemes

Finally, we consider the model three-dimensional linear advection equation

$$\frac{\partial v}{\partial t}+\frac{\partial f(v)}{\partial x}+\frac{\partial g(v)}{\partial y}+\frac{\partial h(v)}{\partial z}=0,\quad f=av,\quad g=bv,\quad h=cv, \tag{3.32}$$

where a, b and c are constant propagation speeds. The scheme is written as

$$v_{ijk}^{n+1}=v_{ijk}^n-\frac{\Delta t}{\Delta x}(f_{i+1/2,jk}-f_{i-1/2,jk})-\frac{\Delta t}{\Delta y}(g_{i,j+1/2,k}-g_{i,j-1/2,k})-\frac{\Delta t}{\Delta y}(h_{ijk+1/2}-g_{ijk-1/2}). \tag{3.33}$$

Suppose the reconstruction polynomial for the cell i, j, k is given by $P_{ijk}(x, y, z)$. Similar to the two-dimensional case, for the linear constant coefficient equation in the case $a > 0$ the solution of the DRP problem is easy. The flux $f_{i+1/2,jk}$ of order r reads:

$$f_{i+1/2,jk} = \frac{a}{\Delta y \Delta z} \int_{y_{j-1/2}}^{y_{j+1/2}} \int_{z_{k-1/2}}^{z_{k+1/2}} \Big(P_i(x_{i+1/2}, y, z) + \sum_{p=1}^{r-1} \left(-a\frac{d}{dx} - b\frac{d}{dy} - c\frac{d}{dz} \right)^p \frac{\Delta t^p}{(p+1)!} P_{ijk}(x_{i+1/2}, y, z) \Big) \, dz \, dy. \tag{3.34}$$

Performing the exact integration over the cell side, we obtain the following expression for the three-dimensional fixed-stencil ADER flux in the x coordinate direction:

$$f_{i+1/2,jk} = a \sum_{\alpha} \sum_{\beta} \sum_{\gamma} W_{\alpha,\beta,\gamma} \, v_{i+\alpha,j+\beta,k+\gamma}, \tag{3.35}$$

where $W_{\alpha,\beta}$ are the coefficients which depend on the CFL coefficients K_x, K_y and $K_z = c\Delta t/\Delta z$.

The fluxes in other directions are formulated in an entirely analogous way.

3.3.1. Description of the schemes

Second-order scheme

We study the second order ADER scheme with MUSCL-type piece-wise linear reconstruction [26] with the reconstruction polynomial given by:

$$P_{ijk}(x, y, z) = v_{ijk} + S_x(x - x_i) + S_y(y - y_j) + S_z(z - z_k), \tag{3.36}$$

where S_x, S_y, S_z are slopes in the x, y and z coordinate directions correspondingly. Similar to the two-dimensional case, we choose the centred slopes:

$$S_x = \frac{v_{i+1,jk} - v_{i-1,jk}}{2\Delta x}, \quad S_y = \frac{v_{ij+1,k} - v_{ij-1,k}}{2\Delta y}, \quad S_z = \frac{v_{ijk+1} - v_{ijk-1}}{2\Delta z}.$$

The corresponding ADER flux is given by

$$W_{-1,0,0} = -\frac{1}{4} + \frac{1}{4}K_x, \quad W_{0,-1,0} = \frac{1}{4}K_y, \quad W_{0,0,-1} = \frac{1}{4}K_z, \quad W_{0,0,0} = 1,$$

$$W_{0,0,1} = -\frac{1}{4}K_z, \quad W_{0,1,0} = -\frac{1}{4}K_y, \quad W_{1,0,0} = \frac{1}{4} - \frac{1}{4}K_x.$$

Third-order schemes

We limit our study to the upwind-biased third order ADER scheme. The corresponding parabolic reconstruction polynomial for $f_{i+1/2,jk}$ uses the following two-dimensional stencil of 27 cells: $(i-1,i,i+1)\times(j-1,j,j+1)\times(k-1,k,k+1)$. The flux is given by

$$W_{-1,-1,-1,} = -\frac{1}{72}K_yK_z, \quad W_{-1,-1,0} = -\frac{1}{72}K_y\left(2K_y+3\right), \quad W_{-1,-1,1} = \frac{1}{72}K_yK_z,$$

$$W_{-1,0,-1} = -\frac{1}{72}K_z\left(3+2K_z\right), \quad W_{-1,0,0} = \frac{1}{18}\left(K_y^2+K_z^2+3K_x^2-3\right),$$

$$W_{-1,0,1} = -\frac{1}{72}K_z\left(-3+2K_z\right), \quad W_{-1,1,-1} = \frac{1}{72}K_yK_z,$$

$$W_{-1,1,0} = -\frac{1}{72}K_y\left(-3+2K_y\right), \quad W_{-1,1,1} = -\frac{1}{72}K_yK_z,$$

$$W_{0,-1,-1} = \frac{5}{72}K_yK_z, \quad W_{0,-1,0} = \frac{1}{72}K_y\ \left(10K_y+15+12K_x\right),$$

$$W_{0,-1,1} = -\frac{5}{72}K_yK_z, \quad W_{0,0,-1} = \frac{1}{72}\ Kz\ \left(10\ Kz+15+12\ Kx\right),$$

$$W_{0,0,0} = \frac{1}{18}\left(15-5K_y^2-5K_z^2-6K_x^2\right)+\frac{1}{2}K_x, \quad W_{0,0,1} = -\frac{1}{72}K_z\left(-10K_z+15+12K_x\right),$$

$$W_{0,1,-1} = -\frac{5}{72}K_yK_z, \quad W_{0,1,0} = \frac{1}{72}K_y\left(10K_y-15-12K_x\right),$$

$$W_{0,1,1} = \frac{5}{72}K_yK_z, \quad W_{1,-1,-1} = \frac{1}{36}K_yK_z,$$

$$W_{1,-1,0} = \frac{1}{36}K_y\left(2K_y+3-6K_x\right), \quad W_{1,-1,1} = -\frac{1}{36}K_yK_z,$$

$$W_{1,0,-1} = -\frac{1}{36}K_z\ \left(-2K_z-3+6K_x\right), \quad W_{1,0,0} = -\frac{1}{9}K_y^2-\frac{1}{9}K_z^2+\frac{1}{3}-\frac{1}{2}K_x+\frac{1}{6}K_x^2,$$

$$W_{1,0,1} = \frac{1}{36}K_z\left(2K_z-3+6K_x\right), \quad W_{1,1,-1} = -\frac{1}{36}K_yK_z,$$

$$W_{1,1,0} = \frac{1}{36}K_y\left(2K_y-3+6K_x\right), \quad W_{1,1,1} = \frac{1}{36}K_yK_z.$$

3.3.2. Stability analysis

For the von Neumann stability analysis we consider a *trial solution*

$$v_{ijk}^n = A^n\exp\left(I(i\alpha+j\beta+k\gamma),\right.$$

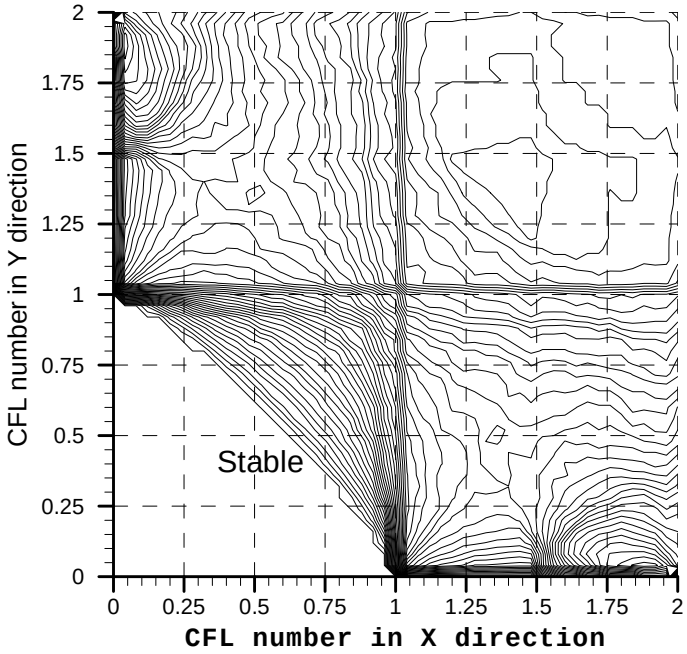

Figure 3.7. Stability plot for the three-dimensional ADER schemes for $K_z = 0$.

where A is the amplitude, α,β and γ are phase angles in x, y and z directions. We now write down the scheme in the following concise form:

$$v_{ijk}^{n+1} = \sum_{lmp} b_{lmp} v_{i+l,j+m,k+p}^{n}, \tag{3.37}$$

where b_{lmp} are the coefficients. Inserting the trial solution in the expression above we obtain the following algebraic expression for the square of the module of A is given by

$$|A|^2 = \left(\sum_{lm} b_{lmp} \cos\left(l\alpha + m\beta + p\gamma\right) \right)^2 + \left(\sum_{lmp} b_{lmp} \sin\left(l\alpha + m\beta + p\gamma\right) \right)^2 . \tag{3.38}$$

A necessary condition for stability is $|A| \leq 1$. For a given set (K_x, K_y, K_z) we evaluate the amplification factor for many phase angles and record the proportion $p(K_x, K_y, K_y)$ of sets for which $|A| \leq 1$. Then a contour plot of $p(K_x, K_y, K_z)$ in $K_x - K_y$ plane for a given value of K_z will indicate the stability region of the scheme.

Our analysis shows that the stability regions of ADER2 and ADER3 schemes are identical and are given in Figs. 3.7 - 3.8. We observe that the schemes are stable under the conventional stability condition of the 3D unsplit Godunov scheme:

$$K_x + K_y + K_z \leq 1, \quad a, b, c > 0. \tag{3.39}$$

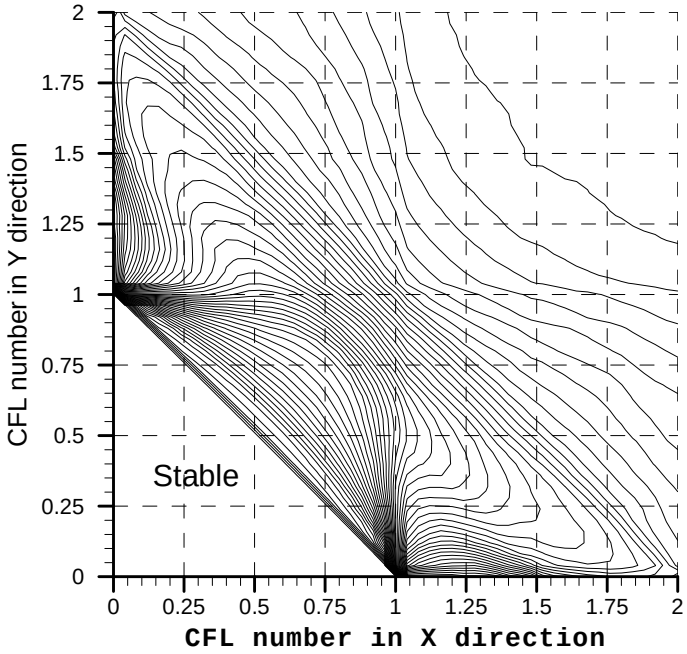

Figure 3.8. Stability plot for the three-dimensional ADER schemes for $K_z = 1 - K_x - K_y$.

3.3.3. Truncation error analysis

Direct evaluation of the leading term of the truncation error $\epsilon(\Delta x, \Delta y, \Delta t)$ as a function of K_x, K_y and K_z shows that both ADER2 and ADER3 schemes achieve the r^{th} order of accuracy in space and time. The corresponding expressions are omitted. For the ADER3 scheme in two limiting cases of one-dimensional advection the truncation error coincides with the corresponding truncation error of third-order upwind-biased scheme (3.12) in the purely one-dimensional case, see Table 9.

Conclusions

In this chapter we have analyzed stability properties and truncation errors of ADER schemes. The analysis can be divided in three parts: one-dimensional linear and non-linear schemes, two-dimensional linear and three-dimensional linear schemes. In the first part we have studied the linear schemes with conventional single-polynomial reconstruction, linear schemes with increased spatial order of accuracy as well as linear and nonlinear schemes with weighted reconstruction. The analysis shows that the properties of the schemes depend strongly on the choice of the reconstruction stencil. Overall, one-dimensional schemes with weighted

reconstructions are most accurate but have a reduced linear stability region. However, in practical calculations the nonlinear versions are stable under normal Courant numbers for both smooth and discontinuous solutions. We also note some unusual stability regions for the fourth order schemes, e.g. the scheme with the centred reconstruction is stable for Courant numbers up to two. In general, we find that the stability regions of schemes of even and odd orders of accuracy are quite different.

In two spatial dimensions we have analyzed second, third and fourth order schemes with different reconstructions. Due to an increased complexity of these schemes we have limited ourselves to some selected reconstructions only. Overall, we observe that the designed schemes have a conventional or better stability regions. Truncation error is such that for special cases of advection in one dimension only it coincides in most of the cases with that of the corresponding one-dimensional scheme. In three spatial dimensions our analysis is limited to the second and third order schemes which are shown to be stable with a conventional stability region. The truncation error of the third-order scheme reduces to the one-dimensional one when advection takes place in one spacial dimension only.

4. *Numerical results*

Introduction

In this chapter we present numerical results of the ADER schemes of up to fifth order of accuracy as applied to linear and nonlinear conservation laws with source terms. Different fluxes are used as the building blocks. For comparisons we also run the finite-volume versions of the WENO schemes [22, 3, 41] with the third-order TVD Runge-Kutta method for time evolution. Following the original reference [41], in two space dimensions for nonlinear systems we use the dimension-by-dimension reconstruction, upwind Rusanov flux [38] as the building block and a three-point (*sixth order*) Gaussian quadrature to discretize fluxes and thus is of formal fifth order of accuracy in space.

All results are obtained using the fully nonlinear versions of the schemes, even when verifying the convergence order for the infinitely smooth solutions.

We remark that it seems to have become a popular practice to check the formal order of very high-order schemes by running them with very small Courant numbers or choosing the time step in such a way that the spatial order dominates the computation [3, 11]. This results in exceedingly small time steps and therefore *enormous* computational cost of the scheme. This is especially so in many space dimensions. We remark that in practical calculations for hyperbolic equations one uses a *fixed* Courant number which should be as close as possible to the maximum allowed value given in the previous section. This would maximize the efficiency of the methods. Since here our goal is to compare the performance of different methods in a realistic setup, in all computations below we use a fixed Courant number close to the upper stability limit of the scheme.

4.1. Scalar equations

4.1.1. Long time evolution for linear advection

The motivation here is to test the ADER-WAF schemes for problems with discontinuous solutions for long evolution times. We solve

$$\partial_t q + \lambda \partial_x q = 0 \ , \quad \lambda = 1 \ , \tag{4.1}$$

with the following initial condition [22, 46, 3]

$$q(x,0) = \begin{cases} \exp\left(\ln 2\ , (x+0.7)^2/0.0009\right)\ , & -0.8 \leq x \leq -0.6\ , \\ 1\ , & -0.4 \leq x \leq -0.2\ , \\ 1 - |10x - 1|\ , & 0.0 \leq x \leq 0.2\ , \\ (1 - 100(x-0.5)^2)^{1/2}\ , & 0.4 \leq x \leq 0.6\ , \\ 0\ , & \text{otherwise}\ . \end{cases} \tag{4.2}$$

This initial condition consists of a discontinuous square pulse and several continuous but narrow profiles. We use a baseline mesh of 200 cells and periodic boundary conditions. We compute the numerical solution at the output times $t = 20$ and $t = 2000$. Note that for the last output time the initial profile is propagated 1000 times over the spatial domain. When CFL number of unity is used, this output time corresponds to $1000 \times N$ time steps, where N is the number of cells. For example, for the finest mesh of $N = 1600$ cells the numerical solution is evolved for 1.6×10^6 time steps.

Table 11 shows results of our convergence study at two output times: $t = 20$ (10 periods) and $t = 2000$ (1000 periods). We present the errors of *cell averages* of the solution in the L_1 norm; in this norm all schemes should converge with first order accuracy. We use $CFL = 0.95$ for ADER-WAF schemes and, following the original papers [22, 3], $CFL = 0.4$ for the WENO5 scheme. From the results of Table 11, the most accurate schemes are the ADER-WAF schemes, which is apparently due to the excellent resolution of the square pulse. On the finest mesh of 1600 cells and the largest output time $t = 2000$ ADER3-WAF is more accurate than the WENO5 scheme by a factor of twenty.

With regards to the behaviour of the ADER schemes, as we increase both the space and the time accuracy, the results show that the ADER4-WAF scheme is in turn more accurate than the ADER3-WAF scheme by a factor of two on all meshes. We also note that the convergence rates of the ADER3-WAF and ADER4-WAF schemes actually exceed the theoretically expected rate of one (for cell averages).

It is important to remember, at this stage, that although for discontinuous solutions most shock-capturing schemes are expected to achieve first order accuracy in the integral L_1 norm, the actual order of accuracy can be much lower than the theoretical first order. An illuminating illustration of this fact can be found in the convergence table for the blast interaction test problem in [83]. Another important factor is the actual size of the error on a given (coarse) mesh; this becomes even more important for very long output times. From Table 11 we see that not only the

Table 11 . Convergence study for various schemes as applied to the model equation (4.1) with initial condition (4.2) at output times $t = 20$ and $t = 2000$. ADER and ADER-WAF schemes used with $CFL = 0.95$ and WENO5 scheme used with $CFL = 0.4$

Scheme	N	$t = 20$		$t = 2000$	
		L_1	r_1	L_1	r_1
WENO5	200	1.05×10^{-1}		4.07×10^{-1}	
	400	4.55×10^{-2}	1.21	3.98×10^{-1}	0.03
	800	2.13×10^{-2}	1.09	3.26×10^{-1}	0.29
	1600	1.16×10^{-2}	0.88	1.65×10^{-1}	0.98
ADER3-WAF	200	2.70×10^{-2}		1.54×10^{-1}	
	400	1.06×10^{-2}	1.35	5.95×10^{-2}	1.37
	800	4.52×10^{-3}	1.22	2.46×10^{-2}	1.27
	1600	2.09×10^{-3}	1.11	8.92×10^{-3}	1.46
ADER4-WAF	200	2.30×10^{-2}		7.00×10^{-2}	
	400	9.55×10^{-3}	1.27	2.95×10^{-2}	1.24
	800	4.38×10^{-3}	1.12	1.11×10^{-2}	1.42
	1600	2.07×10^{-3}	1.08	4.54×10^{-3}	1.29

ADER-WAF schemes achieve the expected first order of accuracy but actually well exceed it. This is not the case with the WENO5 scheme, which approaches the first order convergence rate only on the finest mesh. Due to the faster convergence of ADER-WAF schemes with mesh refinement they produce smaller errors as compared to the WENO5 scheme.

A further illustration of the above results can be obtained by analysing Figs. 4.1 and 4.2. Fig. 4.1 shows results of the WENO5, ADER3-WAF and ADER4-WAF schemes for the output time $t = 2000$ on the mesh of 200 cells. In all figures the continuous line corresponds to the exact solution and symbols correspond to the numerical solution. Fig. 4.2 shows the corresponding results for the mesh of 1600 cells. An obvious general comment is that *long evolution times* really expose the limitations of numerical methods, even the very sophisticated schemes presented here.

WENO5, CFL=0.4

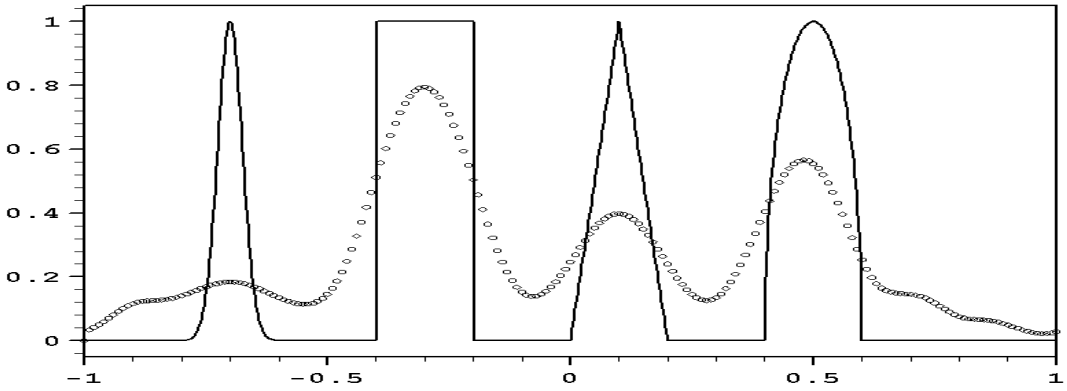

ADER3-WAF, CFL=0.95

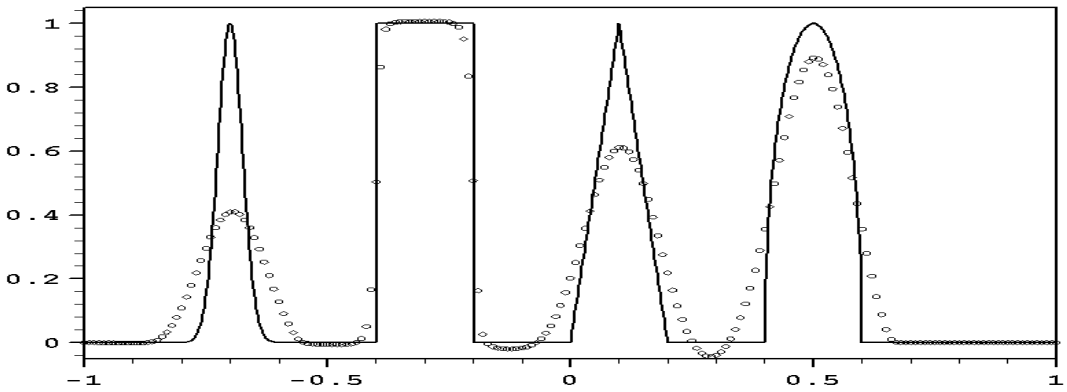

ADER4-WAF, CFL=0.95

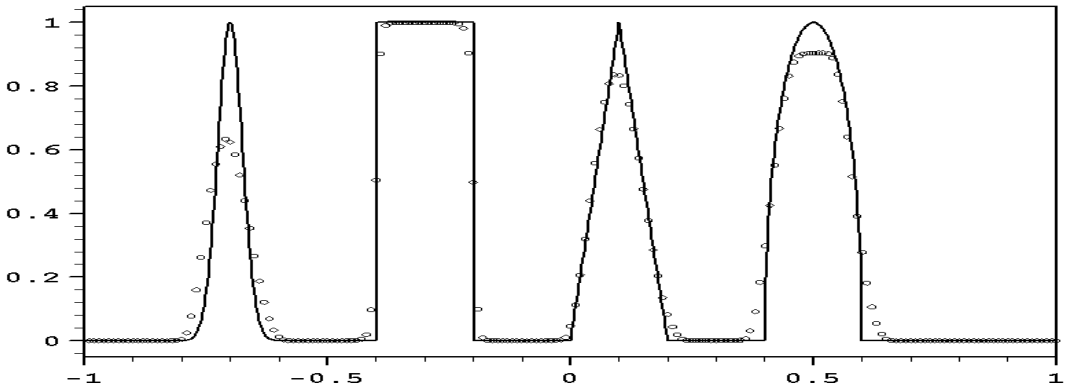

Figure 4.1. Computed (symbol) and exact (line) solutions for the linear advection equation (4.1) with initial condition (4.2) at output time $t = 2000$. The mesh of N=200 cells is used.

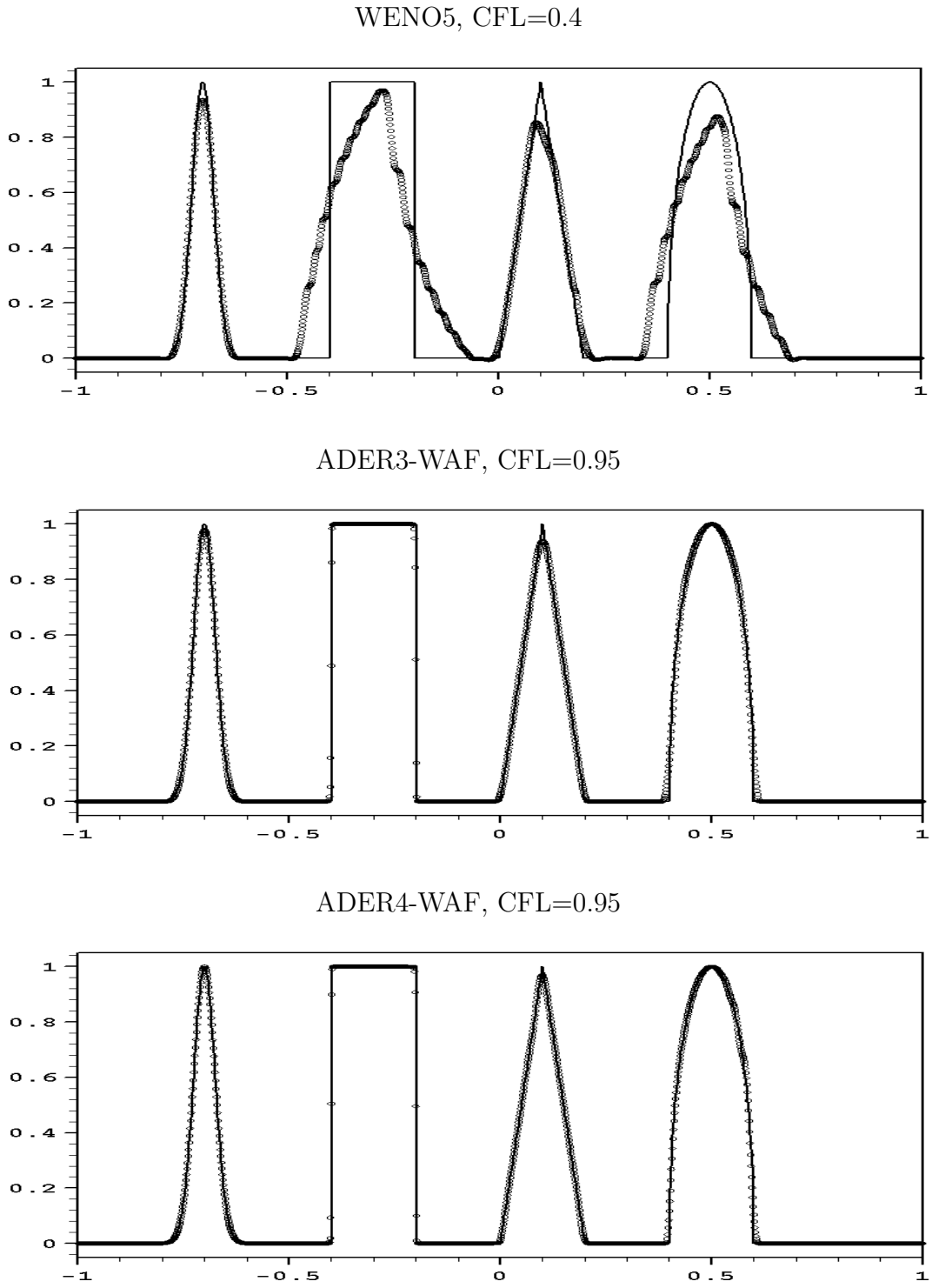

Figure 4.2. Computed (symbol) and exact (line) solutions for the linear advection equation (4.1) with initial condition (4.2) at output time $t = 2000$. The mesh of N=1600 cells is used.

We first comment on schemes of the same formal accuracy and observe that the ADER-WAF scheme is far superior to the WENO5 scheme, at least for this output time, see Fig. 4.1; this is particularly evident with regard to the resolution of the square pulse. The ADER-WAF schemes do not smear this feature, as time evolves. We would like to stress that each discontinuity has five cells across it for *all output times*, that is, once the initial smearing of the discontinuity has been established it is propagated as a steady profile with a constant number of cells across it.

We note that on the finest mesh of 1600 cells the ADER-WAF schemes have essentially converged to the exact solution, see Fig. 4.2, whereas the result of the WENO5 scheme (third-order in time) is still far from the exact solution. Third and fourth order ADER-WAF schemes combine the excellent resolution of contact discontinuities, typical of the WAF scheme with the SUPERBEE limiter, and higher order of accuracy in smooth regions, without the typical *squaring* effect of TVD schemes with compressive limiters. We also observe improvements in accuracy in the other parts of the solution when we move from the third to the fourth order scheme.

The results of the conventional ADER schemes and ADER-WAF schemes of accuracy higher than five (omitted) are somehow less satisfactory than those of the presented schemes. In particular, the ADER5-WAF and ADER6-WAF schemes do smear the square pulse, for longer times. This is again expected since the higher order terms in the flux expansion interfere with the second-order TVD flux. Another issue is the use of WENO reconstruction in the context of the ADER schemes, which might need further investigations. This particularly concerns the design of the nonlinear WENO weights.

4.1.2. Linear Reactive Equation

We solve the following advection-reaction equation

$$q_t + q_x = 5q \tag{4.3}$$

with the initial condition

$$q(x,0) = (\sin \pi x)^4, \tag{4.4}$$

defined on $[-1,1]$. The exact solution is a very fast growing function and given by

$$q(x,t) = (\sin \pi (x-t))^4 \exp(5t)$$

Table 12 shows errors of cell averages of the solution at $t = 2$. We observe that all ADER schemes operate at the designed order of accuracy. The fifth order scheme is the most accurate scheme on all meshes.

Table 12 . Reactive linear advection equation (4.3). Output time $t = 2$.

Method	Number of cells	L_∞ error	L_∞ order	L_1 error	L_1 order
ADER3	10	1.44×10^5		1.54×10^5	
	20	3.10×10^4	2.22	3.19×10^4	2.22
	40	5.25×10^3	2.56	5.17×10^3	2.63
	80	7.61×10^2	2.79	9.14×10^2	2.87
	160	1.01×10^2	2.91	1.20×10^2	2.93
ADER4	10	3.77×10^4		3.99×10^4	
	20	3.43×10^3	3.46	3.72×10^3	3.42
	40	3.85×10^2	3.15	4.48×10^2	3.05
	80	2.89×10^1	3.74	3.18×10^1	3.82
	160	1.96×10^{-1}	3.88	2.14×10^{-1}	3.89
ADER5	10	1.08×10^4		1.23×10^4	
	20	5.57×10^2	4.28	6.73×10^2	4.19
	40	2.25×10^1	4.63	2.77×10^1	4.61
	80	7.93×10^{-2}	4.83	9.78×10^{-2}	4.82
	160	2.63×10^{-3}	4.91	3.23×10^{-3}	4.92

4.1.3. The two-dimensional inviscid Burgers' equation with a source term

We solve the two-dimensional inviscid Burgers' equation with a time-dependent source term

$$q_t + \left(\frac{1}{2}q^2\right)_x + \left(\frac{1}{2}q^2\right)_y = S(x, y, t, q), \tag{4.5}$$

$$S(x, y, t, q) = \pi(q-1)\big[\cos\pi(x-t)\sin\pi(y-t) + \sin\pi(x-t)\cos\pi(y-t)\big]$$

with the following initial condition defined on $[-1, 1] \times [-1, 1]$:

$$q(x, y, 0) = q_0(x, y) = \sin(\pi x)\sin(\pi y) \tag{4.6}$$

and periodic boundary conditions. The exact solution is $q(x, y, t) = q_0(x - t, y - t)$. The cell averages of the exact solution at the output time are computed by 8^{th}-order Gaussian rule and are used to measure the numerical errors of the schemes.

Table 13 . Convergence study for the 2D inviscid Burgers' equation with a source term (4.5) with initial condition (4.6) at output time $t = 1$. CFL= 0.45 for all schemes. N is the number of cells in each coordinate direction.

Method	N	L_∞ error	L_∞ order	L_1 error	L_1 order
ADER3	10	1.90×10^{-2}		3.21×10^{-2}	
	20	2.60×10^{-3}	2.87	3.99×10^{-3}	3.01
	40	3.43×10^{-4}	2.92	4.78×10^{-4}	3.06
	80	4.15×10^{-5}	3.05	5.90×10^{-5}	3.02
	160	5.11×10^{-6}	3.02	7.36×10^{-6}	3.00
ADER4	10	7.00×10^{-3}		3.51×10^{-3}	
	20	1.82×10^{-4}	5.26	6.62×10^{-5}	5.73
	40	5.53×10^{-6}	5.04	2.00×10^{-6}	5.05
	80	1.62×10^{-7}	5.10	9.40×10^{-8}	4.41
	160	7.59×10^{-9}	4.41	5.60×10^{-9}	4.07
ADER5	10	5.46×10^{-4}		4.66×10^{-4}	
	20	2.41×10^{-5}	4.50	2.69×10^{-5}	4.11
	40	8.86×10^{-7}	4.77	8.96×10^{-7}	4.91
	80	2.88×10^{-8}	4.95	2.81×10^{-8}	5.00
	160	9.08×10^{-10}	4.99	8.77×10^{-10}	5.00

Table 14 shows the errors at the output time $t = 1$. We observe that all ADER schemes reach the design r^{th} order of accuracy in both L_∞ and L_1 norms. Moreover, the error decreases by an order of magnitude when the formal order of accuracy increases. As expected, the fifth order ADER scheme is the most accurate scheme.

The solution of this problem varies rapidly with time and thus preserving the time accuracy of the numerical schemes is essential for obtaining the desired order of accuracy.

We would like to stress the fact that the shown high orders of accuracy of ADER schemes are achieved for a *fixed* Courant number.

Table 14 . Convergence study for the 3D inviscid Burgers' equation (4.7) with initial condition (4.8) at output time $t = 0.05$. CFL= 0.27 for all schemes. N is the number of cells in each coordinate direction.

Method	N	L_∞ error	L_∞ order	L_1 error	L_1 order
ADER3	10	2.05×10^{-3}	3.17	3.47×10^{-3}	3.27
	20	3.89×10^{-4}	2.39	2.09×10^{-4}	4.05
	40	4.85×10^{-5}	3.00	1.74×10^{-5}	3.59
	80	6.99×10^{-6}	2.79	2.18×10^{-6}	3.00
ADER4	10	1.07×10^{-3}	4.14	5.82×10^{-4}	5.25
	20	6.64×10^{-5}	4.01	2.25×10^{-5}	4.70
	40	5.10×10^{-6}	3.70	1.27×10^{-6}	4.15
	80	3.07×10^{-7}	4.05	8.27×10^{-8}	3.94
ADER5	10	2.42×10^{-4}	4.30	1.17×10^{-4}	6.09
	20	1.07×10^{-5}	4.50	3.50×10^{-6}	5.06
	40	2.75×10^{-7}	5.28	1.06×10^{-7}	5.04
	80	8.79×10^{-9}	4.97	3.95×10^{-9}	4.75
WENO [41],	10	1.86×10^{-3}	3.53	1.19×10^{-3}	4.50
Rusanov flux	20	2.65×10^{-4}	2.81	9.05×10^{-5}	3.71
	40	3.64×10^{-5}	2.86	1.09×10^{-5}	3.06

4.1.4. The three-dimensional inviscid Burgers' equation

We solve the three-dimensional inviscid Burgers' equation

$$q_t + \left(\frac{1}{2}q^2\right)_x + \left(\frac{1}{2}q^2\right)_y + \left(\frac{1}{2}q^2\right)_z = 0 \tag{4.7}$$

with the following initial condition defined on $[-1,1] \times [-1,1] \times [-1,1]$:

$$q(x,y,z,0) = q_0(x,y,z) = 0.25 + \sin(\pi x)\sin(\pi y)\sin(\pi z) \tag{4.8}$$

and periodic boundary conditions. For this test problem the exact solution is obtained by solving numerically the relation $q = q_0(x - qt, y - qt, z - qt)$ for a

given point (x, y, z) and time t. The cell averages of the exact solution at the output time are computed using the 8^{th}-order Gaussian rule.

Table 14 shows the errors at the output time $t = 0.05$, when the solution is still smooth. We observe that all ADER schemes reach the design r^{th} order of accuracy in both norms. Moreover, the error decreases by an order of magnitude when the formal order of accuracy increases. As expected, the fifth order scheme is the most accurate scheme. Again, we would like to stress the fact that such high orders of accuracy are achieved for a *fixed* Courant number.

4.1.5. The kinematic frontogenesis problem

This problem [13] is a popular test in meteorology, where it models a real effect taking place in the Earth atmosphere. From the numerical point of view it tests the ability of the schemes to handle sharp moving fronts in two space dimensions. We remark that a number of advection schemes has been reported to fail for this test problem, especially those using dimensional splitting.

We solve the two-dimensional linear equation with variable coefficients

$$q_t + (u(x,y)q)_x + (v(x,y)q)_y = 0, \tag{4.9}$$

where (u, v) is a steady divergence-free velocity field:

$$\begin{gathered} u = -y\,\omega(r), \quad v = x\,\omega(r), \quad \omega(r) = \frac{1}{r}\,U_T(r), \quad r^2 = x^2 + y^2, \\ U_T(r) = U_{max}\,\mathrm{sech}^2(r)\tanh(r), \quad U_{max} = 2.5980762. \end{gathered} \tag{4.10}$$

The initial distribution of $q(x, y, t)$, defined on a square domain $[-5, 5] \times [-5, 5]$, is assumed to be one-dimensional

$$q(x, y, 0) = q_0(y) = \tanh\left(\frac{y}{\delta}\right), \tag{4.11}$$

where δ expresses the characteristic width of the front zone. The exact solution is then given by [13]

$$q(x, y, t) = q_0(y\cos(\omega t) - x\sin(\omega t)) \tag{4.12}$$

and represents the rotation of the initial distribution around the origin with variable angular velocity $\omega(r)$. We note that as time evolves the solution will eventually develop scales which will be beyond the resolution of the computational mesh.

For this test problem we also include the results of the state-of-art finite-volume WENO scheme We note that we use the exact Riemann solver as the building block

Table 15 . Convergence study for the 2D linear advection equation with variable coefficients (4.9) with initial condition (4.11) and $\delta = 1$ at output time $t = 4$. CFL= 0.45 for all schemes. N is the number of cells in each coordinate direction.

Method	N	L_∞ error	L_∞ order	L_1 error	L_1 order
ADER3	50	2.92×10^{-1}		6.53×10^{-1}	
	100	7.56×10^{-2}	1.95	1.16×10^{-1}	2.49
	200	9.27×10^{-3}	3.03	1.12×10^{-2}	3.38
	400	7.47×10^{-4}	3.63	6.65×10^{-4}	4.07
ADER4	50	2.04×10^{-1}		3.67×10^{-1}	
	100	2.95×10^{-2}	2.79	3.95×10^{-2}	3.22
	200	2.63×10^{-3}	3.49	2.51×10^{-3}	3.98
	400	3.22×10^{-5}	6.35	2.57×10^{-5}	6.61
ADER5	50	1.36×10^{-1}		2.84×10^{-1}	
	100	2.10×10^{-2}	2.69	3.06×10^{-2}	3.21
	200	1.26×10^{-3}	4.06	9.47×10^{-4}	5.01
	400	2.08×10^{-5}	5.92	1.70×10^{-5}	5.80
WENO [41]	50	2.87×10^{-1}		6.80×10^{-1}	
exact Riemann solver	100	7.78×10^{-2}	1.88	1.23×10^{-1}	2.47
	200	9.82×10^{-3}	2.99	1.44×10^{-2}	3.10
	400	1.02×10^{-3}	3.27	1.86×10^{-3}	2.95

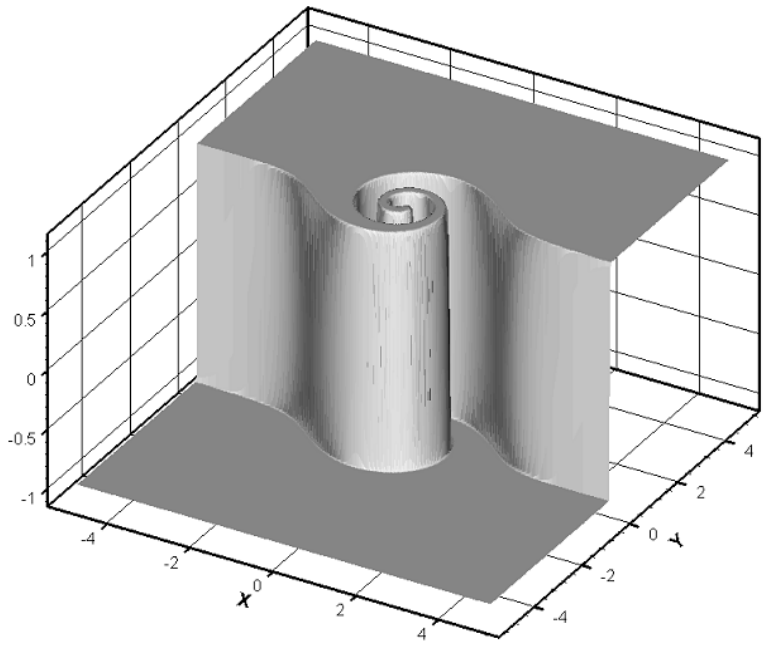

Figure 4.3. Solution of (4.9) with the initial condition (4.11) and $\delta = 10^{-6}$. Method: the ADER5 scheme. Mesh of 401×401 cells is used.

for the WENO scheme whereas in the original reference [41] a more diffusive Rusanov flux [38] is used.

We first consider a smooth solution with $\delta = 1$. Table 15 shows a convergence study for cell averages at the output time $t = 4$. Obviously, all ADER schemes achieve the designed order of accuracy. The size of the error decreases as the formal order of the scheme increases. Moreover, the forth and fifth order schemes show sixth order of accuracy on fine meshes. We see that the third-order ADER3 scheme competes well with the WENO scheme and higher-order ADER schemes are considerably more accurate than the WENO scheme due to their higher order spatial and temporal accuracy.

Next we compute the numerical solution which corresponds to a discontinuous initial distribution, with $\delta = 10^{-6}$. At the given output time the initial discontinuity has been rotated several times and the solution represents a discontinuous rolling surface. Such a profile is difficult to be resolved on a fixed mesh since the scheme must be able to handle moving discontinuities.

Figs. 4.3 – 4.4 depict, respectively, a three-dimensional plot and contour plot of the numerical solution obtained by the fifth order ADER scheme. We observe that the numerical solution is essentially non-oscillatory with sharp resolution of all discontinuities. All parts of the discontinuous rolling surface have been captured

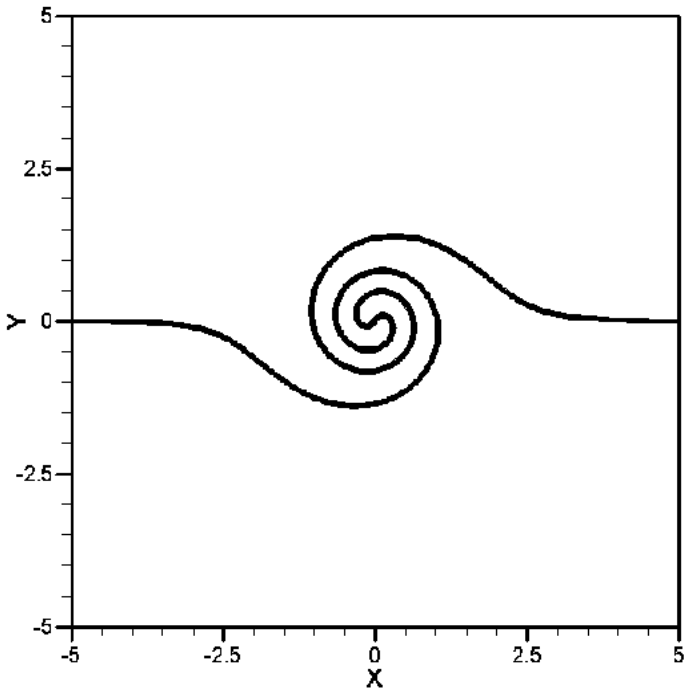

Figure 4.4. Contours of the solution of (4.9) with the initial condition (4.11) and $\delta = 10^{-6}$. Method: the ADER5 scheme. Mesh of 401×401 cells is used. See also Fig. 4.3.

well. Further illustration is provided by Figures 4.5 – 4.7, which show one-dimensional cuts along the y axis for $-3 \leq y \leq 3$; results of the third, forth and fifth order schemes on the meshes of 201×201 cells and 401×401 cells are shown. The odd number of cells is chosen so that the one-dimensional cut corresponds to the center of a middle cell for both meshes. In all figures the solid line corresponds to point-wise values of the exact solution, whereas symbols correspond to the numerical solution (cell averages). The meshes of 201×201 cells (left plot) and 401×401 cells (right plot) are used. Clearly all schemes capture all features correctly. Note also that the resolution of the discontinuities improves as the formal order of accuracy of the scheme increases, which is more clearly shown in the finer mesh results. We observe slight oscillations in the result of the ADER5 scheme in the y cut of $q(x, y, t)$. These oscillations are due to the fact that the essentially non-oscillatory reconstruction cannot find a smooth stencil on this coarse mesh of 201×201 cells. Indeed, there are only four cells between discontinuities in the middle, whereas the forth order polynomials used in the reconstruction need at least five cells. When the mesh is refined further the oscillations vanish rapidly.

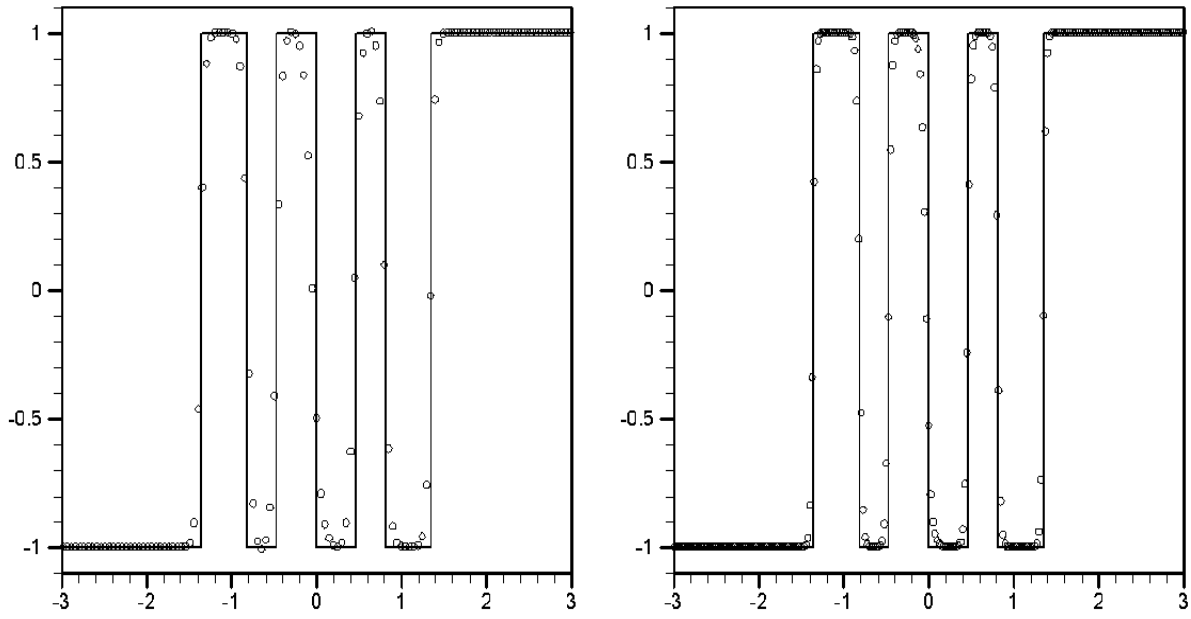

Figure 4.5. One-dimensional cuts along the y axis for (4.9) with the initial condition (4.11) and $\delta = 10^{-6}$ for the ADER3 scheme.

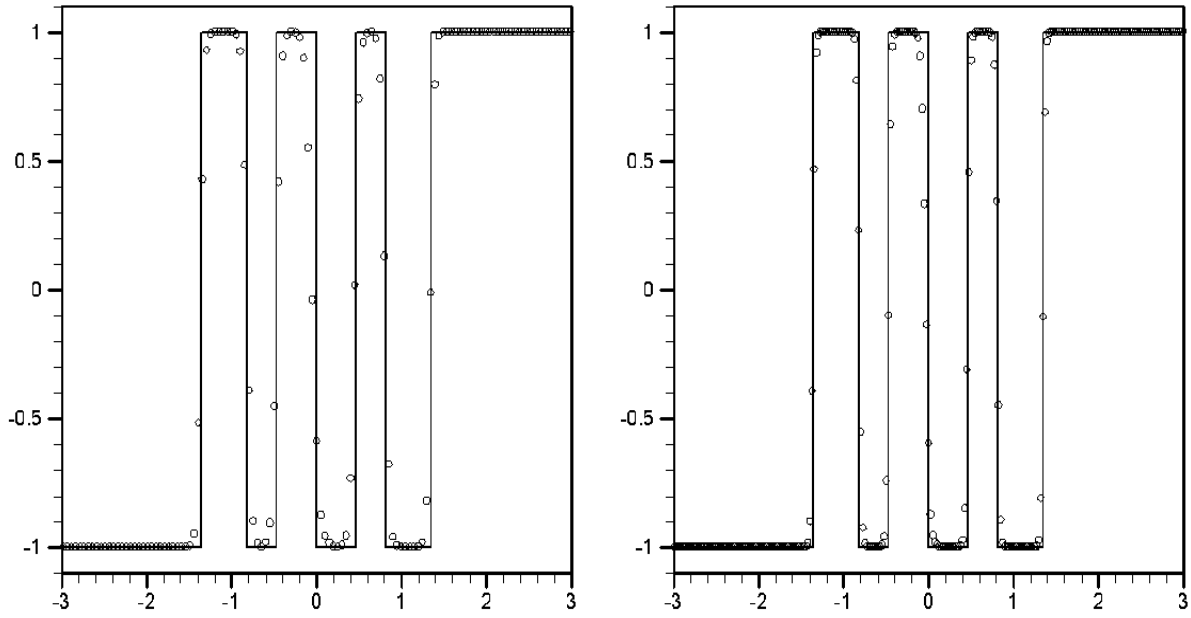

Figure 4.6. One-dimensional cuts along the y axis for (4.9) with the initial condition (4.11) and $\delta = 10^{-6}$ by the ADER4 scheme.

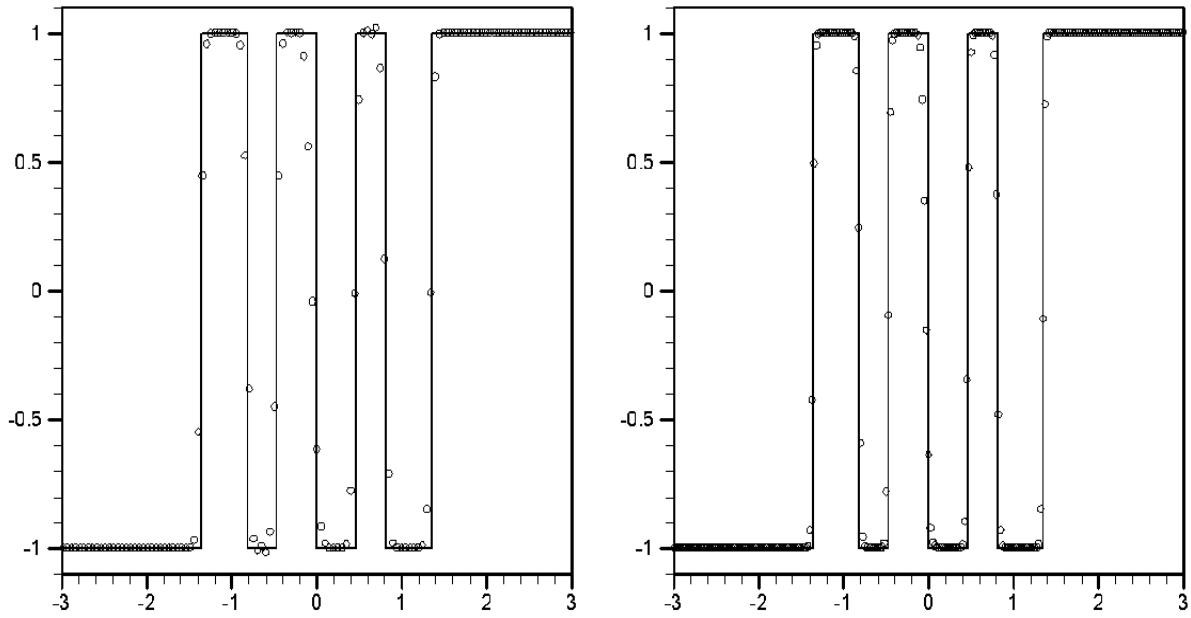

Figure 4.7. One-dimensional cut along the y axis for (4.9) with the initial condition (4.11) and $\delta = 10^{-6}$ by the ADER5 scheme.

4.2. Application to nonlinear systems

Next we present numerical results of the ADER schemes as applied to the multidimensional nonlinear systems.

The state-expansion ADER schemes need the Godunov state to provide the leading term of the state expansion (1.2). In general, any exact or approximate Riemann solver can be used for this purpose. Here we choose the adaptive Riemann solver described of Sect. 9.5.2 of [65]. We remark that the computational cost of the Riemann solver is very small compared to the overall cost of the scheme, typically around 5%. Other parts of the schemes are considerably more expensive, e.g. the reconstruction procedure takes around 60% of the computing time.

The flux-expansion ADER schemes additionally need a first-order upwind flux to provide the leading term of the flux expansions (2.22),(2.55). We have successfully used a number of upwind fluxes, including the Rusanov flux [38], the Roe flux [37], the HLL flux [20] and the HLLC flux [73]. For general background on fluxes see also [65]. However, the aim of this section is not to assess the performance of different fluxes in the ADER framework. Rather we would like to illustrate the idea of the flux-expansion ADER schemes. Therefore, we present results for only two numerical fluxes, the HLL flux [20] and HLLC flux [73]. The HLL flux assumes a two-wave structure of the Riemann problem solution with wave speeds S_L and S_R.

The HLLC fluxes uses a more accurate three-wave structure, which includes the middle wave with the speed S_*. These wave speeds must be estimated. We use the pressure-velocity estimates of Sect. 10.5.2 of [65].

Additionally, we include the results of the ADER schemes which use the new modification of the DRP solver with the GMUSTA/EVILIN state, see Chapter 1.

For both the state-expansion and the flux-expansion variants of the ADER approach we use the fourth-order Simpson rule for time integration in (2.20), (2.53).

We denote the state-expansion ADER schemes of third and fourth orders of time accuracy, using the adaptive Riemann solver from [65], as ADER3-AD and ADER4-AD respectively. The corresponding flux expansion ADER schemes are denoted as ADER3-HLLC, ADER4-HLLC (the HLLC flux is used) and ADER3-HLL and ADER4-HLL (the HLL flux is used). The schemes with the GMUSTA/EVILIN state are referred to as the ADER-GM schemes.

In our computations we evaluate a stable time step Δt according to

$$\Delta t = C_{cfl} \times \min_{ijk} \left(\frac{\Delta x}{|S_{ijk}^{n,x}|}, \frac{\Delta y}{|S_{ijk}^{n,y}|}, \frac{\Delta z}{|S_{ijk}^{n,z}|} \right). \tag{4.13}$$

Here $S_{ijk}^{n,d}$ is the speed of the fastest wave present at time level n travelling in the d direction, with $d = x, y, z$. C_{cfl} is the CFL number and is chosen according to the linear stability condition of the scheme, namely $0 < C_{cfl} \leq 1/2$ in two space dimensions and $0 < C_{cfl} \leq 1/3$ in three space dimensions. We run all convergence tests with a fixed Courant number close to the stability limit. Usually we use $C_{cfl} = 0.45$ in two space dimensions and $C_{cfl} = 0.3$ in three space dimensions.

We note that the ADER3 schemes with different flxues and the WENO scheme [41] use the same piece-wise parabolic ($r = 3$) reconstruction. Therefore, their comparison is indeed justified. The fourth-order ADER4 schemes use more accurate piece-wise cubic ($r = 4$) WENO reconstruction; therefore their comparison with other schemes must be qualified.

4.3. Shallow water equations

We consider the case of horizontal channels with rectangular cross section. The two-dimensional shallow-water equations with pollutant transport can be written as follows:

$$\partial_t \mathbf{Q} + \partial_x \mathbf{F}(\mathbf{Q}) + \partial_y \mathbf{G}(\mathbf{Q}) = \mathbf{S_1} + \mathbf{S_2}, \tag{4.14}$$

where the vectors of conservative variables $\mathbf{Q}$, fluxes $\mathbf{F}$, $\mathbf{G}$ and source terms $\mathbf{S}_1$, $\mathbf{S}_2$ are given by

$$\mathbf{Q} = \begin{pmatrix} h \\ hu \\ hv \\ h\psi \end{pmatrix}, \quad \mathbf{F} = \begin{pmatrix} hu \\ hu^2 + \frac{1}{2}gh^2 \\ huv \\ hu\psi \end{pmatrix}, \tag{4.15}$$

$$\mathbf{G} = \begin{pmatrix} hv \\ hvu \\ hv^2 + \frac{1}{2}gh^2 \\ hv\psi \end{pmatrix}. , \quad \mathbf{S_1} = \begin{pmatrix} 0 \\ -gb_x h \\ -gb_y h \\ 0 \end{pmatrix}. \tag{4.16}$$

Here u and v are respectively x and y components of velocity, h is the depth, b is the bed elevation, $g = 9.8$ is acceleration due to the gravity and ψ is concentration of pollutant.

4.3.1. Dam-break problem

We solve a circular dam-break problem which corresponds to the following initial condition defined on $[-20:20] \times [-20:20]$:

$$\begin{gathered} (h, \psi) = \begin{cases} (2.5, 1) & r \leq 2.5, \\ (0.5, 0) & r > 2.5, \end{cases} \\ u = v = 0, \quad r^2 = x^2 + y^2. \end{gathered} \tag{4.17}$$

Here we compute the numerical solution at two output times $t = 0.4$ and $t = 4.7$ on a mesh of 201 cells in each coordinate direction. We use $C_{cfl} = 0.45$ for all runs. We compare the results of the ADER4 scheme with a reference radial solution, which is obtained by solving numerically the following one-dimensional shallow-water equations with a geometric source term

$$\partial_t \begin{pmatrix} h \\ hv_r \\ h\psi \end{pmatrix} + \partial_r \begin{pmatrix} hv_r \\ hv_r^2 + \frac{1}{2}gh^2 \\ h\psi v_r \end{pmatrix} = -\frac{1}{r} \begin{pmatrix} hv_r \\ hv_r^2 \\ h\psi v_r \end{pmatrix}$$

on a very fine mesh. See Chapter 13 of [66] for details. Figs. 4.8–4.10 show a comparison between the one-dimensional reference radial solution (solid line) and the cell averages of the two-dimensional ADER4 solution (symbols) along the radial line that is coincident with the x-axis. We present distributions of depth h, velocity u and pollutant concentration ψ.

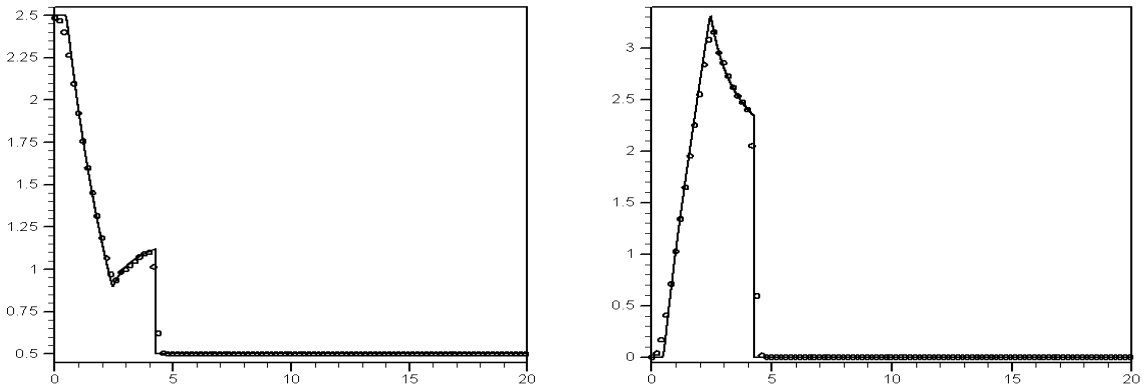

Figure 4.8. The circular dam-break problem. Depth (left) and velocity (right) for the ADER4 scheme at the output time $t = 0.4$.

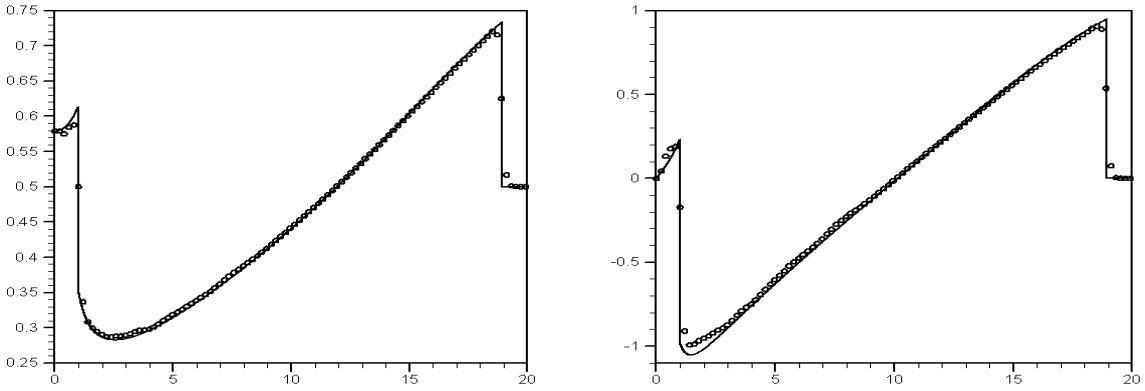

Figure 4.9. The circular dam-break problem. Depth (left) and velocity (right) for the ADER4 scheme at the output time $t = 4.7$.

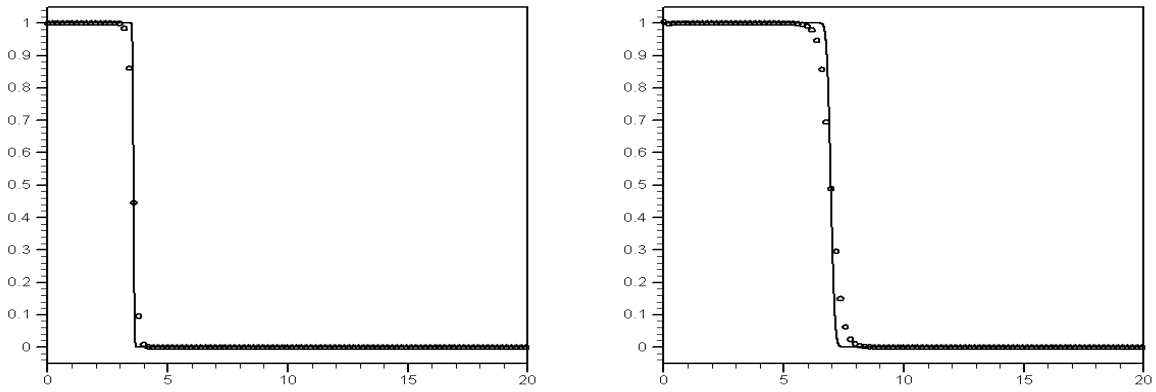

Figure 4.10. The circular dam-break problem. Pollutant transport for the ADER4 scheme at the output times $t = 0.4$ (left) and $t = 4.7$ (right).

A detailed numerical study of this problem for a sequence of output times is given in Chapter 13 of [66]. At time $t = 0.4$, see Fig. 4.8, the solution contains an outward-propagating circular shock wave and an inward-propagation rarefaction wave which is about to reach the origin. Then the rarefaction reflects from the origin and has overexpanded the flow to the point that the depth falls well below the ambient depth initially outside the circular dam. A secondary circular shock is then formed, which is more clearly seen in the velocity profile. This shock initially propagates inwards and then reflects from the centre. At the final time $t = 4.7$, see Fig. 4.9, it is propagating outwards.

We observe that the ADER4 scheme produces the correct flow pattern for all output times. A complex process of implosion of the circular shock in the centre and formation of a reflected outward-moving circular shock does not lead to the generation of oscillations in the numerical solution. Overall, representation of shocks is quite sharp, with only 2-3 cells across them.

4.3.2. Smooth convergence test

We consider a time-dependent flow with periodic boundary condtions in a domain $[-5:5]^2$. We take the exact solution in the following form:

$$\begin{pmatrix} h \\ hu \\ hv \\ h\varphi \end{pmatrix} = \begin{pmatrix} 5 + \sin \pi t \sin \pi x \sin \pi y \\ (5 + \sin \pi t \sin \pi x \sin \pi y) \sin \pi t \sin \pi x \\ (5 + \sin \pi t \sin \pi x \sin \pi y) \sin \pi t \sin \pi y \\ (5 + \sin \pi t \sin \pi x \sin \pi y) \sin \pi t \sin \pi x \sin \pi y \end{pmatrix} \tag{4.18}$$

The bottom elevation has the form: $b(x, y) = \exp(-\alpha(x^2 + y^2)$, with $\alpha = 10$. The second part of the source term $\mathbf{S}_2$ is adjusted in such a way that we have the exact solution given above.

We present convergence results for the output time $t = 1$ for third and fourth order ADER schemes.

Table 16 shows the convergence study for ADER3 and ADER4 schemes The errors of cell averages of the solution in L_∞ and L_1 norms are presented. We observe that approximately fifth order of accuracy is achieved by all schemes. It is interesting to note that these orders of accuracy actually exceed the fourth order accuracy of the two-point Gaussian rule used for flux integration.

Table 16 . Convergence test for ADER schemes as applied to equations (4.14) with the exact solution (4.18).

Method	Mesh	L_∞ error	L_∞ order	L_1 error	L_1 order
ADER3	25×25	2.82×10^{-2}		7.55×10^{-1}	
	50×50	8.53×10^{-3}	1.73	2.33×10^{-1}	1.69
	100×100	4.54×10^{-4}	4.23	4.26×10^{-3}	5.78
ADER4	25×25	6.92×10^{-3}		3.35×10^{-1}	
	50×50	2.06×10^{-3}	1.75	7.31×10^{-2}	2.19
	100×100	7.15×10^{-5}	4.85	1.49×10^{-3}	5.61

4.4. Compressible Euler equations

We consider the compressible Euler equations of the form (2.44) with

$$\mathbf{Q} = \begin{pmatrix} \rho \\ \rho u \\ \rho v \\ \rho w \\ E \end{pmatrix}, \quad \mathbf{F} = \mathbf{Q}u + \begin{pmatrix} 0 \\ p \\ 0 \\ 0 \\ pu \end{pmatrix}, \quad \mathbf{G} = \mathbf{Q}v + \begin{pmatrix} 0 \\ 0 \\ p \\ 0 \\ pv \end{pmatrix}, \quad \mathbf{H} = \mathbf{Q}w + \begin{pmatrix} 0 \\ 0 \\ 0 \\ p \\ pw \end{pmatrix}, \tag{4.19}$$

$$p = (\gamma - 1)(E - \frac{1}{2}\rho(u^2 + v^2 + w^2)).$$

Here ρ, u, v, w p and E are density, components of velocity in the x, y and z coordinate directions, pressure and total energy, respectively; γ is the ratio of specific heats. We use $\gamma = 1.4$ throughout.

We assess the performance our methods as applied to several test problems, as detailed in the following subsections.

Table 17 . Convergence study for various schemes as applied to the Euler equations (1.7) with initial condition (4.20) at output time $t = 2$. All schemes are used with CFL=0.95.

Method	N	L_∞ error	L_∞ order	L_1 error	L_1 order
ADER3-AD	20	1.45×10^{-1}		1.29×10^{-1}	
	40	1.29×10^{-2}	3.49	1.03×10^{-2}	3.65
	80	2.29×10^{-3}	2.49	1.18×10^{-3}	3.13
	160	2.69×10^{-4}	3.09	1.01×10^{-4}	3.55
ADER3-WAF	20	9.80×10^{-2}		7.71×10^{-2}	
	40	6.07×10^{-3}	4.01	6.58×10^{-3}	3.55
	80	1.03×10^{-3}	2.56	6.27×10^{-4}	3.39
	160	1.43×10^{-4}	2.85	6.59×10^{-5}	3.25
ADER5-AD	20	2.79×10^{-2}		3.09×10^{-2}	
	40	1.91×10^{-3}	3.87	6.96×10^{-4}	5.47
	80	1.05×10^{-5}	7.51	3.50×10^{-6}	7.64
	160	6.67×10^{-8}	7.29	4.09×10^{-8}	6.42
ADER5-WAF	20	1.58×10^{-2}		1.77×10^{-2}	
	40	1.24×10^{-3}	3.68	4.75×10^{-4}	5.22
	80	8.83×10^{-6}	7.13	3.72×10^{-6}	6.99
	160	7.79×10^{-8}	6.82	7.86×10^{-8}	5.57

4.4.1. Convergence studies in 1D

This test problem is chosen to study the convergence properties of the schemes. We solve the one-dimensional Euler equations (1.7) for a γ-law gas, with $\gamma = 1.4$, for the following initial condition, defined on [-1,1]:

$$u = p = 1, \quad \rho = 2 + (\sin \pi x)^4 \,, \tag{4.20}$$

so that the exact solution is $\rho(x,t) = 2 + [\sin(\pi(x-t))]^4$, $u = p = 1$. Periodic boundary conditions are used. The error of *cell averages* is measured at the output time $t = 2$ (one time period). Table 17 shows convergence rates and errors for density in different norms. We observe that all ADER-AD and ADER-WAF schemes reach the expected order of accuracy. In fact, the fifth order schemes well exceed the designed fifth order of accuracy. In particular, we note that the use of the

TVD flux, when used with a compressive limiter, does not affect the convergence properties of the ADER-WAF schemes. Moreover, for the third order scheme the accuracy actually improves.

At this stage, it is informative to remark that such high orders of accuracy are achieved under nearly optimal Courant number CFL=0.95, and by *non-linear* (non-oscillatory) schemes which produce essentially non-oscillatory results, as we demonstrate below. These schemes may be used for solving practical problems involving discontinuous solutions or large gradients.

4.4.2. Modified shock/turbulence interaction

Here we use a test problem that is a modification of the shock/turbulence problem proposed in [3, 22]. The modification is three-fold. We use (i) a weaker shock wave, (ii) a density fluctuation with frequency four times higher and (iii) an output time ten times larger. The modified test is more appropriate for testing the performance of very-high order schemes.

We solve the Euler equations on $[-5, 5]$ with the initial condition

$$(\rho, u, p) = \begin{cases} (1.515695, 0.523346, 1.80500) \ , & x < -4.5 \ , \\ (1 + 0.1 \sin 20\pi x, 0.0, 1) \ , & x > -4.5 \ . \end{cases} \tag{4.21}$$

The test problem consists of a right facing shock wave of Mach number 1.1 running into a high-frequency density perturbation. As time evolves, the shock moves into this perturbation, which spreads upstream. We compute the solution at the output time $t = 5$.

Results are shown in Figs. 4.11 and 4.12. In all figures, symbols denote the numerical solution and the solid line denotes the reference solution, computed using the ADER5-WAF scheme on a mesh of 5000 cells. The solution contains *physical oscillations* which have to be resolved by the numerical method. It is for such type of problems that sophisticated higher order schemes should give better results than lower order ones. For the calculations shown here we choose a coarse mesh of 1000 cells so that there are only four to five cells between each extrema in the physical oscillations. We use $CFL = 0.95$ for the ADER-AD and ADER-WAF schemes and the smaller $CFL = 0.6$ for the WENO5-RK3 and WENO9-RK3 schemes. We remark that further reduction of the CFL number does not improve the accuracy of the WENO schemes whilst, needless to say, the computational cost increases significantly.

There are three schemes that use piece-wise parabolic reconstruction (fifth order in space) and third-order time discretisation: WENO5, ADER3-AD and ADER3-WAF. See Fig. 4.11. Of these, the most accurate scheme is ADER3-WAF. Next, we have schemes that use reconstruction with fourth-order polynomials (ninth order in space): WENO9, ADER5-AD and ADER5-WAF. See Fig. 4.12. The first of these is third-order in time and the ADER schemes are fifth-order in time. Firstly, we see that the ADER5-AD scheme is more accurate than the WENO9-RK3 scheme. Secondly, the ADE5-WAF scheme is the most accurate scheme for this problem: on a given course mesh it resolves almost all features of the solution.

Therefore, the ADER-WAF schemes are far superior to the corresponding ADER-AD and WENO schemes. The difference in accuracy is evident for schemes of all orders.

4.4.3. Two-dimensional vortex evolution problem

We solve the two-dimensional Euler equations in the square domain $[-5:5]\times[-5:5]$ with periodic boundary conditions. The initial condition corresponds to a smooth vortex placed at the origin and is defined as the following isentropic perturbation to the uniform flow of unit values of primitive variables [3]:

$$\begin{gathered} u = 1 - \frac{\epsilon}{2\pi} e^{\frac{1}{2}(1-r^2)}\, y, \quad v = 1 + \frac{\epsilon}{2\pi} e^{\frac{1}{2}(1-r^2)}\, x, \\ T = 1 - \frac{(\gamma-1)\epsilon^2}{8\gamma\pi^2} e^{(1-r^2)}, \quad \frac{p}{\rho^\gamma} = 1, \end{gathered} \tag{4.22}$$

where $r^2 = x^2 + y^2$ and the vortex strength is $\epsilon = 5$. The exact solution is a vortex movement with a constant velocity at 45^o to the Cartesian mesh lines. We compute the numerical solution at the output time $t = 10$ for which the vortex returns to the initial position. We use $C_{cfl} = 0.45$ for all runs.

Table 18 shows the convergence study for the ADER and WENO schemes with the piece-wise parabolic ($r = 3$) reconstruction. We present errors and convergence rates in L_∞ and L_1 norm for cell averages of density. We observe that the ADER schemes achieve approximately sixth and fifth orders of accuracy in L_∞ and L_1 norms respectively. The ADER-GM scheme is only slightly less accurate than the ADER-AD scheme. It is interesting to note that these orders of accuracy actually exceed the fourth order accuracy of the two-point Gaussian rule used for flux integration. The WENO scheme is less accurate than the ADER schemes by a factor of two on coarse meshes and by a factor of three on the finest mesh. We also note, that the accuracy of the ADER-AD and ADER-HLLC schemes of the same order is very

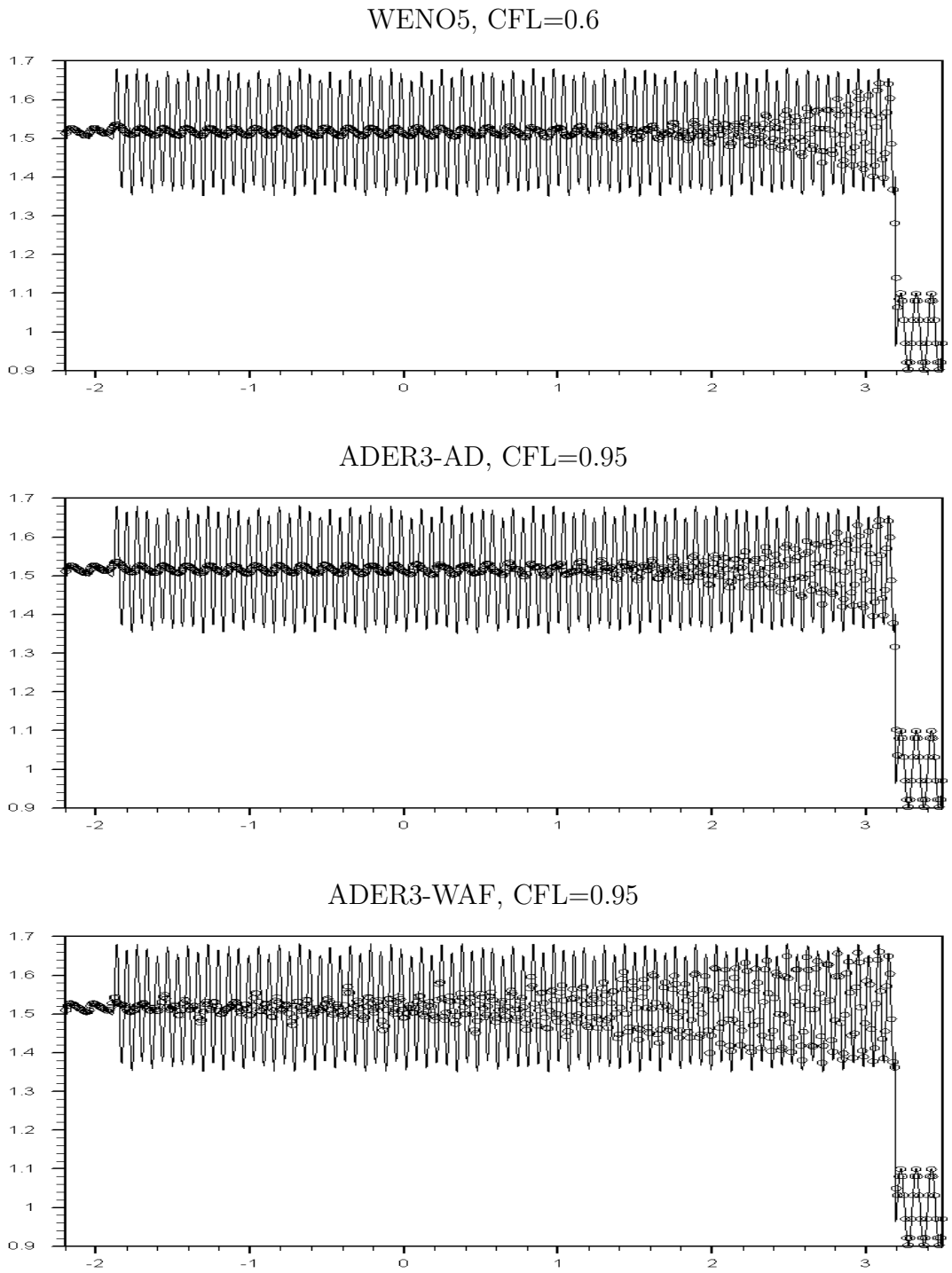

Figure 4.11. Computed (symbol) and reference (line) solutions for the Euler equations (1.7) with initial condition (4.21) at output time $t = 5$ for schemes with piece-wise parabolic reconstruction. The mesh of N=1000 cells is used.

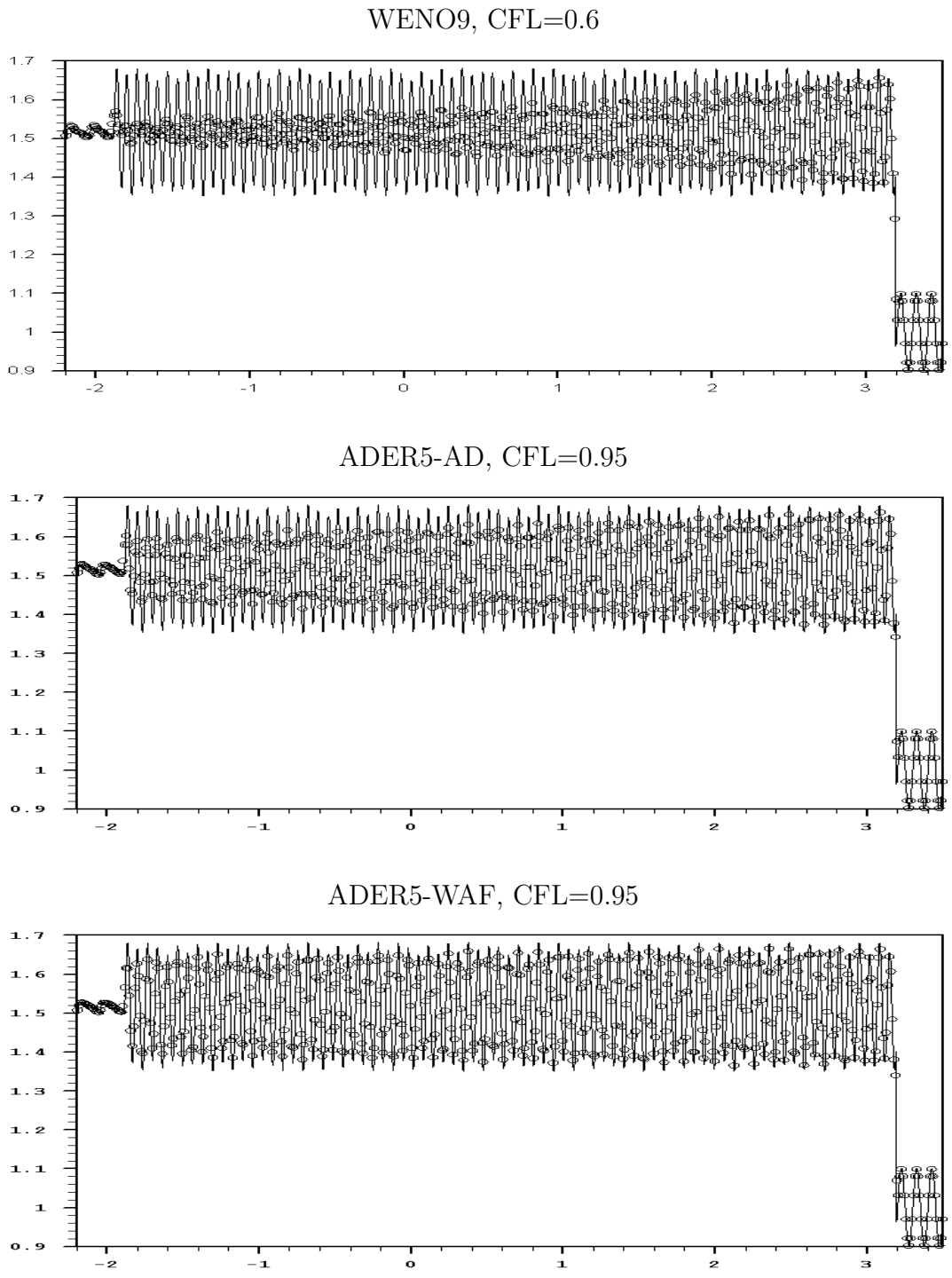

Figure 4.12. Computed (symbol) and reference (line) solutions for the Euler equations (1.7) with initial condition (4.21) at output time $t = 5$ for schemes with piece-wise quadric reconstruction. The mesh of N=1000 cells is used.

Table 18 . Density convergence study for the vortex evolution problem (4.22) for schemes with piece-wise parabolic ($r = 3$) reconstruction.

Method	Mesh	L_∞ error	L_∞ order	L_1 error	L_1 order
ADER3-AD	25×25	5.94×10^{-2}		3.43×10^{-1}	
	50×50	8.90×10^{-3}	2.74	2.50×10^{-2}	3.78
	100×100	2.62×10^{-4}	5.08	8.83×10^{-4}	4.82
	200×200	4.55×10^{-6}	5.85	3.58×10^{-5}	4.62
ADER3-HLLC	25×25	5.94×10^{-2}		3.43×10^{-1}	
	50×50	8.94×10^{-3}	2.73	2.50×10^{-2}	3.78
	100×100	2.63×10^{-4}	5.09	8.83×10^{-4}	4.82
	200×200	4.68×10^{-6}	5.81	3.61×10^{-5}	4.61
ADER3-HLL	25×25	6.08×10^{-2}		3.87×10^{-1}	
	50×50	9.32×10^{-3}	2.71	2.64×10^{-2}	3.88
	100×100	2.86×10^{-4}	5.02	9.97×10^{-3}	4.73
	200×200	4.90×10^{-6}	5.87	3.79×10^{-5}	4.72
ADER3-GM	25×25	1.01×10^{-1}		6.29×10^{-1}	
	50×50	1.42×10^{-2}	2.83	4.20×10^{-2}	3.91
	100×100	4.58×10^{-4}	4.96	1.63×10^{-3}	4.69
	200×200	9.97×10^{-6}	5.52	5.15×10^{-5}	4.98
WENO [41]	25×25	1.04×10^{-1}		6.92×10^{-1}	
	50×50	1.38×10^{-2}	2.91	4.58×10^{-2}	3.92
	100×100	4.60×10^{-4}	4.91	2.33×10^{-3}	4.30
	200×200	1.67×10^{-5}	4.78	9.05×10^{-5}	4.68

Table 19 . Density convergence study for the vortex evolution problem (4.22) at the output time $t = 10$. ADER schemes with piece-wise cubic ($r = 4$) reconstruction

Method	Mesh	L_∞ error	L_∞ order	L_1 error	L_1 order
ADER4-AD	25×25	1.96×10^{-2}		1.15×10^{-1}	
	50×50	1.59×10^{-3}	3.62	5.43×10^{-3}	4.40
	100×100	2.52×10^{-5}	5.98	1.29×10^{-4}	5.39
	200×200	4.14×10^{-7}	5.93	1.81×10^{-6}	6.16
ADER4-HLLC	25×25	1.96×10^{-2}		1.15×10^{-1}	
	50×50	1.60×10^{-3}	3.62	5.43×10^{-3}	4.40
	100×100	2.52×10^{-5}	5.98	1.29×10^{-4}	5.40
	200×200	4.14×10^{-7}	5.93	1.80×10^{-6}	6.16
ADER4-HLL	25×25	1.90×10^{-2}		1.15×10^{-1}	
	50×50	1.61×10^{-3}	3.56	5.68×10^{-3}	4.34
	100×100	2.79×10^{-5}	5.85	1.44×10^{-4}	5.31
	200×200	4.49×10^{-7}	5.96	1.95×10^{-6}	6.20

similar whereas the ADER-HLL schemes are slightly less accurate, which is due to the use of the less accurate HLL Riemann solver.

We also remark that all ADER schemes are more accurate than the WENO scheme by a factor between two and three. The observed difference in accuracy between ADER and WENO schemes can be related to the more accurate time evolution method of the ADER approach as compared to the combination of the Rusanov flux and the TVD RK method in the WENO scheme.

Table 19 shows the convergence study for the fourth order ADER schemes with the higher-order piece-wise cubic ($r = 4$) reconstruction. We observe approximately sixth order of accuracy in both norms. For a fixed resolution the fourth order ADER schemes are more accurate than the schemes of Table 18 by a factor of ten.

4.4.4. Double Mach reflection of a strong shock

The setup of the problem is as follows [83]. The domain of interest is a region of 4 units long and 1 unit wide. At the initial time $t = 0$ a right-moving shock wave of shock Mach number equal to 10 is set up. The shock front makes an angle of 60^o with the x-axis at $x = 1/6$. Ahead of the shock the gas is at rest with $\rho = 1.4$, $p = 1$. The following boundary conditions are used. The in-flow boundary condition is applied at the left vertical boundary $x = 0$ and transmissive boundary conditions are used at the right vertical boundary $x = 4$. At the bottom boundary $y = 0$ the exact post-shock values of all gas parameters are set for $0 \leq x \leq 1/6$ whereas for $1/6 < x \leq 4$ reflective boundary conditions are used. The exact motion of the Mach 10 shock is prescribed at the top boundary $y = 1$. The solution is studied for the output time $t = 1/5$.

Figs. 4.13–4.20 show numerical results of the third-order ADER3-AD, ADER3-HLLC, ADER3-HLL and ADER3-GM schemes for three meshes: 480×120, 960×240 and 1920×480 cells. The corresponding results of the WENO scheme can be found in Fig. 3.4 of [41] and are not shown here. Comparing our results with those in the existing literature [83, 22, 11, 21, 41] it is seen that ADER schemes produce the flow pattern generally accepted at present as correct, on all meshes. All discontinuities are well resolved and correctly positioned. Comparing ADER new schemes, and the WENO scheme [41], we see that the main difference occurs in the resolution of the slip surfaces and the associated jet. This is partly explained by the numerical flux. The adaptive Riemann solver used to compute the leading term of the state expansion (2.50) in the ADER3 scheme and the HLLC Riemann solver used for the leading term of the flux expansion (2.55) in the ADER3-HLLC scheme recognize all these waves. In fact, the numerical results of the ADER3-AD and ADER3-HLLC schemes are very similar, almost identical. The HLL and the Rusanov fluxes used in the ADER3-HLL and the WENO schemes ignore the internal structure of the Riemann problem solution and thus smear the slip surfaces more significantly [73]. The overall accuracy of the ADER3-GM scheme compares well with that of the WENO scheme [41] and conventional state-expansion ADER schemes.

Additionally, we observe that all ADER schemes produce much sharper profiles of the shock waves as compared with the WENO scheme [41]. Presumably, this should be attributed to the one-step framework of the ADER approach.

On the finest mesh we begin to see the appearance of the Kelvin-Helmholtz instability (rolling) of the slip surface. We remark that slip surfaces are physically unstable features of the flow, the converged solution of which can only be obtained

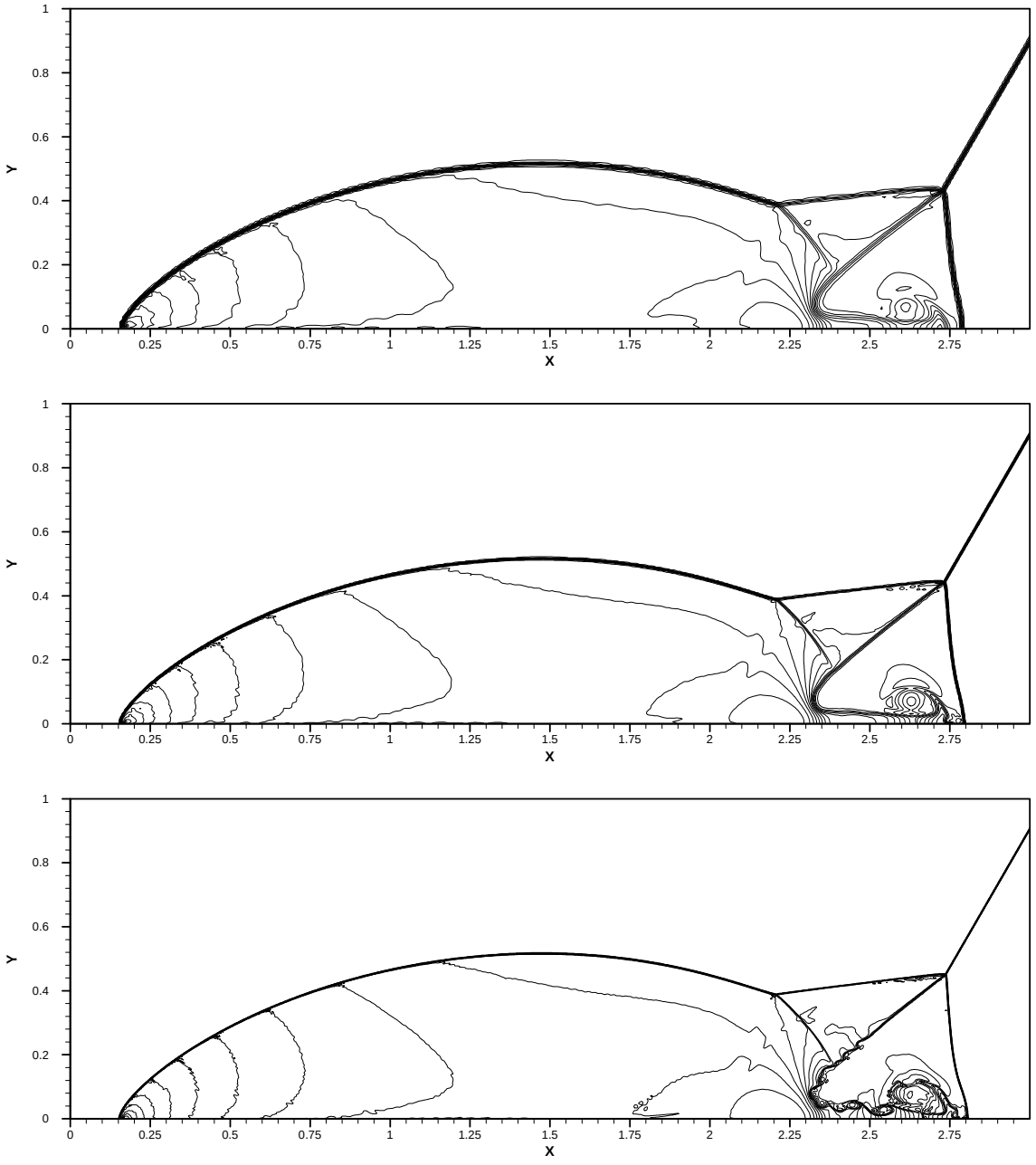

Figure 4.13. Density convergence study for the double Mach reflection problem. Method: the ADER3-AD scheme. 30 contour lines from 2 to 22.

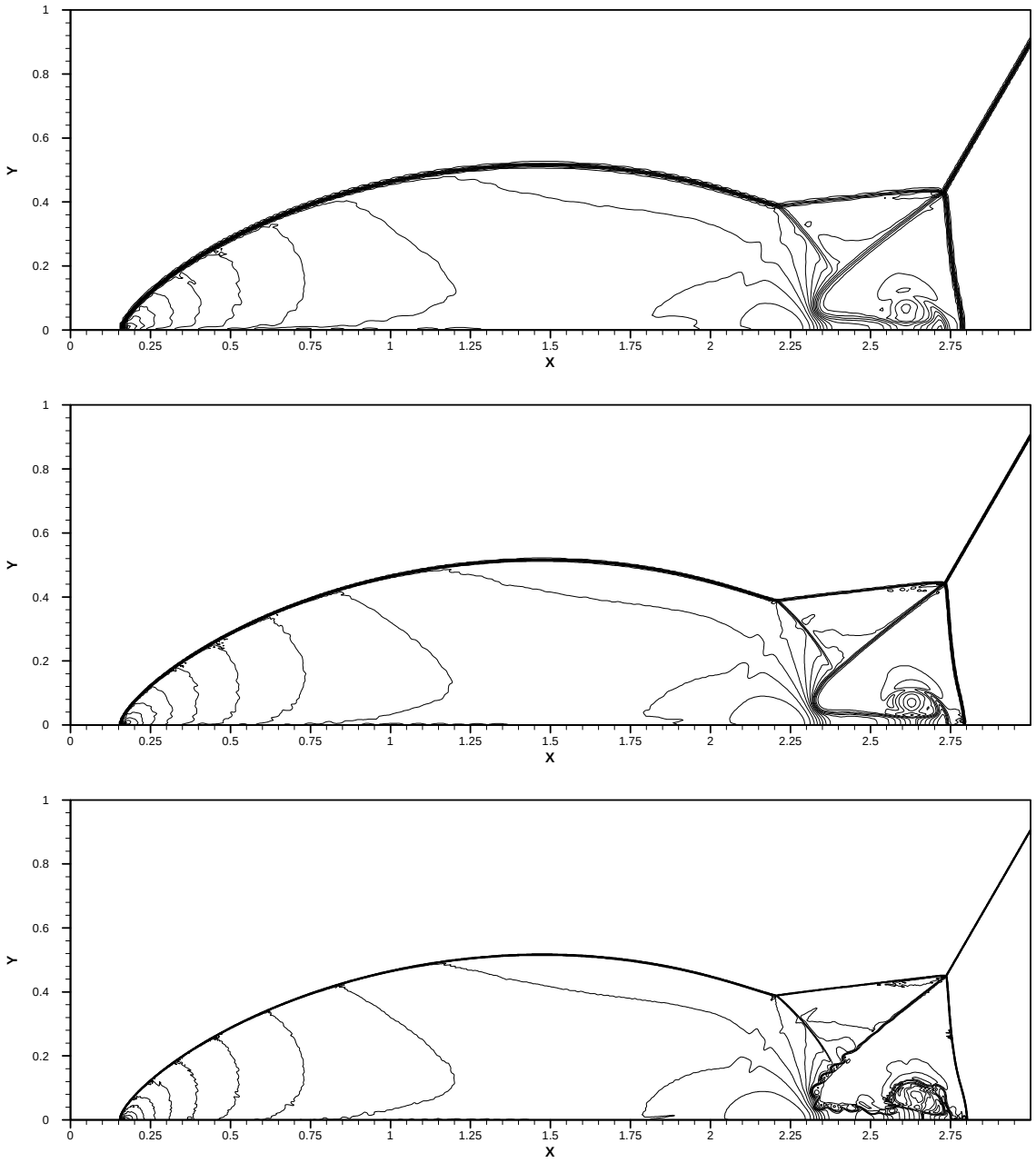

Figure 4.14. Density convergence study for the double Mach reflection problem. Method: the ADER3-HLLC scheme. 30 contour lines from 2 to 22.

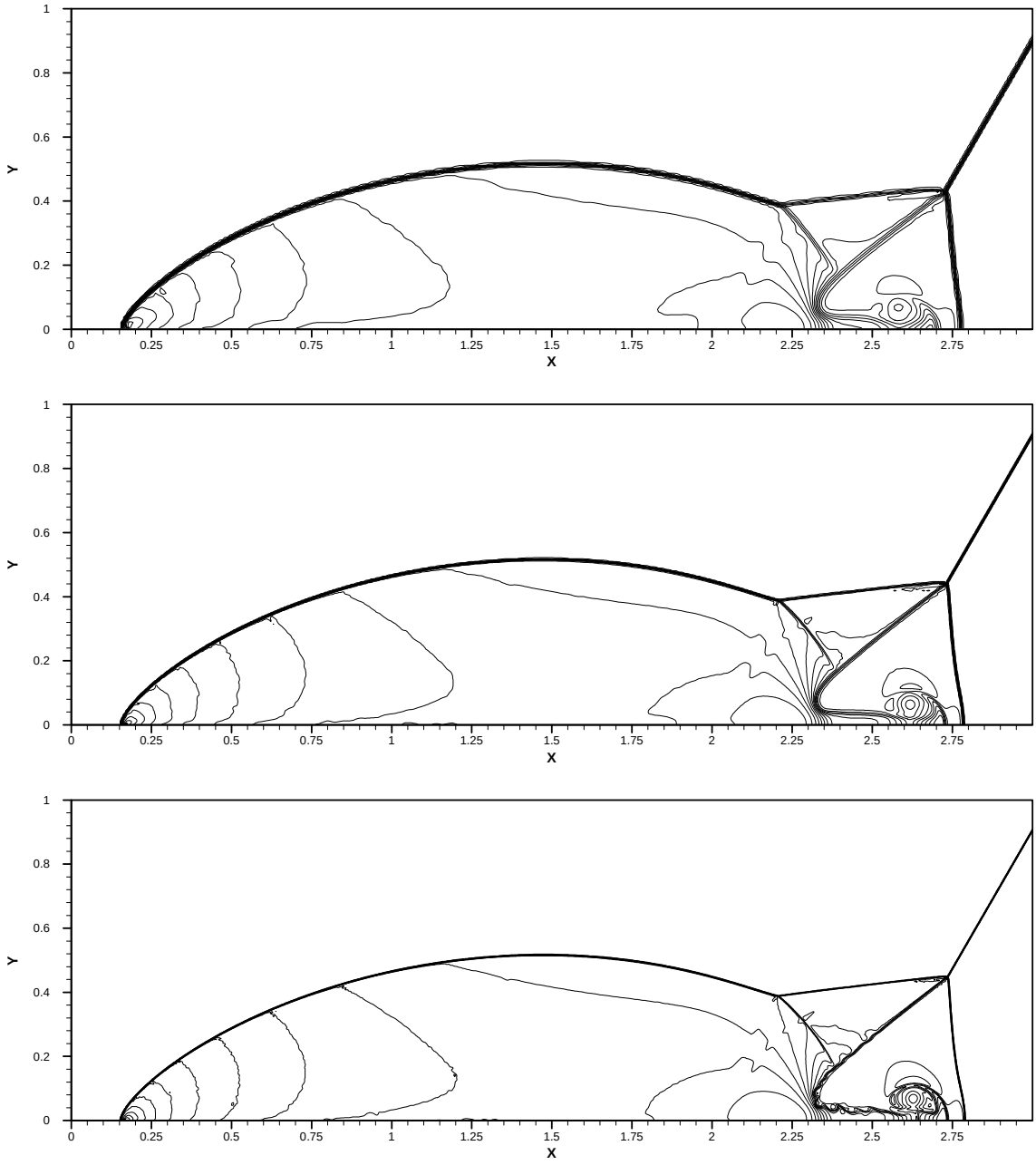

Figure 4.15. Density convergence study for the double Mach reflection problem. Method: the ADER3-HLL scheme. 30 contour lines from 2 to 22.

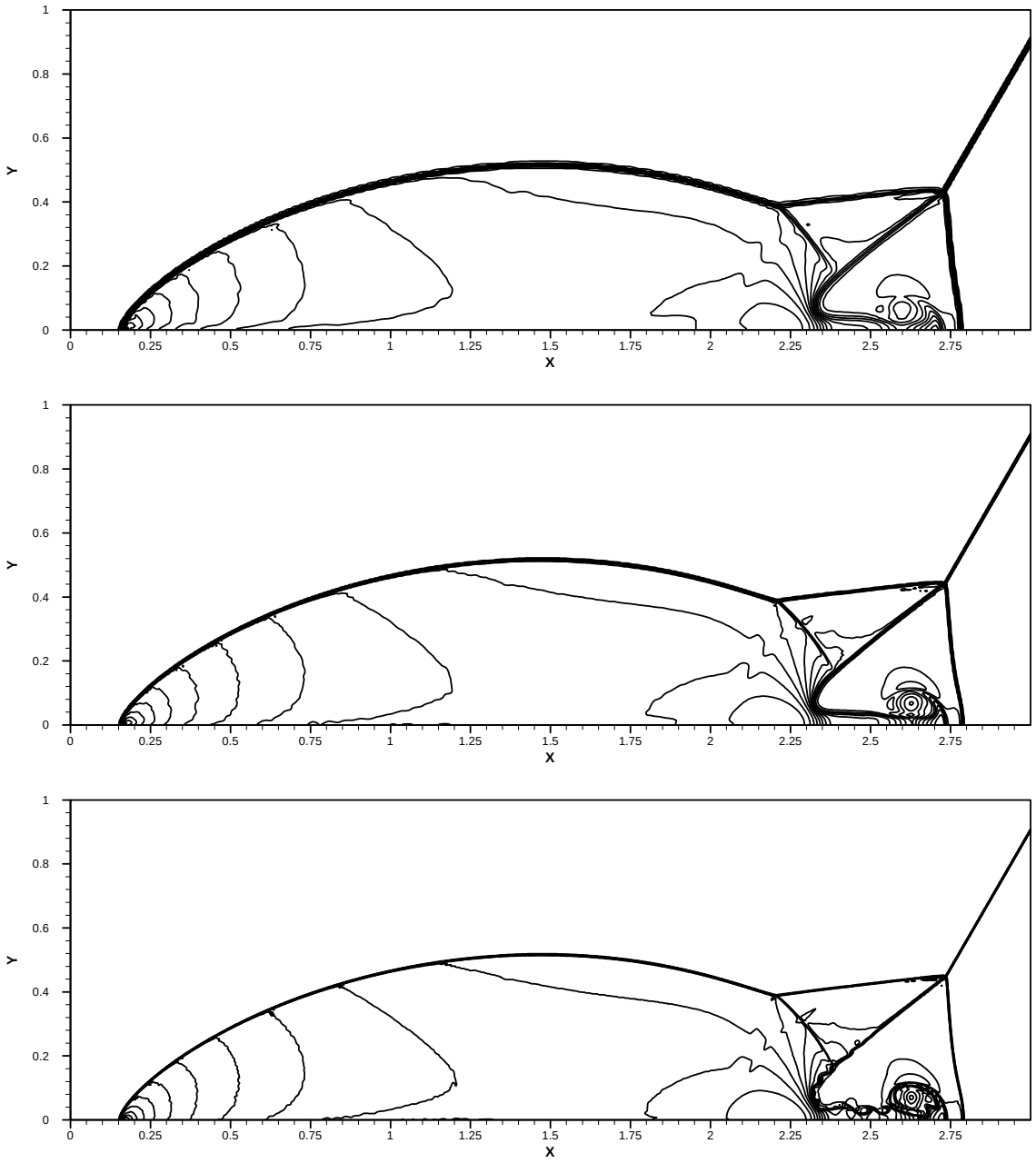

Figure 4.16. Density convergence study for the double Mach reflection problem. Method: the ADER3-GM scheme. 30 contour lines from 2 to 22.

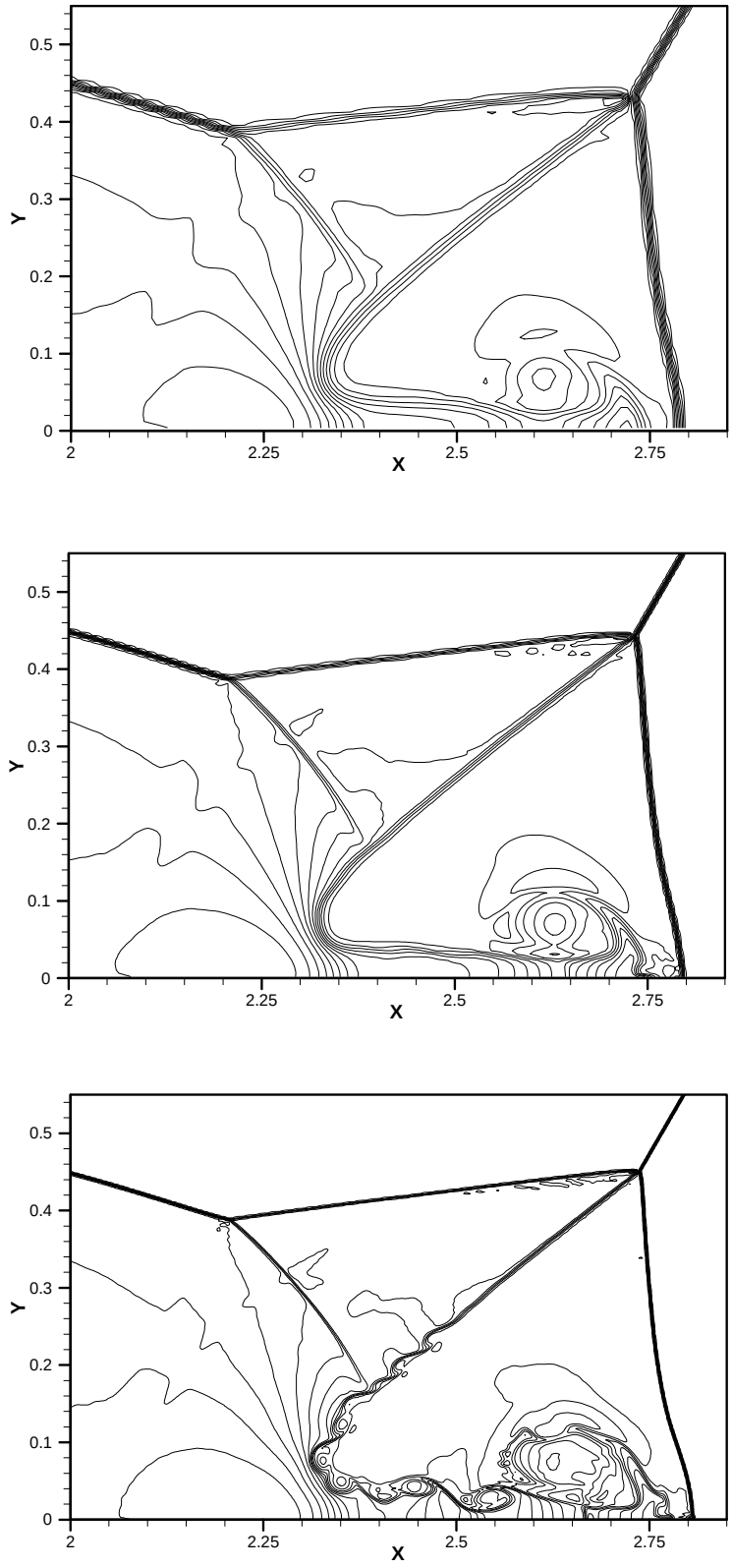

Figure 4.17. Density convergence study for the double Mach reflection problem. Method: the ADER3-AD scheme. Zoomed area of Fig. 4.13.

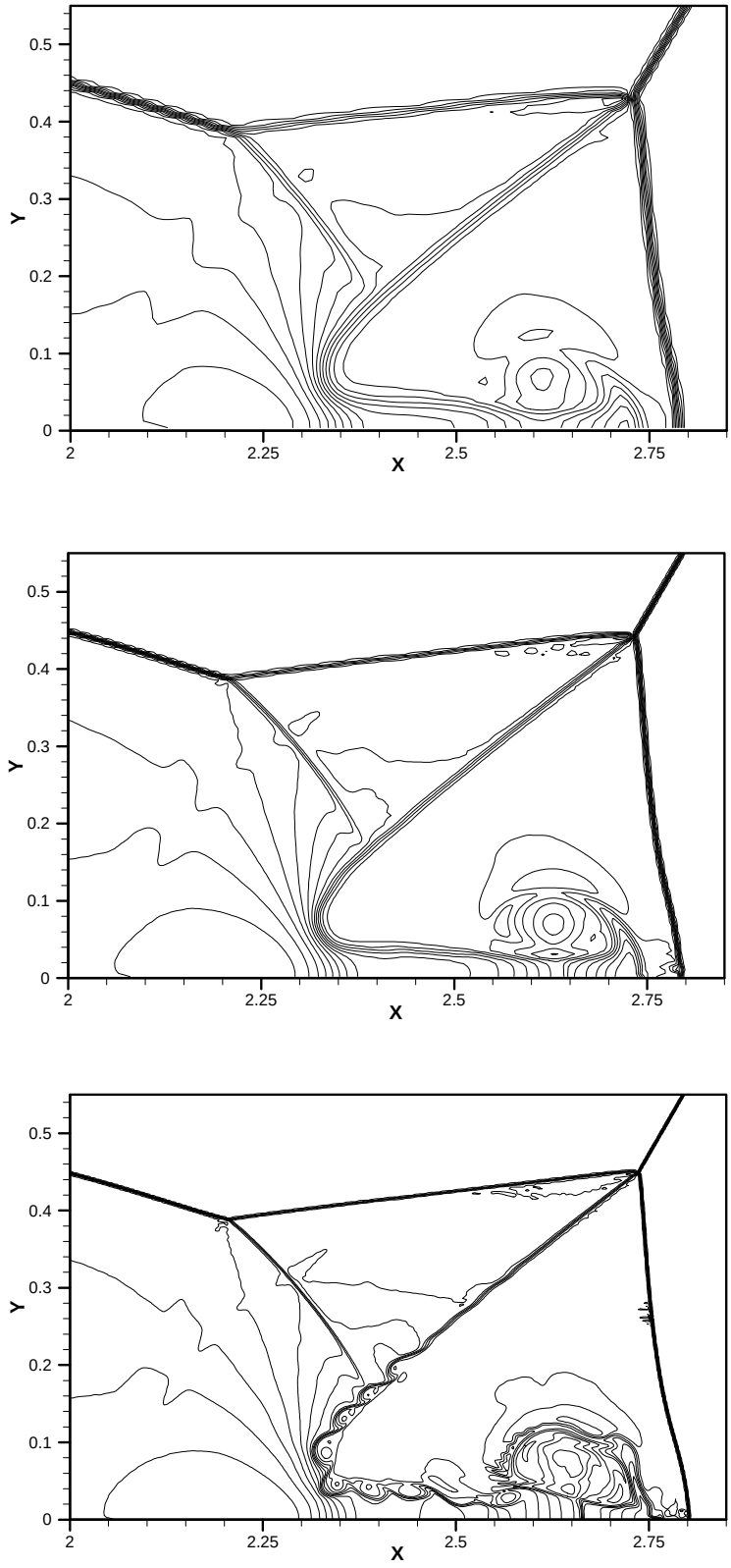

Figure 4.18. Density convergence study for the double Mach reflection problem. Method: the ADER3-HLLC scheme. Zoomed area of Fig. 4.14

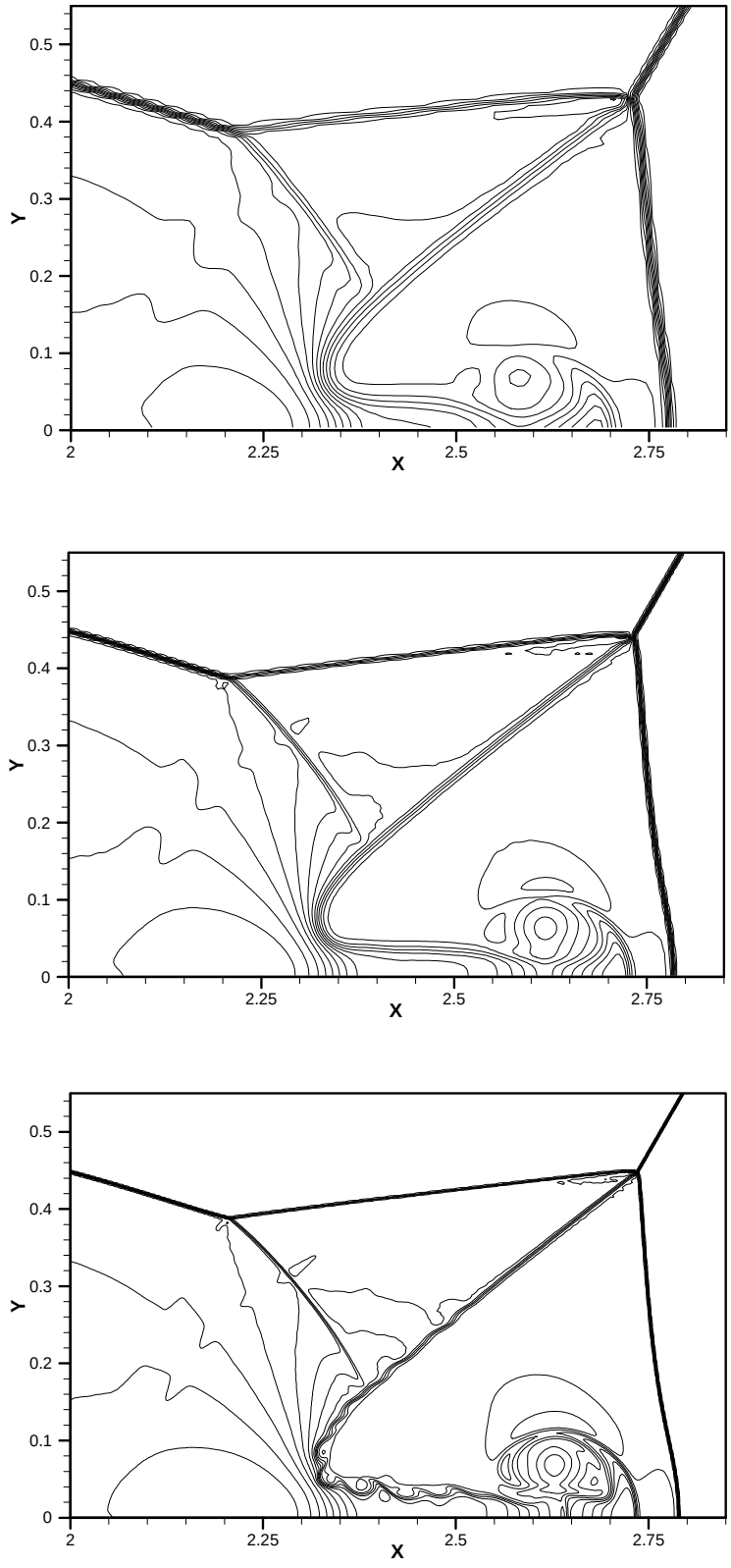

Figure 4.19. Density convergence study for the double Mach reflection problem. Method: the ADER3-HLL scheme. Zoomed area of Fig. 4.15

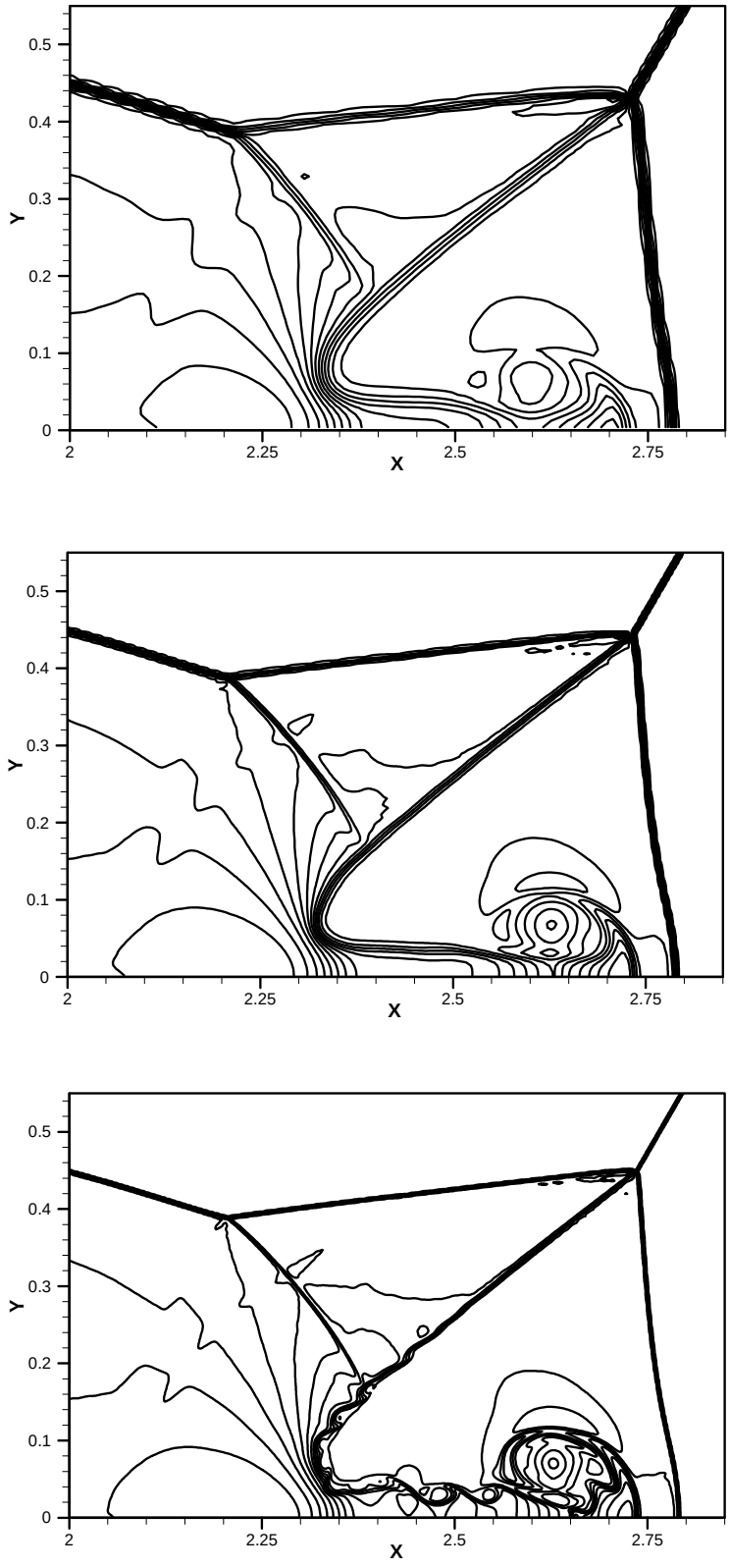

Figure 4.20. Density convergence study for the double Mach reflection problem. Method: the ADER3-GM scheme. Zoomed area of Fig. 4.15

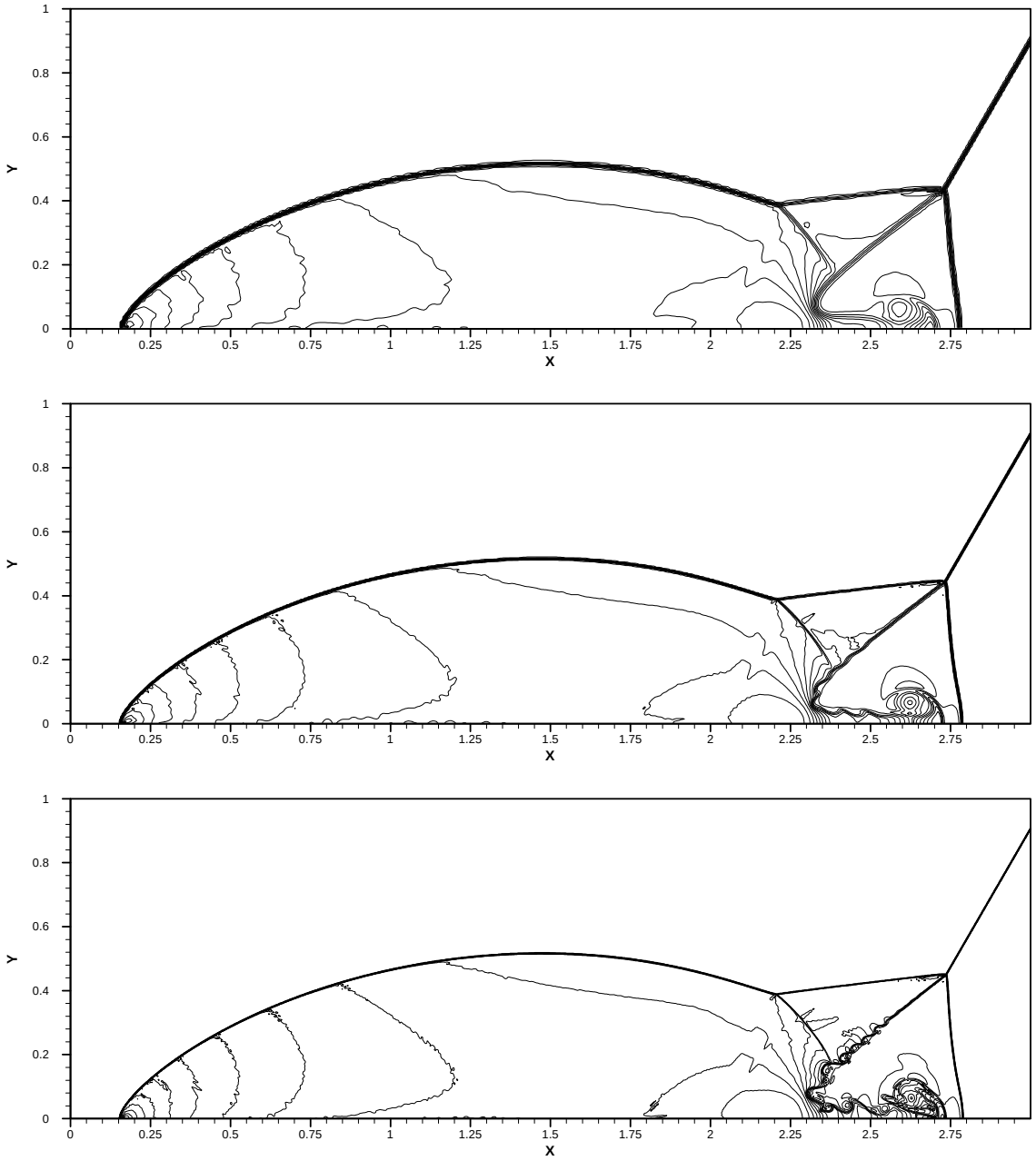

Figure 4.21. Density convergence study for the double Mach reflection problem. Method: the ADER4-HLL scheme. Meshes: 480×120 cells (top) , 960×240 cells (middle) and 1920×480 cells (bottom). 30 contour lines from 2 to 22.

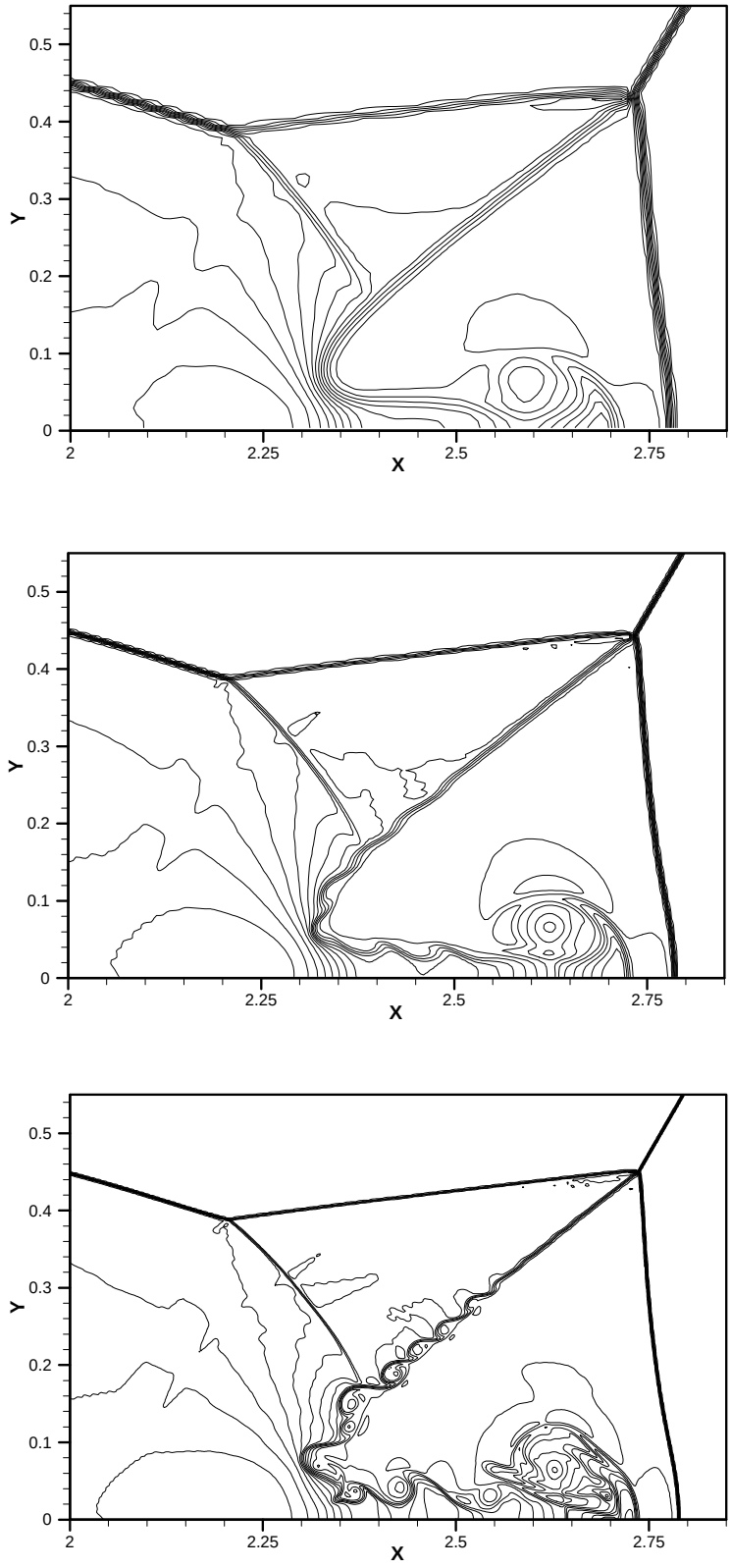

Figure 4.22. Density convergence study for the double Mach reflection problem. Method: the ADER4-HLL scheme. Zoomed area of Fig. 4.21

by solving the Navier-Stokes equations. See e.g. [84] for a numerical study of two-dimensional Rayleigh-Taylor instability. When we use the Euler equations, the viscosity is in fact the numerical viscosity of the method and depends on *the scheme and the mesh* used. As the mesh is refined, no limiting (converged) solution is found. However, for a given particular mesh the numerical solution may exhibit features, typical of physically unstable flows, but with unknown viscosity. Therefore, more pronounced instability of the solution (rolling of the slip surfaces) means smaller numerical diffusion of the ADER3-AD and ADER3-HLLC schemes as compared to the ADER3-HLL scheme and the WENO scheme of [41].

We remark that the resolution of delicate flow features, such as slip surfaces and the jet can be directly related to the accuracy of the Riemann solver used in the scheme. In particular, complete Riemann solvers with all waves in the Riemann problem solution, e.g. exact and HLLC Riemann solvers, give results superior to those of the incomplete ones, such as HLL and Rusanov solvers. We observe that the accuracy of our new ADER-GM scheme is comparable with that of the ADER-HLLC scheme and superior to the ADER3-HLL and WENO schemes.

Figs. 4.21–4.22 show numerical results of the higher-order ADER4-HLL scheme for the same meshes. We observe that the scheme produces the correct flow pattern on all meshes, with thin profiles for discontinuities. Comparing Fig. 4.22 with that of methods with the lower-order piece-wise parabolic reconstruction (see Figs. 4.13–4.19 and [41]) it is seen that the rolling of slip surfaces is much more pronounced in the results of ADER4-HLL scheme. Therefore, the ADER4-HLL scheme has significantly smaller numerical diffusion as compared with the lower-order schemes.

4.4.5. Three-dimensional explosion test problem

Finally, we apply our schemes to the three-dimensional Euler equations (4.19) and solve the spherical explosion test problem [65]. The initial condition defined on $[-1:1]\times[-1:1]\times[-1:1]$ consists of two regions of constant but different values of gas parameters separated by a sphere of radius 0.4:

$$(\rho,p)=\begin{cases}(1.0,\ 1.0), & r\le 0.4\\ (0.125,\ 0.1), & r>0.4\end{cases},\quad u=v=w=0,\quad r^2=x^2+y^2+z^2. \tag{4.23}$$

The numerical solution is computed at the output time $t=0.25$ on a sequence of refined meshes with 25, 51 and 101 cells in each coordinate direction. We use $C_{cfl}=0.3$ for all runs. For this problem we obtain a reference radial solution by

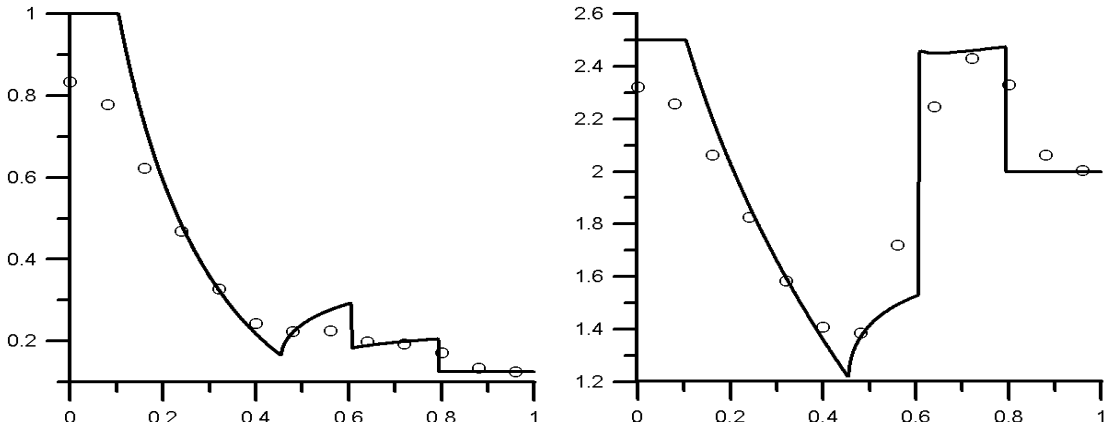

Figure 4.23. Spherical explosion test problem. Computed (symbol) and reference (line) solutions for density (left) and internal energy (right) for the ADER3-AD scheme. A mesh of $25 \times 25 \times 25$ cells is used.

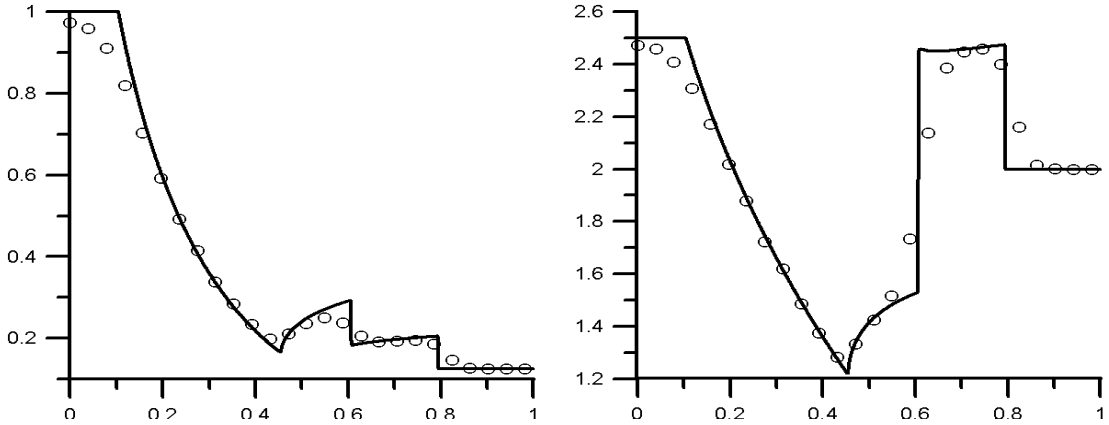

Figure 4.24. Spherical explosion test problem. Computed (symbol) and reference (line) solutions for density (left) and internal energy (right) for the ADER3-AD scheme. A mesh of $51 \times 51 \times 51$ cells is used.

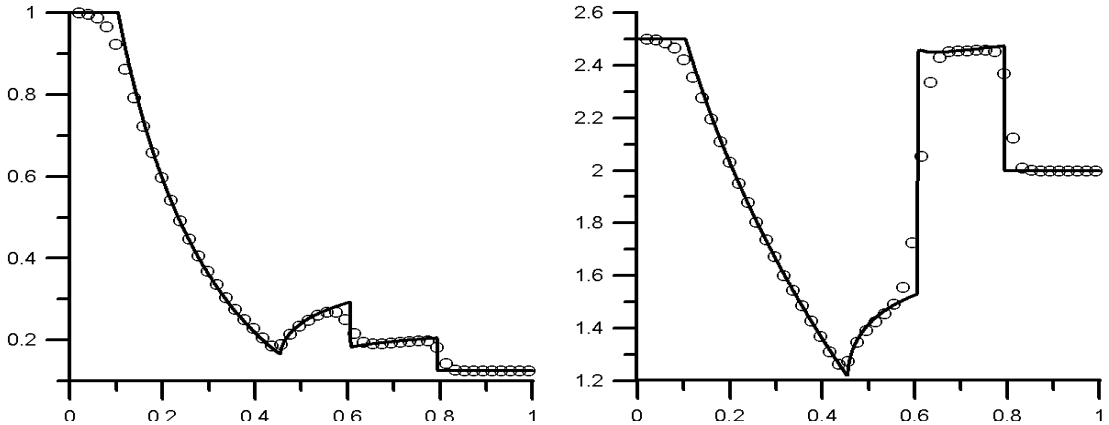

Figure 4.25. Spherical explosion test problem. Computed (symbol) and reference (line) solutions for density (left) and internal energy (right) for the ADER3-AD scheme. A mesh of $101 \times 101 \times 101$ cells is used.

solving numerically the following one-dimensional Euler equations with a geometrical source term:

$$\frac{\partial}{\partial t}\begin{pmatrix}\rho\\ \rho V_r\\ E\end{pmatrix}+\frac{\partial}{\partial r}\begin{pmatrix}\rho V_r\\ \rho V_r^2+p\\ (E+p)V_r\end{pmatrix}=-\frac{2}{r}\begin{pmatrix}\rho V_r\\ \rho V_r^2\\ (E+p)V_r\end{pmatrix}$$

where V_r is the radial velocity. We use the Weighted Average Flux (WAF) method [61, 65] on a very fine mesh.

Figs. 4.23–4.25 show a comparison between the one-dimensional reference radial solution (solid line) and the cell averages of the three-dimensional ADER3-AD solution (symbols) along the radial line that is coincident with the x-axis. We present distributions of gas density ρ and internal energy $e = T/(\gamma - 1)$ for $x > 0$. The solution contains a spherical shock wave and a contact surface travelling away from the centre and a spherical rarefaction wave travelling towards the origin (0,0,0). We observe that the scheme produce the correct flow patter with the correct values behind the shock wave and the contact surface. As the mesh is refined, the numerical solution approaches the reference solution. No oscillations are present.

The results of the ADER3-HLLC and ADER3-HLL schemes are essentially the same and are thus omitted.

4.5. Cost comparison of the schemes

Table 20 shows approximate computing times for the schemes with piece-wise parabolic reconstruction as applied to the double Mach reflection problem. All numbers are normalized by the computing time of the ADER3-AD scheme. We see that the third-order ADER schemes are faster than the WENO scheme with the Rusanov flux roughly by 66% for the state expansion version and for 40% for the flux expansion version with the EVILIN flux. The reason for this is twofold. Firstly, our scheme needs to perform the very costly characteristic projections and smoothness indicators computations in the reconstruction procedure only once during one time step. Secondly, the ADER scheme uses the two-point integration rule to evaluate the numerical fluxes whereas the WENO scheme in the cited reference uses the three-point Gaussian rule.

The gain in computational cost of ADER schemes over the WENO schemes with Runge-Kutta time stepping is similar to that of the finite-difference WENO schemes with Cauchy-Kowalewski procedure over the finite-difference WENO schemes with Runge-Kutta time stepping [34].

Table 20 . Approximate computation times for the double Mach reflection problem.

Method	Normalized computing time
ADER3-AD	100%
ADER3-HLLC	104%
ADER3-GM with $k = M = 1$	112%
WENO [41], Rusanov flux	166%

The fourth order ADER schemes in two space dimensions are more expensive than the corresponding third order ADER schemes by a factor of three. This is due to substantially more expensive reconstruction procedure and more complicated fluxes.

Secondly, we discuss the memory requirement of the schemes. The ADER schemes of any order effectively need only two global arrays to store the vector of the conservative variables and the total sum of fluxes. The WENO schemes with the third order three-stage TVD Runge-Kutta method [42] need at least three such arrays. Note that expensive memory transfers may be needed for the RK method in this case. For the fourth order *five stage* SSP RK method [45] the memory requirements are substantially higher. In summary, the memory requirements of the ADER schemes are significantly smaller than those of the WENO schemes with RK time discretizations.

Conclusions

We implemented schemes of up to fifth order of temporal accuracy (fifth and seventh order of spatial accuracy, respectively). We presented the numerical results for scalar linear and nonlinear equations as well as for multidimensional nonlinear systems. These illustrate the very high order of accuracy as well as the essentially non-oscillatory properties of the ADER schemes. Comparisons with the state-of-art WENO schemes [41] show that the ADER schemes are faster, more accurate and need less computer memory.

Conclusions and future work

This thesis has focused on the further construction and generalization of the ADER advection schemes to the case of non-linear multi-dimensional conservation laws with reactive-like source terms. The main results can be summarized as follows:

1. A new variant of the Derivative Riemann problem solver has been presented, which can be applied to systems for which the solution of the conventional Riemann problem is not available or is exceedingly complicated. The extension consists of modifying the procedure of the computation of the leading term whereas high-order terms are left intact.

2. The schemes have been extended to multidimensional *non-linear* hyperbolic systems with reactive-like source terms. This required a suitable extension of the DRP solver for the split multidimensional case, development of the 3D reconstruction procedure as well as development of the WENO weights for Gaussian quadrature points and for the higher orders of accuracy.

3. In one space dimension a special version of the schemes, called ADER-TVD, has been developed by replacing the first order flux by a second order limited flux for all terms in the Taylor time expansion in the DRP solution. The use of a a superbee-type limiter has resulted in much better accuracy for long time evolution problems without the squaring effect typical of TVD methods with compressive limiters.

4. Truncation error and stability analysis of the schemes for the model linear advection equation with constant coefficients in one, two and three space dimensions has been performed. It shows that the ADER schemes are stable under conventional CFL numbers similar to those for the WENO schemes and retain the design order of accuracy.

5. Extensive numerical evaluation of the schemes as applied to a number of the well-established test problems has been performed. Up to fifth order of temporal accuracy has been demonstrated. Non-oscillatory results have been obtained for problems with strong discontinuities. A detailed comparison with the state-of-the art finite-volume WENO schemes has been carried out. Overall, our methods compare well or favorably with the WENO methods.

Further work will include extension to other hyperbolic systems as well as more careful study of the approximation of the source terms.

References

1. R. Abgrall. On essentially non-oscillatory schemes on unstructured meshes: analysis and implementation. *J. Comput. Phys.*, 114(1):45–58, 1994.

2. H. Atkins and C.-W. Shu. Quadrature-free implementation of the discontinuous Galerkin method for hyperbolic equations. *AIAA Journal*, 36:775–782, 1998.

3. D.S. Balsara and C.W. Shu. Monotonicity preserving weighted essentially non-oscillatory schemes with increasingly high order of accuracy. *J. Comput. Phys.*, 160:405–452, 2000.

4. M. Ben-Artzi and J. Falcovitz. A second–order Godunov–type scheme for compressible fluid dynamics. *J. Comput. Phys.*, 55:1–32, 1984.

5. S.J. Billett and E.F. Toro. WAF–type schemes for multidimensional hyperbolic conservation laws. *J. Comput. Phys.*, 130:1–24, 1997.

6. A. Bourgeade, P.G. LeFloch, , and P.-A. Raviart. An asymptotic expansion for the solution of the generalized Riemann problem. Part II: application to the gas dynamics equations. *Ann. Inst. H. Poincare, Nonlinear Analysis*, 6:437–480, 1989.

7. J. Casper and H. Atkins. A finite-volume high order ENO scheme for two dimensional hyperbolic systems. *J. Comput. Phys.*, 106:62–76, 1993.

8. J. Casper, C.-W. Shu, and H.L. Atkins. Comparison of two formulations for high-order accurate essentially non-oscillatory schemes. *AIAA Journal*, 32:1970–1977, 1994.

9. B. Cockburn and C.-W. Shu. TVB Runge-Kutta local projection discontinuous Galerkin finite element method for conservation laws II: general framework. *Mathematics of Computation*, 52:411–435, 1989.

10. B. Cockburn and C.-W. Shu. The Runge-Kutta discontinuous Galerkin method for conservation laws V: multidimensional systems. *J. Comput. Phys.*, 141:199–224, 1998.

11. B. Cockburn and C.-W. Shu. Runge-Kutta Discontinuous Galerkin methods for convection-dominated problems. *J. Sci. Comput.*, 16:173–261, 2001.

12. P. Colella. Multidimensional upwind methods for hyperbolic conservation laws. *J. Comp. Phys.*, 87:171–200, 1990.

13. R. Davies-Jones. Comments on 'A kinematic analysis of frontogenesis associated with a non-divergent vortex'. *J. Atm. Sci.*, 42:2073–2075, 1985.

14. M. Dumbser. ADER discontinuous Galerkin schemes for aeroacoustics. In *Proceedings of the Euromech Colloquium 449, Chamonix, France, 11th of December 2003*, 2003.

15. M. Dumbser and C.-D. Munz. Arbitrary high order discontinuous Galerkin schemes. In M. Gutnic S. Cordier, T. Goudon and E. Sonnendrucker, editors, *IRMA series in mathematics and theoretical physics. Numerical Methods for Hyperbolic and Kinetic Problems*, pages 295–333. EMS Publishing House, 2004.

16. M. Dumbser and C.-D. Munz. Building blocks for arbitrary high order discontinuous Galerkin schemes. *J. Sci. Comp.*, 2005. to appear.

17. M. Dumbser, T. Schwartzkopff, and C.-D. Munz. Arbitrary High Order Finite Volume Schemes for Linear Wave Propagation. In *Notes on Numerical Fluid Mechanics and Multidisciplinary Design (NNFM)*. Springer, 2005. to appear.

18. S.K. Godunov. A finite difference method for the computation of discontinuous solutions of the equations of fluid dynamics. *Mat. Sbornik*, 47:357–393, 1959.

19. A. Harten, B. Engquist, S. Osher, and S.R. Chakravarthy. Uniformly high order accurate essentially non-oscillatory schemes III. *J. Comput. Phys.*, 71:231–303, 1987.

20. A. Harten, P. D. Lax, and B. van Leer. On upstream differencing and Godunov-type schemes for hyperbolic conservation laws. *SIAM Review*, 25(1):35–61, 1983.

21. C. Hu and C.-W. Shu. Weighted essentially non-oscillatory schemes on triangular meshes. *J. Comput. Phys.*, 150:97–127, 1999.

22. G.S. Jiang and C.W. Shu. Efficient implementation of weighted ENO schemes. *J. Comput. Phys.*, 126:202–212, 1996.

23. M. K̈aser and A. Iske. ADER schemes for the solution of conservation laws on adaptive triangulations. In A. Iske and T. Randen, editors, *Mathematical Methods and Modeling in Hydrocarbon Exploration and Production, Series : Mathematics in Industry*, volume 7. Springer-Verlag, 2004.

24. M. K̈aser and A. Iske. ADER schemes on adaptive triangular meshes for scalar conservation laws. *J. Comput. Phys.*, 205:486–508, 2005.

25. V.P. Kolgan. Application of the minimum-derivative principle in the construction of finite-difference schemes for numerical analysis of discontinuous solutions in gas dynamics. *Uch. Zap. TsaGI*, 3(6):68–77, 1972. in Russian.

26. V.P. Kolgan. Finite-difference schemes for computation of three dimensional solutions of gas dynamics and calculation of a flow over a body under an angle of attack. *Uch. Zap. TsaGI*, 6(2):1–6, 1975. in Russian.

27. V.P. Kolgan. Finite-difference schemes for computation of two dimensional discontinuous solutions of nonstationary gas dynamics. *Uch. Zap. TsaGI*, 6(1):9–14, 1975. in Russian.

28. A.G. Kulikovskii, N. V. Pogorelov, and A. Yu. Semenov. *Mathematical Aspects of Numerical Solution of Hyperbolic Systems*. Chapman and Hall, 2002. Monographs and Surveys in Pure and Applied Mathematics, Vol. 118.

29. P.G. LeFloch and P.-A. Raviart. An asymptotic expansion for the solution of the generalized Riemann problem. Part I: general theory. *Ann. Inst. H. Poincaré, Nonlinear Analysis*, 5(2):179–207, 1988.

30. X.D. Liu, S. Osher, and T. Chan. Weighted essentially non-oscillatory schemes. *J. Comput. Phys.*, 115:200–212, 1994.

31. I.S. Men'shov. Increasing the order of approximation of Godunov's scheme using the solution of the generalized Riemann problem. *U.S.S.R. Comput. Math. Math. Phys.*, 30(5):54–65, 1990.

32. I.S. Men'shov. Generalized problem of break-up of a single discontinuity. *Prikl. Matem. i Mekhan. (J. Applied Mathematics and Mechanics))*, 55(1):86–95, 1991.

33. C.F. Ollivier-Gooch. Quasi-ENO schemes for unstructured meshes based on unlimited data-dependent least-squares reconstruction. *J. Comput. Phys.*, 133(1):6–17, 1997.

34. J. Qiu and C.-W. Shu. Finite difference WENO schemes with Lax-Wendroff type time discretization. *SIAM J. Sci. Comput.*, 24:2185–2198, 2003.

35. J. Qiu and C.-W. Shu. Hermite WENO schemes and their application as limiters for Runge-Kutta discontinuous Galerkin method II: two dimensional case. *Computers and Fluids*, 34:642–663, 2005.

36. J. Qiu and C.-W. Shu. Runge-Kutta discontinuous Galerkin method using WENO limiters. *SIAM J. Sci. Comput.*, 26:907–929, 2005.

37. P.L. Roe. Approximate Riemann solvers, parameter vectors, and difference schemes. *J. Comput. Phys.*, 43:357–372, 1981.

38. V.V. Rusanov. Calculation of interaction of non-steady shock waves with obstacles. *USSR J. Comp. Math. Phys.*, 1:267–279, 1961.

39. T. Schwartzkopff, M. Dumbser, and C.D. Munz. Fast high order ADER schemes for linear hyperbolic equations. *J. Comput. Phys.*, 197(2):532–539, 2004.

40. T. Schwartzkopff, C.D. Munz, and E.F. Toro. ADER-2D: a high-order approach for linear hyperbolic systems in 2D. *J. Sci. Comput.*, 17:231–240, 2002.

41. J. Shi, C. Hu, and C.-W. Shu. A technique for treating negative weights in WENO schemes. *J. Comput. Phys.*, 175:108–127, 2002.

42. C.-W. Shu. Total - Variation - Diminishing time discretizations. *SIAM J. Scientific and Statistical Computing*, 9:1073–1084, 1988.

43. C.-W. Shu and S. Osher. Efficient implementation of essentially non-oscillatory shock-capturing schemes. *J. Comput. Phys.*, 77:439–471, 1988.

44. C.-W. Shu, T.A. Zang, G. Erlebacher, D. Whitaker, and S. Osher. High order ENO schemes applied to two and three dimensional compressible flow. *Applied Numerical Mathematics*, 9:45–71, 1992.

45. R.J. Spitery and S.J. Ruuth. A new class of optimal high-order strong-stability-preserving time discretization methods. *SIAM J. Numer. Anal.*, 40(2):469–491, 2002.

46. A. Suresh and T. Huynh. Accurate monotonicity preserving scheme using Runge-Kutta time stepping. *J. Comput. Phys.*, 136:83–99, 1997.

47. Y. Takakura and E.F. Toro. Arbitrarily accurate non-oscillatory schemes for a nonlinear conservation law. *CFD Journal*, 11(1):7–18, 2002.

48. N.I. Tilaeva. A generalization of the modified Godunov scheme to arbitrary unstructured meshes. *Uchenye Zapiski TsaGI*, 17(2):18–26, 1986. in Russian.

49. V.A. Titarev and E.F. Toro. ADER: arbitrary high order Godunov approach. *J. Sci. Comput.*, 17:609–618, 2002.

50. V.A. Titarev and E.F Toro. High order ADER schemes for the scalar advection-reaction-diffusion equations. *CFD Journal*, 12(1):1–6, 2003.

51. V.A. Titarev and E.F. Toro. ADER schemes for shallow water equations with pollutant transport. In *XXIX Convegno di Idraulica e Costruzioni Idrauliche,Trento, Italia*, volume 1, pages 909–914. Springer-Verlag, 2004.

52. V.A. Titarev and E.F. Toro. Finite-volume WENO schemes for three-dimensional conservation laws. *J. Comput. Phys.*, 201(1):238–260, 2004.

53. V.A. Titarev and E.F. Toro. ADER schemes for three-dimensional nonlinear hyperbolic systems. *J. Comput. Phys.*, 204(2):715–736, 2005.

54. V.A. Titarev and E.F. Toro. MUSTA schemes for multi-dimensional hyperbolic systems: analysis and improvements. *International Journal for Numerical Methods in Fluids*, 49(2):117–147, 2005.

55. A.I. Tolstykh. On a method for the numerical solution of the compressible Navier-Stokes equations over a wide range of Reynolds numbers. *Dokl. Akad. Nauk. SSSR*, 210(48), 1973. *Engl. transl., Sov. Phys. Dokl, V. 18, 74, 1973.*

56. A.I. Tolstykh. *Compact difference schemes and their application to problems of aerohydrodynamics*. Nauka, Moscow, 1990. In Russian.

57. A.I. Tolstykh. *High accuracy non-centered compact difference schemes for fluid dynamics applications*. World Scientific Publishing, 1994.

58. A.I. Tolstykh. Centered prescribed-order approximations with structured grids and resulting finite-volume schemes. *Applied Numerical Mathematics*, 49:431–440, 2004.

59. A.I. Tolstykh and D. A.Shirobokov. Difference schemes with compact fifth-order approximations for spatial flows of a viscous gas. *Computational Mathematics and Mathematical Physics*, 36(4):477–489, 1996.

60. A.I. Tolstykh and M.V. Lipavskii. On performance of methods with third- and fifth-order compact upwind differencing. *J. Comput. Phys.*, 140(2):205–232, 1998.

61. E.F. Toro. A weighted average flux method for hyperbolic conservation laws. *Proc. Roy. Soc. London*, A423:401–418, 1989.

62. E.F. Toro. Riemann problems and the WAF method for solving two–dimensional shallow water equations. *Phil. Trans. Roy. Soc. London*, pages 43–68, 1992.

63. E.F. Toro. The weighted average flux method applied to the time–dependent Euler equations. *Phil. Trans. Roy. Soc. London*, A341:499–530, 1992.

64. E.F. Toro. Primitive, conservative and adaptive schemes for hyperbolic conservation laws. In E.F. Toro and J.F. Clarke, editors, *Numerical Methods for Wave Propagation*, pages 323–385. Kluwer Academic Publishers, 1998.

65. E.F. Toro. *Riemann solvers and numerical methods for fluid dynamics*. Springer-Verlag, 1999. Second Edition.

66. E.F. Toro. *Shock-Capturing Methods for Free-Surface Shallow Flows*. Wiley and Sons Ltd., 2001.

67. E.F. Toro. Multi-stage predictor-corrector fluxes for hyperbolic equations. *Preprint NI03037-NPA. Isaac Newton Institute for Mathematical Sciences, University of Cambridge, UK*, 2003.

68. E.F. Toro. MUSTA: A multi-stage numerical flux. *Preprint NI04008-NPA. Isaac Newton Institute for Mathematical Sciences, University of Cambridge, UK*, 2004.

69. E.F. Toro. Riemann solvers with evolved initial conditions. *Preprint NI05003-NPA. Isaac Newton Institute for Mathematical Sciences, University of Cambridge, UK*, 2005.

70. E.F. Toro and S.J. Billett. Centred TVD schemes for hyperbolic conservation laws. *IMA J. Numerical Analysis*, 20(1):47–79, 2000.

71. E.F. Toro, R.C. Millington, and L.A.M. Nejad. Primitive upwind methods for hyperbolic partial differential equations. In C. H. Bruneau, editor, *Sixteenth International Conference on Numerical Methods for Fluid Dynamics. Lecture Notes in Physics*, pages 421–426. Springer-Verlag, 1998.

72. E.F. Toro, R.C. Millington, and L.A.M. Nejad. Towards very high order Godunov schemes. In E. F. Toro, editor, *Godunov Methods. Theory and Applications*, pages 907–940. Kluwer/Plenum Academic Publishers, 2001.

73. E.F. Toro, M. Spruce, and W. Speares. Restoration of the contact surface in the Harten-Lax-van Leer Riemann solver. *Journal of Shock Waves*, 4:25–34, 1994.

74. E.F. Toro and V.A. Titarev. Solution of the generalised Riemann problem for advection-reaction equations. *Proc. Roy. Soc. London*, 458 (2018):271–281, 2002.

75. E.F. Toro and V.A. Titarev. TVD fluxes for the high-order ADER Schemes. In *Preprint NI03011-NPA*, pages 1–37. Isaac Newton Institute for Mathematical Sciences, University of Cambridge, UK., 2003.

76. E.F. Toro and V.A. Titarev. MUSTA schemes for systems of conservation laws. *Preprint NI04033-NPA. Isaac Newton Institute for Mathematical Sciences, University of Cambridge, UK*, 2004. to appear in J. Comput. Phys.

77. E.F Toro and V.A. Titarev. TVD Fluxes for the high-order ADER schemes. *J. Sci. Comput.*, 24(3):285–309, 2005.

78. E.F. Toro and V.A. Titarev. Derivative Riemann solvers for systems of conservation laws and ADER methods. *J. Comput. Phys.*, 212(1):150–165, 2006.

79. J.J.W. van der Vegt and H. van der Ven. Discontinuous Galerkin Finite Element Method with Anisotropic Local Grid Refinement for Inviscid Compressible Flows. *J. Comput. Phys.*, 141(1):46–77, 1998.

80. J.J.W. van der Vegt and H. van der Ven. Space-time discontinuous Galerkin finite element method with dynamic grid motion for inviscid compressible flows: I. General formulation. *J. Comput. Phys.*, 182(2):546–585, 2002.

81. H. van der Ven and J.J. W. van der Vegt. Space-time discontinuous Galerkin finite element method with dynamic grid motion for inviscid compressible flows: II. Efficient flux quadrature. *J. Comput. Phys.*, 191(41-42):4747–4780, 2002.

82. B. van Leer. Towards the ultimate conservative difference scheme V: order sequel to Godunov's method. *J. Comput. Phys.*, 32:101–136, 1979.

83. P. Woodward and P. Colella. The numerical simulation of two-dimensional fluid flow with strong shocks. *J. Comput. Phys.*, 54:115–173, 1984.

84. Y.-T. Zhang, J. Shi J, C.-W. Shu, and Y. Zhou. Numerical viscosity and resolution of high-order weighted essentially nonoscillatory schemes for compressible flows with high Reynolds numbers. *Physical Review E*, 68:1–16, 2003. article number 046709.